CONFINEMENT PROPERTIES OF HIGH ENERGY
DENSITY PLASMAS IN THE
WISCONSIN LEVITATED OCTUPOLE

by

JONATHAN CHADSEY TWICHELL

A thesis submitted in partial fulfillment of the
requirements for the degree of

Doctor of Philosophy
(Nuclear Engineering)

at the
UNIVERSITY OF WISCONSIN—MADISON
1984

CONFINEMENT PROPERTIES OF HIGH ENERGY DENSITY
PLASMAS IN THE WISCONSIN LEVITATED OCTUPOLE

Jonathan Chadsey Twichell
Under the supervision of Professor J. D. Callen

The confinement of particles and energy is critically dependent on the plasma-wall interaction. Results of a study detailing this interaction are presented.

High power ICRF heated and gun afterglow plasmas were studied to detail the mechanisms determining particle and energy confinement. An extensive zero-D simulation code is used to assist in interpreting the experimental data. Physically reasonable models for plasma surface interactions, time dependent coronal treatment of impurities and multiple region treatment of neutrals are used in modeling the plasma. Extensive diagnostic data are used to verify the model.

Non-heated plasmas decay from 28 to 3 eV allowing clear identification of wall impact energy thresholds for desorption and particle reflection. The charge state distribution of impurities verifies the reflux to plasma diffusion rate ratio. Close agreement between the simulation and experimental data is found.

ICRF heated plasmas have spatial and velocity anisotropies making modeling less conclusive. A hot ion edge plasma supported by RF dramatically enhances reflux. Multiple limiters and limiter gas load

depletion are observed. The code accurately models impurity behaviour but the spatial dependencies reduce the accuracy of modeled neutral densities. RF seems to reduce the plasma diffusion rate but this may be an artifact caused by inaccurate rate coefficients. Sensitivity of the model to threshold cross sections is discussed as is the possible effect on molecular rate coefficients of vibrational excitation.

Financial support has been provided by the United States Department of Energy.

ACKNOWLEDGEMENTS

This study would not have been possible without my wife Kristi's loving support, encouragement, and endless patience, and my daughter Sarah's cheerful tolerance of my absence while working.

I am deeply indebted to Professor R. N. Dexter for his guidance, help in taking data, and many illuminating discussions. His assistance, both scientific and personal, made graduate study possible. His kindness and understanding made it enjoyable

Professor J. D. Callen lent support and insight when it was most needed, and this is greatly appreciated.

Many people helped develop, operate, and maintain the experiment in the course of this study. Cliff Fortgang, Ted Strait, Skip Garner, and Mike Zarnstorff provided essential assistance and deserve more than thanks. Many thanks to John Laufenberg for his technical support of the experiment.

Many helpfull conversations with Andy Feldt are acknowledged, as well as the use of computer facilities in the Department of Physics and Astronomy at the University of Oklahoma.

Shireen Ray typeset this manuscript. Her timely and competent work against constant deadlines are deeply appreciated.

My thanks to Tom Lovell for his technical expertise, gentle guidance, and a shoulder to cry on when nothing worked.

TABLE OF CONTENTS

CHAPTER 1

INTRODUCTION

Overview

The objective of this research is to study the confinement properties of the Levitated Octupole plasmas. Explicitly, the goal is to determine the magnitude and scaling of the particle and energy source terms in the conservation equations. The study will be restricted to plasmas with energy densities high enough that atomic processes can be important. In most of these plasmas, atomic process terms in the conservation equations are the dominant terms. Thus, of primary interest are wall reflux, impurity radiation, and charge exchange.

Particle and energy density become inseparably intertwined in such plasmas. For example, a spectral line intensity depends on the electron temperature and density as well as on the density of the impurity in a particular charge state. This, in turn depends on the history of the plasma. Thus, with rare exception, the study of atomic processes in plasmas forces an integrated study of particle and energy behavior. Particles (both neutrals and ions) leave the plasma and hit the wall. A variety of processes contribute to the wall reflux. Reflection, desorption, and sputtering occur, each with a rate dependent on the incoming particle's momentum and ionic charge. Wall reflux is the

primary source of neutrals and impurities to the plasma, hence it strongly affects the plasma temperatures, radiation rate, and neutral density. These processes in turn modify the flux of particles to the wall.

In plasmas where atomic processes are important, the determination of confinement properties becomes a complex study of the interplay of a large number of effects. Experiment and numerical modeling are the primary tools used. The results of the study take on a significance greater than the numeric values of terms in a conservation equation. To get those values, an understanding of the interactions of plasma, atomic, and surface processes is required.

The accurate modeling of the global behavior of the plasma permits (and in some cases demands) treatment of subtle processes often ignored. A case in point is the dramatic effect the small ungettered portion of the wall has on reflux. Less than 10% of the wall accounts for virtually all of the molecular hydrogen and impurities in the plasma. Further, the location of the ungettered wall is of critical importance.

Motivation

The interaction of a Tokamak plasma with the wall and limiter has a profound effect on many aspects of the plasma.[1] Impurity content affects $\langle z \rangle$, the plasma conductivity,[2] and the temperature profile,[3] hence MHD stability.[4] Line radiation from high z impurities can make

ignition impossible.[5,6] The techniques and physical understanding resulting from a study of the high energy density Octupole plasmas are directly applicable to Tokamak edge plasmas.

The Octupole's operational flexibility (independent control of fields, density, power input, etc.) permits the verification of models over a far greater range of parameter space than a Tokamak can explore. Thus the physical processes involved are more accessible.

Finally, and most directly, is the desire to increase the temperatures, energy density, and plasma pressure (β) obtained in the Octupole. Since atomic processes dominate the physics of these discharges, a thorough understanding of confinement is an essential prelude to enhancing the plasma parameters.

A new operational regime for the octupole is being explored. Never before have both density and temperature been high enough for atomic processes to be important. With the recent addition of an ICRF heating source more than 0.1 W/cm^3 can be applied to the plasma. Under these conditions atomic processes overwhelm the usual loss mechanisms (particle and heat transport by collective plasma effects). Thus previous studies of diffusion and transport in the Octupole are not applicable to heated plasmas.[7,8,9,10] Further, tokamak codes cannot be applied to simulate Octupole plasmas. Different geometries, heating techniques and temperature ranges lead one to very different sets of approximations in writing such codes.

Concise Statement of the Problem

The primary objective of this study can be restated as: The development and use of techniques to quantitatively determine the important particle and energy loss mechanisms. The basic approach taken is the validation of a physically based model with experimental data. Once validated, the model then yields a wealth of data difficult or impossible to obtain experimentally. The physical insight thus gained permits a detailed interpretation of experimental data. The model used is an evolver type code named ZD. Given initial conditions and a few parameters describing experimental conditions (input power, wall condition, etc.) the code generates densities and temperatures of each specie (hydrogen and several impurities in all charge states and electrons). The input parameters are adjusted to produce a match with a limited subset of experimental diagnostics (typically density and electron temperature). The code results are then compared with the remaining data (spectral line intensities, radiated power, ion temperature, neutral flux, etc.).

The complexity of the problem forces one to assume spatial homogeneity (referred to as zero-D) in most modeling and experimental data analysis. Supplemental experimental work addresses some of the spatially dependent features and provides independent checks of the model's validity. By varying basic plasma parameters over order of

magnitude ranges, we gain substantial confidence in the physical basis of the model.

It should be stressed that our objective is more than assigning powers to various loss channels. We seek to gain insight into the physical mechanisms responsible for these losses. The remarkable character of the plasma-wall interaction holds a variety of surprises in store.

The remainder of the thesis is organized as follows. Chapter 2 covers the research design of the study. After an overview of the physics involved, the chapter covers the use and validation of models in experimental research. Chapter 3 details the experimental facilities used. Of primary importance here are the diagnostics used, and particularly the diagnostics developed for the study. Chapter 4 describes the models used in detail. After covering each physical process, the limitations and assumptions of the models are addressed. Chapters 5 and 6 present the results of both experiment and modeling for (respectively) gun-only target plasmas and ICRF heated plasmas. The final chapter summarizes the work. Suggestions for future work are given.

References for Chapter 1

[1]G.M. McCracken, P.E. Stott, *Nucl. Fusion* **19**, 889 (1979).

[2]E. Hinnov, L.C. Johnson, E.B. Meservey, D.L. Dimock, *Plasma Phys.* **14**, 755(1972).

[3]H.P. Furth, *Nucl. Fusion* **15**, 487(1975).

[4]R.J. Bickerton, Culham Laboratory, Report CLM-R 176, 1977.

[5]R.F. Post, *Ref. Mod. Phys.* **28**, 338(1956).

[6]D.M. Meade, *Nucl. Fusion* **14**, 289(1974).

[7]G.A. Navratil, R.S.Post, A.B. Ehrhardt, *Phys. Fluids* **20**, 156(1977).

[8]G.A. Navratil, R.S. Post, A.B. Ehrhardt, *Phys. Fluids* **22**, 241(1977).

[9]J.R. Drake *et al.* in Plasma Physics and Controlled Nuclear Fusion Research (IAEA, Vienna, 1976), Vol. II, p. 333.

[10]H.R. Garner, Ph.D. Thesis, University of Wisconsin, 1982.

CHAPTER 2

RESEARCH DESIGN

Objectives

The objective of this chapter is to review how the goal of determining confinement properties is to be achieved. Particular attention to the use of computer models in experimental research is called for given the importance of such codes in this study. The discussion of procedures used to experimentally validate the physics in the code is the final topic of this chapter. We begin with a review of the physical processes involved in the study of confinement. Detailed consideration of each process will be left to Chapter 4.

The starting point for any discussion of confinement is the set of conservation equations for the plasma. Because atomic processes are important, equations for each specie are needed. The set of species is large, consisting of electrons and, for each element of nuclear charge z, $z+1$ species (one for each possible ionization level from neutral to fully stripped). A few additional species are added to the set to treat molecular forms of hydrogen (H_2, H_2^+). For each specie a conservation equation for particles and energy is then written:[1]

$$\frac{\partial n_i}{\partial t} + \nabla \cdot \vec{\Gamma}_i = S_i \tag{2.1}$$

$$\frac{\partial \frac{3}{2} E_i}{\partial t} + \nabla \cdot \vec{Q}_i = R_i \tag{2.2}$$

where, for the i^{th} species

n_i = density

$\vec{\Gamma}_i$ = particle flux/unit area = $n\vec{V}$

E_i = energy density = nkT

$\vec{Q}_i$ = heat flux/unit area = $nkT\vec{V}$

S_i = particle (Source - Sink) density

R_i = energy (Source - Sink) density

Virtually all the difficulties involved arise from the source terms. For particles the source term includes creation and destruction of particles by ionization, recombination, and charge exchange. The rate those processes occur at depends on the density of other species, and on the electron temperature. The energy source term includes the collisional exchange energy with all other species, the classical "thermodynamic force" terms, inelastic collisions, and the transfer of energy due to particles changing species. Again many of these terms depend on the density and temperature of other species.

Atomic Processes

Such a complex approach to confinement is necessary only if atomic processes are an important part of the conservation equations. Two conditions must be met for this to be true. First, the electron temperature must be a significant fraction of a typical ionization energy (say 10 eV). Below about 3 eV, the electrons simply don't have enough

energy to excite impurity atoms, much less ionize them. Second, the rate of such excitation must be high enough to substantially modify the plasma energy density during a particle confinement time.

The second condition can be numerically estimated to give a lower limit for the density in the octupole at which atomic processes dominate energy confinement. The energy loss by particle transport can be compared with that of a typical atomic process as follows:

$$\frac{2n_eT_e}{\tau} \leq E_{exc}n_z n_e\langle\sigma_z V\rangle \qquad (2.3)$$

where

$\langle\sigma_z V\rangle$ = Maxwellian averaged rate coefficient

n_e = electron density

n_z = impurity density

E_{exc} = excitation energy

$2T_e$ = average energy/particle ($T_e = T_i$)

τ = shorter of particle confinement or experiment time.

$\langle\sigma_z V\rangle$ is within an order of magnitude of 10^{-8} cm^3sec^{-1} for most processes (charge exchange, ionization, excitation) for low z atoms or ions.[2,3,4] Also, the energy of the first excited state is usually close to the ionization energy. Thus equation 2.3 is a reasonable minimum density threshold for a broad range of impurities and processes. By expressing n_z as a fraction, f, of n_e ($n_z = fn_e$) and rearranging

$$n_e \geq \frac{2T}{E_{exc}}\frac{1}{\tau f\langle\sigma_z V\rangle}. \qquad (2.4)$$

As any great difference between T and E_{exc} will result in a shift in the distribution of ionization states until there is insufficient electron energy to ionize at a rate in excess of the recombination rate, $\frac{2T}{E_{exc}} \sim 1$. Assuming $\tau \sim$ 10 msec, $f \sim 0.01$ we get $n_e \geq 10^{12}$ cm^{-3}. This result overestimates the density at which atomic processes dominate energy confinement. Only one process is considered, and some common impurities (notably oxygen) have larger rate coefficients.[2,3]

The plasmas under study have electron temperatures of 20-50 eV and densities in the vicinity of 10^{13} cm^{-3}. From the preceding discussion atomic effects would be expected to be important. Experimental measurements indicate that impurity radiation and charge exchange are, in fact, the dominant energy losses. Bolometric measurements indicate about 1/2 the input power (for ICRH plasmas) is radiated away as VUV line radiation. Charge exchange and spectroscopic diagnostics indicate hydrogen charge exchange is the other major loss channel.

Plasma Wall Interactions

Neutral hydrogen and, to a lesser degree, impurities exist within the plasma volume by virtue of a complex and dynamic process; the interaction between the plasma and the wall. Ions diffuse across the field lines and impact the wall. Neutrals don't feel the field, and so travel directly from their birthplace (the opposite wall or a charge exchange or recombination event) to the wall unless an intervening

charge exchange or ionization event occurs. Three processes result in particles being emitted from the wall in response to this incoming flux.

First the incoming particle can be reflected as a neutral. In effect it bounces, picking up (if necessary) an electron as it interacts with the surface. Second, one or more particles can be desorbed from the loosely bound surface layers. Third, an atom can be sputtered from a tightly bound clean surface. Virtually all wall reflux particles are neutral.[5] Any ions produced at the wall have an overwhelming probability of simply executing a gyro orbit back into the wall.

As mentioned earlier, the cross section for each process depends on the mass, charge and velocity of the incoming particle. One of the assumptions of the model is that reflux due to impurities hitting the wall is ignorable. Although doping experiments do not clearly confirm this assumption, it is an unrealistic complication to include significant amounts of impurity ion induced desorption. Another observation is that the cross sections depend on the character of the surface. This undoubtedly varies with position in the machine, and depends on the recent operating history of the experiment.

The effectiveness of discharge cleaning and the observed day to day variation in plasma parameters demonstrate the significance of the inner wall surface condition. To minimize the effects of this variation in wall condition every effort was made to acquire a complete set of data

in one shot. To such end the largest set of simultaneous diagnostics ever run on the experiment was used. Enough data were collected in a single shot to use, and validate, the computer code. Scaling studies were run only after days of conditioning to insure consistent shot to shot behavior. This was further checked by returning to the 'standard' configuration. Thus the wall condition was consistent, if not controlled.

Simple physical models are used to determine the reflux from the wall. The energy dependence is taken from the literature.[5] Only one parameter, the fraction of the wall covered by each specie, is used to describe the wall condition. Particle reflection is taken to be that of a clean titanium surface, but the reflection coefficient is insensitive to wall condition.

Unfortunately, the details of the plasma-wall interaction are experimentally inaccessible by direct observation. The behavior of the wall must be inferred from the effects on the plasma. One can measure spectral line intensities, but significant, interpretable data comes only from multiply ionized species. Lower ionization states 'burn out' and higher states are not produced. Thus the observable effects of the plasma-wall interaction are quite removed from their source. Indeed, one must know the history of most facets of the plasma to interpret spectroscopic data. Thus the conclusion that a global treatment of the plasma is required is reiterated.

Computer Codes

The fact that many of the processes which affect a spectral line intensity are not observable forces the use of computer codes for even the simplest of applications. As noted above, only a few of the possible ionization states of an impurity will radiate much power. Time-dependent coronal equilibrium theory is used to determine the distribution of population among states. Since the power radiated per unit volume is

$$P_{rad} = n_e n_z \langle \sigma_{exec} V_e \rangle E_{exec} \qquad (2.5)$$

knowledge of the electron density and temperature is required to infer an impurity density. Since, however, the ionization state under observation is close to the equilibrium state, knowledge of ionization rates and recombination rates for all species is essential to relate the observed line intensity (via the multiply ionized state density) to the neutral source rate. Computer codes are indispensible for such calculations.

Returning to the conservation equations 2.1 and 2.2, the preceding discussion demonstrated not only the necessity of computer codes to interpret spectroscopic data, but described the source and sink terms in the particle conservation equation. It would seem reasonable, then, that the solution of the conservation equations and the interpretation of spectral lines be unified in a single code. Indeed, one has little choice. The nonlinear nature of many of the terms and the complex

coupling between terms dictates the method used to solve the equations. They must be brute force integrated given a set of initial conditions.

Such 'evolver' codes reduce the problem of solving the conservation equations to specifying an algorithm to calculate each term. Given a set of initial conditions, the terms in the differential equation are calculated, and over some small time step, summed. Thus these codes evolve the initial conditions in time. There remains a choice of initial conditions and the choice of physical processes and approximations used to make the code realizable.

Limitations

There are several fundamental practical limitations which must be faced. The primary restriction is a limit on the dimensionality of the study. Neither the data nor computer time is available to permit more than a zero-D treatment. The octupole geometry of the experiment makes spatially resolved spectroscopic data close to impossible to obtain. It has the mitigating characteristic that half the plasma volume is contained within 20% of the flux volume. [A plot (Figure 1) of n_e and T_e *vs* V(ψ) shows that 50% of the volume of the machine has temperatures and density within 25% of the peak separatrix value.] This volume also comprises 80% of the plasma observed by midcylinder line-averaged diagnostics (spectrometers, microwave interferometer, etc.)

Nevertheless, the zero-D nature of the study is its single most limiting characteristic.

Some concessions to the spatial nature of the machine have been made, however. The behavior of H^0 and H_2 are so critical in determining basic plasma parameters that these species are divided into spatial regions. Two regions are used: The center of the machine, and the bridge region. Order of magnitude differences of the density of H^0 and H_2 result in the two regions.

Another series of improvements over zero-D modeling involve corrections for the known spatial and velocity space anisotropies of the ion distribution function during RF heating. RF is seen to heat the edge of the plasma, probably to a gyroradius limit. Experimental data are used to determine the edge ion temperature to establish the correct energy of ions impacting the walls and limiter. This edge ion region is not, however, fully treated. The H^+ species temperature is considered an average over position (including the edge) and velocity space.

A second limitation is the accuracy of rate coefficient data. These are calculated as needed by the code. Details are given in Chapter 4 and its references. The rate coefficients are accurate to within a factor of 2. This calculation (adapted from a code written by R. Hulse and D.E. Post of PPPL[6]) is the best data currently available. It would be pointless to perform higher dimensionality modeling for impurities as the confidence in the results would be negligible given the accuracy of

the rate coefficients.

To review, the study of confinement can be restated as the determination of the values and scaling of the terms in the conservation equations 2.1 and 2.2. Atomic processes will be dominant in the regimes under study. As wall reflux is the primary source of neutrals and impurities, a thorough understanding of the plasma-wall interaction is essential. Indeed, this is the most important aspect of confinement under study. Because experimental data are so removed from the details of the plasma-wall interaction, computer codes become an essential part of interpreting the data. Limited accuracy of rate coefficients and difficulty in obtaining spatially resolved data in the experiment's complex geometry restrict the study to zero-D.

References for Chapter 2

[1]S.I. Braginskii, in Reviews of Plasma Physics, edited by M.A. Leontovich (Consultants Bureau, New York), Vol. 1, p. 205.

[2]D.E. Post, R.V. Jensen, C.B. Tarter, W.H. Grasberger, W.A. Lokke, *Atomic Data and Nuclear Data Tables* **20**, 397(1977).

[3]W. Lotz, *Astrophys. J. Suppl.* **14**, 207(1967).

[4]E.L. Freeman, E.M. Jones, Culham Laboratory, Report CLM-R137 (1974).

[5]G.M. McCracken, P.E. Stott, *Nucl. Fusion* **19**, 889(1979).

[6]D.E. Post, R. Hulse, private communication.

Figure 1. Electron density and temperature plotted versus $V(\psi)$, the volume enclosed by the ψ flux surface. Data were taken by Dr. Strait for a full power ICRF shot just before the end of the RF pulse.

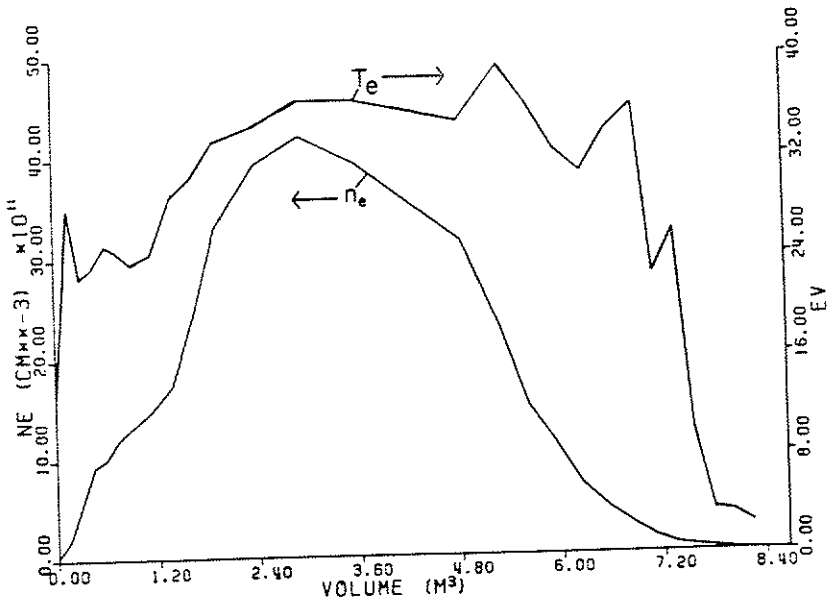

CHAPTER 3

EXPERIMENTAL FACILITIES

General Machine Description

The Wisconsin Levitated Octupole was the experimental facility used for these studies. The machine has a long history, and several references exhaustively detail its characteristics.[1,2,3] ICRF heating is a relatively recent addition. Fortgang's thesis covers the construction, theory, and performance of the ICRF system.[4] Several diagnostics were added to the experiment to permit the study of impurities. These include VUV monochromators, bolometers, and interference filter line monitors. Their characteristics, and interpretation of their data, are the primary subjects of this chapter.

The Wisconsin Levitated Octupole (Figure 1) is a toroidal internal ring machine with an octupole field geometry. The poloidal field is generated by inductively coupling the discharge of a large capacitor bank into the four internal rings. Figure 2 shows the poloidal field generated while Figure 3 has mod B surfaces and the location of the ICRF resonance zone.

Figure 4 shows the timing of a standard shot. The 'standard shot' comprises a set of machine and plasma parameters which are easily reproduced, consistent, and operate the equipment at conserva-

tive power levels. Thus, the data presented in later chapters is not representative of plasmas optimized for temperature, or β. Table 1 gives machine and plasma parameters for the standard experimental configuration.

A number of facilities available for use were not employed. Most data were taken without toroidal field. While the internal rings can be levitated (the ring supports pneumatically removed during the shot) this produced no appreciable improvement in plasma parameters. All data were taken with the rings left supported. The poloidal field strength can also be varied, but for consistency the values given in Table 1 were always used in this study.

The ICRF oscillator can generate a 10 millisecond pulse with 2 megawatts input power. This typically coupled 600 kilowatts to the plasma. The pulse is usually terminated at 9.5 milliseconds to avoid variations of input voltage which occur in the pulse forming network during the last half-millisecond. The pulse is abruptly terminated by crowbarring the power supply. This can be done at any time during the pulse. The input voltage, hence RF power, can be set as well.

The Octupole vacuum volume is about 8.6 m^3 and has about 40 m^2 of wall surface area. Approximately 75% of the wall area is continuously coated with titanium[5] from 6 getters located on the midplane (see Figure 2). These getters produce about 10^5 l/sec[6] of H_2 pumping. More importantly, they leave the majority of the wall

free of adsorbed gas. The region behind the rings and the nose are in getter shadow, however, leaving much of the surface in the bridge region ungettered. Details of the treatment of wall surface conditions will be deferred to Chapter 4.

The octupole pumping is designed to minimize impurity content of the plasmas. Two cryopumps provide about 8000 l/sec for most gases (hydrogen and helium being the notable exceptions). Two turbopumps provide 1500 l/sec of removal pumping. A regular program of discharge cleaning was used to condition the walls. Typical base pressures of 6×10^{-8} Torr are achieved with the residual gas being primarily water and hydrogen.

The plasma source used for this study was the "intermediate" gun. This Marshall gun produces a 1×10^{13} cm^{-3} plasma with ion and electron temperatures about 30 eV. The operating voltages and timing for the gun were optimized to produce high electron temperatures. The injected plasma is typically reproducible to within 5%. The gun produces a very low impurity content plasma with a negligible neutral gas component.

As mentioned in Chapter 2, basic plasma parameters are quite sensitive to the wall condition for ICRF heated shots. Care in operating the vacuum system, heavy gettering, and discharge cleaning help establish stable day to day behavior. Plasma parameters could typically be reproduced to within 10%. To reduce the errors in data analysis due

to shot to shot variation, the data acquisition system was upgraded. The objective was to acquire enough data to validate the computer code ZD in a single shot.

Data Acquisition

Twenty channels of diagnostic data were simultaneously digitized. About 10^5 total data points were taken and archived per shot. Shot cycle time was limited by the computer's ability to handle the data. Maintaining all diagnostics and the supporting electronics was a constant problem.

Great care was taken to ensure the accuracy of the digitized data. The large, low frequency electric fields from the ICRF oscillator were notoriously efficient in coupling into the diagnostic electronics. Fiberoptic light guide was used whenever possible. Amplifiers with 60 db attenuation of common mode signals at the ICRF frequency (1 MHz) were developed. Numerous shielding and RF trapping strategies were employed. RF coupling was not the only problem.

Marshall guns require fraction of a megamp ten microsecond current pulses with driving voltages of 10-20 kilovolts. It was not unusual to see different sections of the ground bus (40 cm^2 aluminum bus bar) with 300 volt potential differences during the gun discharge. The diagnostics were distributed around the experiment but all were tied to the central data acquisition system. This mandated extreme

care in grounding, and generated some rather spectacular faults.

Digitizers were run well above the Nyquist limit for the bandwidths of the signals being measured. Aperture uncertainty and sample timing jitter contributed negligible error. Amplifier nonlinearity induced less error than the digitizer quantization. Offset drifts were measured and subtracted for each shot. The experiment was initiated synchronously with the 60 Hz line frequency. Timing control of the experiment was absolutely calibrated to 10^{-6} second and was repeatable to within 10^{-8} seconds.

Diagnostics

The standard diagnostics for measuring density and temperatures will be briefly reviewed with references to the literature for details. The operation and interpretation of diagnostics built for or critical to this study will be covered in detail.

Microwave Interferometer

Electron density is measured with a 70 GHz microwave digital multiradian fringe shift interferometer.[7] The interferometer absolutely measures the line integrated density along a vertical chord through the center of the plasma. This path heavily weights the separatrix density and leaves the result quite insensitive to profile changes.

Probes

Probes are used extensively in the octupole.[8,9] Tests indicate they do not significantly perturb the plasma (except for a slight increase in impurity content and concomitant reduction in T_e for large probes). A triple tipped Langmuir probe is used to measure electron temperature. Two of the tips are used as a floating double probe to accurately obtain the ion saturation current. The third probe tip is used to measure plasma admittance.[10] These data are processed by the computer to produce the electron temperature.

Measures of Ion Temperature

Several measures of ion temperature were used. A charge exchange system measures the energy dependence of the neutral flux leaving the plasma. The analyzer, like the interferometer, views a midcylinder vertical chord of the plasma. Energetic ions charge exchange in the plasma and are no longer confined. Those entering the analyzer charge exchange again in a gas cell and are energy selected in a cylindrical electrostatic analyzer. A Daley detector (sensitive to single particles) measures the energy selected flux. The potential on the energy analyzer is swept to measure the entire high energy (>100 eV) distribution. As the charge exchange cross section energy dependence is well known the ion distribution function can be unfolded from the

raw data. This in turn yields the ion temperature.

In practice, ICRF heated plasmas yield a distinct two component ion temperature (Figure 5). As the analyzer views the entire midcylinder the two component ion distribution was thought to be due to spatial variations in T_i.

A local diagnostic of the ion distribution function confirmed this hypothesis. The gridded ion probe consists of a Faraday cup with grids to repel all electrons and ions of less than a set energy. A floating pinhole faces the plasma, and a secondary electron suppressor grid in front of the ion collector completes the probe. The ion current collected is proportional to the number of ions entering the probe of energy greater than the ion repeller voltage. Thus sweeping this voltage yields a scan of the ion distribution function. $I \alpha \int_V^\infty f_i(E)\,dE$. $I(V)$ is then reduced to $f(E)$ by differentiating, and T_i is then available from $f(E)$.

The probe is less than 1/4" in diameter. It can be positioned to sample any part of the common flux and rotated to obtain the ion temperature at an angle relative to $\vec{B}$. The lifetime of this delicate probe in high power RF shots was quite short, hence only limited data are available. Figures 6 and 7 show the measured ion temperature perpendicular and parallel to $\vec{B}$ as a function of position.

Strait[11] calculates that these data are consistent with the charge exchange data. Thus the two temperature distribution of the charge exchange data is attributed to the velocity anisotropy near the edge of the

plasma. The causes of the spatial variation of T_i and the strong velocity isotropy are not well understood.

Strait[11] performed a one-dimensional study of ion heat transport in an attempt to explain the ion temperature profiles and velocity anisotropies. He was unable to account even qualitatively for the data. The zero dimensionality nature of this study precludes detailed treatment of ion heat transport. Instead the experimental data is used to apply corrections to the zero-D model. This is discussed in detail in Chapter 4.

Spectroscopic Instruments

Relative impurity and neutral densities are derived from spectroscopic data. The primary instrument is a Vacuum Ultraviolet (VUV) monochromator. A high resolution visible monochromator is used for Doppler broadening studies. Four individual line monitors consist of 10 Å bandwidth interference filters and photomultiplier tubes. These instruments view the central, midcylinder plasma. The VUV and visible monochromators view a vertical chord like the microwave interferometer. The line monitors view a chord slightly offset from vertical (to make room for the photomultipliers while using a single port for all four instruments).

Vacuum Ultraviolet Monochromator

The VUV monochromator has 1 Å resolution and is useful for the range of 500 to 3000 Å. It is not absolutely calibrated so only relative intensities are available. The utility of VUV observations is that the strong first excited transition can be directly observed. Typically, the first (Δn=1) state above the ground state is the most probable for electron impact excitation (frequently by a factor of 10). A photon is then emitted in the transition to the ground state. One has, then, a simple system to evaluate where cascade from large Δn excitations can be ignored without (usually) incurring large errors.

Interperting Spectroscopic Data

To obtain densities from intensities is straightforward. The radiation rate is:

$$I = \alpha n_e n_z \langle \sigma V \rangle$$

I =	intensity	α =	constant containing
n_e =	electron density		geometry, efficiency, etc.
n_z =	impurity density	$\sigma(v)$ =	energy dependent electron
v =	relative impurity-velocity		impact excitation cross section.

The mass ratio m_e/m_z is very small ($< \frac{1}{1836}$) allowing the

assumption that the impurities are motionless. This removes the ignorably small ion temperature dependence from I. Note that in principle, one must integrate this across the field of view. Rearranging,

$$\alpha n_z = \frac{I}{n_e \langle \sigma V \rangle}$$

The approximation is made that geometric dependencies are constant in time and may thus be included in α. While consistent with a zero dimensional study, this approximation contributes substantial error for neutrals.

The dominant sources for neutrals are reflection and desorption from the walls. Neutral lifetimes are short in high T_e ($>$10eV) plasmas. One thus expects high neutral densities in the edge of the plasma, and significant burnout in the center. As the edge electron temperatures are cooler than in the center, and since neutral penetration will be density dependent, substantial errors in the average density inferred from spectral intensities are to be expected. These errors are largest when neutral reflux is large and electron temperatures are significant ($\geq$10eV).

The electron density and temperature are measured, as discussed above, to about 10% accuracy. Thus if the excitation cross section energy dependence is known, αn_z can be derived from I, n_e and T_e.

Atomic hydrogen is an important specie in the plasma, so special care was taken to use accurate cross sections. Several approxima-

tions were tried. The simplest was:

$$\sigma(E) \propto e^{-(E-E_0)} \qquad \text{for } E \geq E_0$$

$$= 0 \qquad \text{for } E < E_0.$$

Several forms from Moiseiwitch and Smith[12] (modified Bethe approximations) were used, and finally, an analytically integrable form by Johnson[13] was tried. All produced Maxwellian rate coefficients within 10% of each other, well above threshold.

When the impacting electron energy is close to the excitation energy all approaches to calculating cross sections break down as assumptions are violated. The Maxwellian distribution of electron impact energies dramatically reduces the sensitivity of the excitation rate on the threshold cross section behavior. For electron temperatures below about half the excitation energy, however, Maxwellian averaging becomes ineffective in reducing the sensitivity of rate coefficients to threshold cross section behavior. In such a case, the excitation energy is located in the tail of the distribution. The tail of the distribution can be approximated as a simple exponentially decreasing function e-folding on an energy scale of T_e. Thus as T_e is reduced, Maxwellian averaging actually increases the weighting of the threshold cross section in calculation of rate coefficients. For hydrogen, the first excitation energy threshold is 10.199 eV. Thus errors in rate coefficients due to inaccuracies in threshold cross sections will become significant below

about 5 eV. Recent data[14] indicate Johnson may be in error by a factor of 2 near threshold.

Finally, ZD uses a far simpler approach to calculate rate coefficients. As the code is used to assist in evaluating experimental data, the best available (Johnson's[13]) H^0 rate coefficients are used to accurately infer experimental neutral density. Detailed correspondence between the code and data are not expected at low T_e.

Molecular hydrogen is less amenable to calculation (or measurement) of cross sections than atomic hydrogen. Factor of 10 errors are expected near threshold.[15]

Impurity ions are much easier to treat as the coulomb field dominates the interaction between the incident and orbital electrons. Threshold behavior changes dramatically having an abrupt step at the threshold energy. Consequently, simple approximations yield reasonable results for ions.[12] A single form for the energy dependence of the cross section scaled to the transition energy and normalized to one is used for all ion excitation rates. This is found to incur less than 10% errors for all ion first excited states covered in Moiseiwitch and Smith. Maxwellian averaging smooths out slight errors.

Separate programs were used to calculate the rate coefficients for neutrals. The form of the rate coefficient for ions was calculated as needed due to its simplicity:

needed due to its simplicity:

$$\langle \sigma V \rangle = \frac{e^{-E_0/T_e}}{2\sqrt{T_e}}$$

where:

$\langle \sigma V \rangle$ = normalized rate coefficient

T_e = electron temperature in eV

E_0 = excitation energy in eV

Then the density was calculated normalized to the average value as:

$$\tilde{n}_z = \frac{I}{n_e \langle \sigma v \rangle} \Big/ \int \frac{I}{n_e \langle \sigma V \rangle} dt$$

where

I = measured intensity (arb units)

$\tilde{n}_z$ = normalized impurity density

To summarize, the interpretation of VUV spectroscopic data has a number of constraints. First, only relative intensities are available. This limits analysis of the data to relative impurity and neutral densities. Second, the experiment is treated as zero dimensional. Spatial variations causing variations in excitation rate are ignored. This is most serious for neutrals in $T_e \geq 10$ eV ICRF plasmas where neutral profiles affect the temperature dependence of line of sight integrated spectral intensities. Third, substantial uncertainties in cross sections exist. Errors are largest for neutral species near threshold. Molecular hydrogen is particularly subject to errors, perhaps by a factor of 10. In short, the

data are analyzed with assumptions similar to ZD except that absolute calibration of the instrument is unavailable.

Line Monitors

The Hydra (named for its appearance) consists of four filtered photomultiplier tubes. 10 Å interference filters are used to view visible lines of atomic hydrogen (H_β), CIII, NIII, and OIII. Data are analyzed, and subject to the same limitations as the VUV data. A comparison of inferred relative densities from the Hydra and the VUV monochromator show good correspondence for NIII and OIII (Figure 8). The H_β line is a few angstroms (well within the filter bandwidth) of an oxygen line making its data largely useless. Figure 9 shows the comparison. This instrument is used largely for operational monitoring of machine cleanliness. The close match of the VUV and Hydra data adds confidence to the zero dimensionality assumption as these instruments are separated by 120° toroidally, and view different vertical chords.

Bolometric instruments

Three different instruments are used to measure the total radiated power the plasma emits. An intrinsic barrier detector is a semiconductor device which produces a current proportional to the number of photons incident upon it. A bolometer measures the temperature change of a sensing element. A filtered channeltron[16] yields a signal

proportional to the incident radiation in a wide range, typically the VUV.

The first of those, the intrinsic barrier detector is used primarily as a monitor of machine conditions. This detector counts photons independently of the photon energy. Consequently as T_e rises and the spectrum broadens, the signal from the intrinsic barrier detector drops. Thus it is not useful as even a relative radiated power measure.

A bolometer was constructed from a Veco 'Thinistor'.[17] This sensor is a 1 millimeter square, 0.025 mm thick thermistor. It is mounted in a recessed cavity viewing the plasma. Plasma cannot reach the sensor. Photons and neutrals from a narrow cone centered on a vertical chord through the midcylinder can reach the device.

Thermistors are essentially resistors with large negative temperature coefficients. The specific heat of the device can be easily measured by pulsing a known voltage across the device and then measuring the resultant change in resistance. The sensor can thus be absolutely calibrated. Most of the radiated power is due to VUV line radiation. The thinistor is assumed to absorb all this energy. Neutrals will reflect off the surface about 60% of the time. Reflected particles will deposit about 30% of their incident energy on the thinistor. Thus the thinistor will absorb about 50% of the incident neutral power. (This figure drops dramatically at low energy). If half of the plasma

power loss was due to neutrals, then 25% of the energy deposited on the thinistor is due to these neutrals, and 75% is due to radiation.

The response time of the signal from the thinistor is faster than 10^{-4} seconds. The cooling time scale of the device mounted in vacuum is seconds. Thus the temperature (proportional to resistance) is the integral of the time dependent energy flux onto the device. It was hoped that a time dependent measure of radiated power could thus be constructed by differentiating the voltage required to maintain a constant current through the device.

Such a circuit was built, only to discover that photoelectrons emitted due to the intense flux of ultraviolet photons exceeded the current used to measure the resistance. The resistance measurement probe current cannot be increased as the thinistor is thermally very well isolated. Several elaborate schemes were considered to resolve the problem.

The problem was avoided by using the instrument simply to measure the total energy deposited on it during the entire shot. A sequence of shots with successively shorter RF pulses then allows the change in the time integrated radiated power to be measured as a function of RF power time. Typical data are shown in Figure 10. Note for zero RF, the Thinistor measures the gun only plasma incident power. The derivative of the Thinistor temperature after the shot as a

function of RF pulse time thus yields the radiated power due to RF as a function of time. Such differentiation is noisy (i.e., sensitive to small changes). Usually, other measures of radiated power are integrated to compare with thinistor data.

The Thinistor bolometer is most useful in conjunction with the filtered channeltron. A broad filter (tin-germanium alloy film) is typically used. The channeltron views a horizontal chord through the midcylinder plasma (unlike most other global diagnostics which view a vertical chord). The channeltron output is nearly linear in incident photon energy in the VUV region. Since it is filtered, it measures only photons. Thus it is a reasonable measure of relative radiated power. Dr. Groebner covers the characteristics and operation of this device in detail in his thesis.[16]

A comparison of various filters, and thinistor data is also shown in Figure 10. The close correspondence of the curves gives confidence in the techniques. The different views and locations of the two diagnostics again reinforce the validity of a zero dimensional study.

Shot to Shot Consistency

The diagnostics thus provide a comprehensive set of data in a single shot. Density, electron temperature and the two component ion temperatures are measured versus time. Several measures of radiated power are available, with the filtered channeltron giving time dependent

data calibrated to the bolometric measurement of integrated power from the Thinistor. A single VUV line and four fixed visible line monitors are also digitized.

Multiple shot studies for the Thinistor and VUV scans of many impurities require consistent shot to shot behavior. Figures 11 through 14 give the standard deviation of 24 shots of several critical diagnostics. Primary plasma parameters (n_e, T_e, T_i) yield 5% standard deviations. Indeed, the remarkable consistency of these plasmas is a direct consequence of the strong processes driving the plasma and several feedback effects. Such consistent behavior, and a complete diagnostic set permit the unraveling of the complex, interacting processes controlling the plasma behavior.

References for Chapter 3

[1] J.D. Steben, *J. Appl. Phys.* **43**, 1211(1972).

[2] J.R. Drake, Ph.D. Thesis, University of Wisconsin, PLP-549 (1974).

[8] A.J. Cavallo, Ph.D. Thesis, University of Wisconsin, PLP-628 (1975).

[4] C.M. Fortgang, Ph.D. Thesis, University of Wisconsin (1983).

[5] H.R. Garner, University of Wisconsin. Large Octupole Gettering Area, 1980, PLP-834.

[6] H.R. Garner, Ph.D. Thesis, University of Wisconsin (1982).

[7] H.R. Garner, University of Wisconsin. Digital Multiradian Fringe Shift Interferometer, 1980, PLP-833.

[8] J.C. Sprott, University of Wisconsin. Electrostatic Probe Techniques, PLP-88 (19XX).

[9] F.F. Chen, in Plasma Diagnostic Techniques, R.H. Huddlestone, S.L. Leonard (eds.) (Academic Press, New York, 1965).

[10] J.C. Sprott, *Rev. Sci. Inst.* **39**, 1569(1968).

[11] E.J. Strait, University of Wisconsin. Ion Heat Transport and Temperature Profiles in the Octupole ICRF Plasma: Numerical Modeling and Experiment, PLP-903 (1983).

[12] Moisewitsch, B.I., Smith, S.J., *Rev. Mod. Phys.* **40**, 238(1968).

[13] L.C. Johnson, *Astrophys. J.* **174**, 227(1972).

[14] J. Furst, private communication.

[15] M. Morrison, private communication.

[16] R.J. Groebner, Ph.D. Thesis, University of Wisconsin, PLP-802 (1979).

[17] Victory Engineering Corporation, Springfield, New Jersey. "Thinistor" is a registered trademark of Victory Engineering Corp.

Figure 1: An overview of the Wisconsin Levitated Octupole showing major components of the experiment.

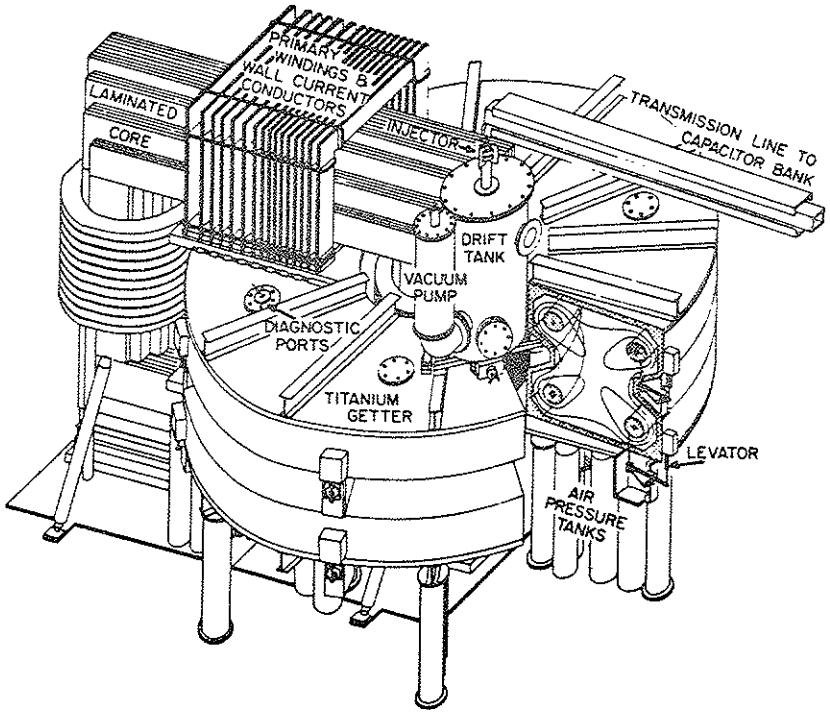

Figure 2: A poloidal section of the machine showing flux surfaces, the separatrix (ψ_s) and the boundary for stable MHD confinement (ψ_{crit}). Units of magnetic flux are Dories where the total flux in the machine is defined as 10 Dories.

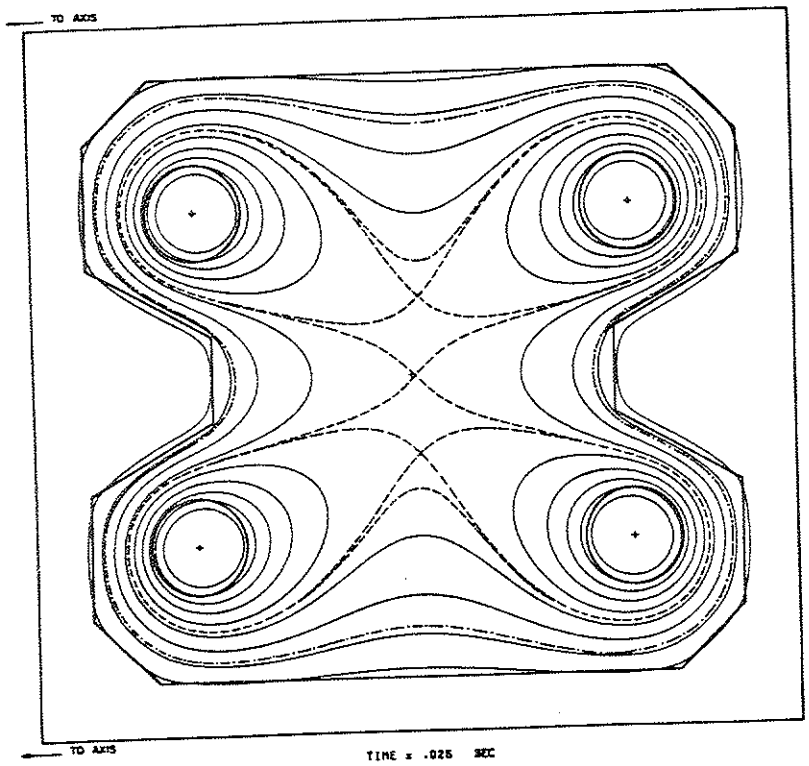

Figure 3: A poloidal section of the machine showing Mod B contours for maximum field. This study used 70% of the maximum possible field, so the field strength of each contour should be reduced by this value. The ICRF resonance shown in the plot is correctly located for the reduced field.

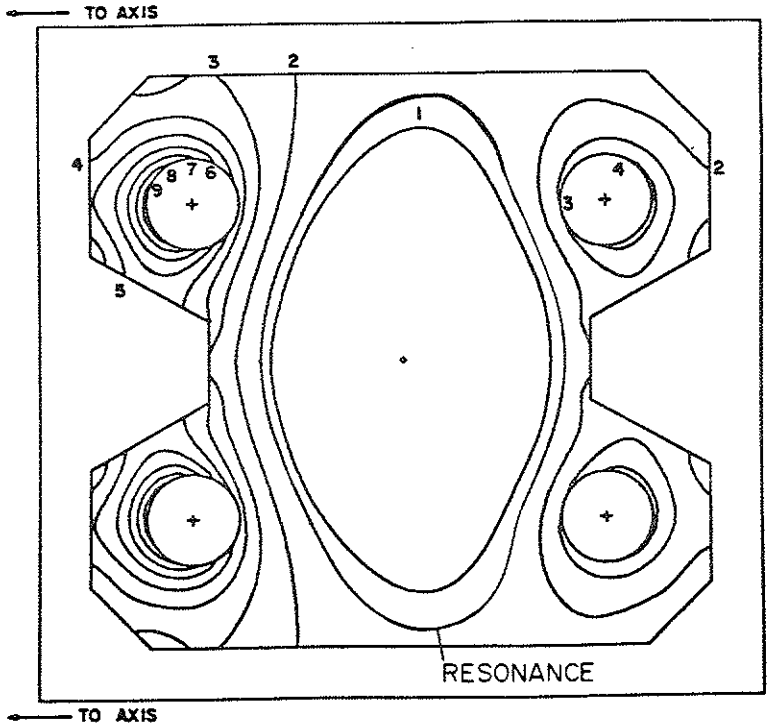

Figure 4: This plot shows the time dependence of the magnetic field normalized to one. Also noted is the timing for the RF pulse. The Marshall gun fires (and defines) t = 0. This occurs 17.2 milliseconds after the poloidal field capacitor bank is fired.

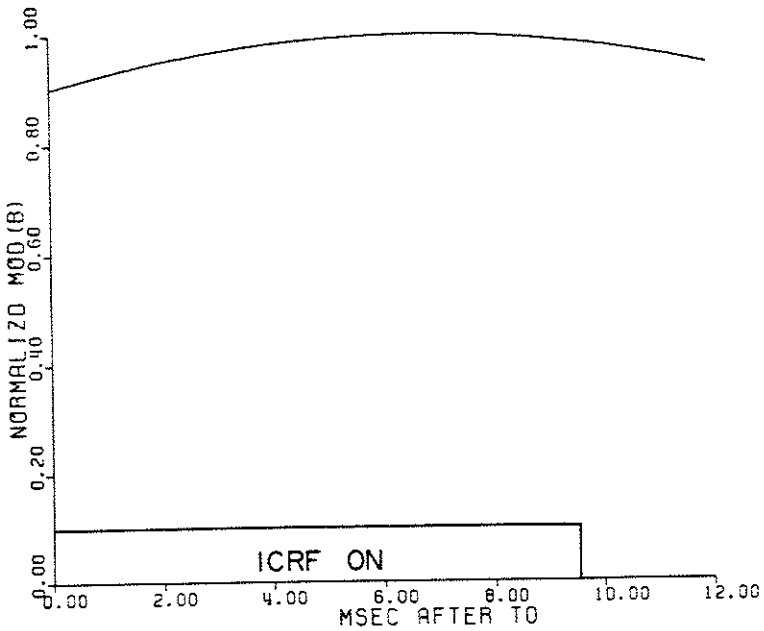

Figure 5: The ion distribution function as measured by the charge exchange analyzer. This plot is taken from Fortgang's thesis.[4]

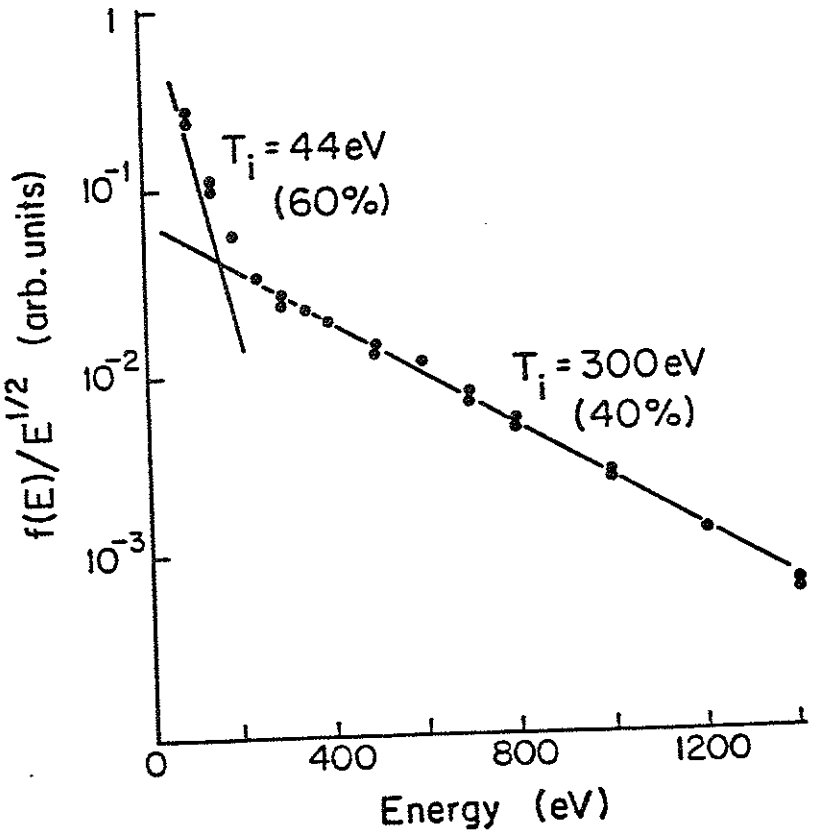

Figure 6: Angular dependence of T_i measured at $\psi = 6.35$ with the gridded ion probe. The angle is relative to the local magnetic field.

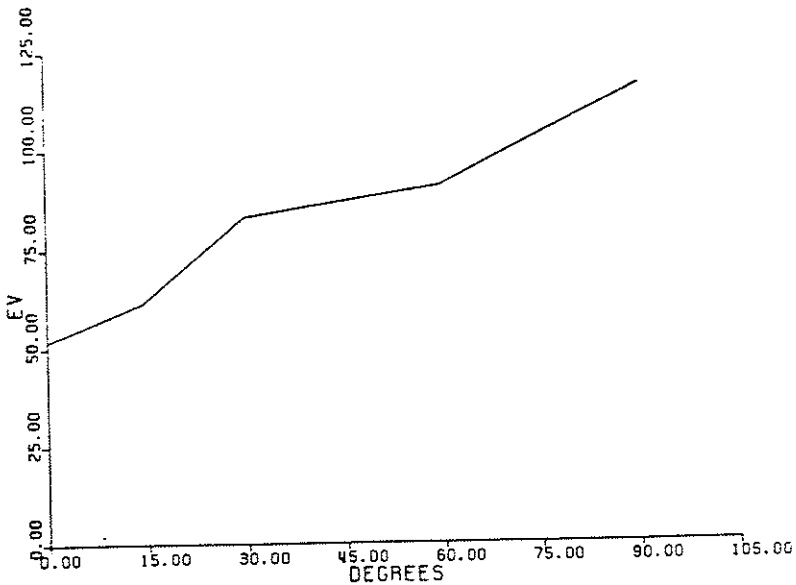

Figure 7: $T_{i\perp}$ and $T_{i\parallel}$ versus position (in flux units) measured with the gridded ion probe.

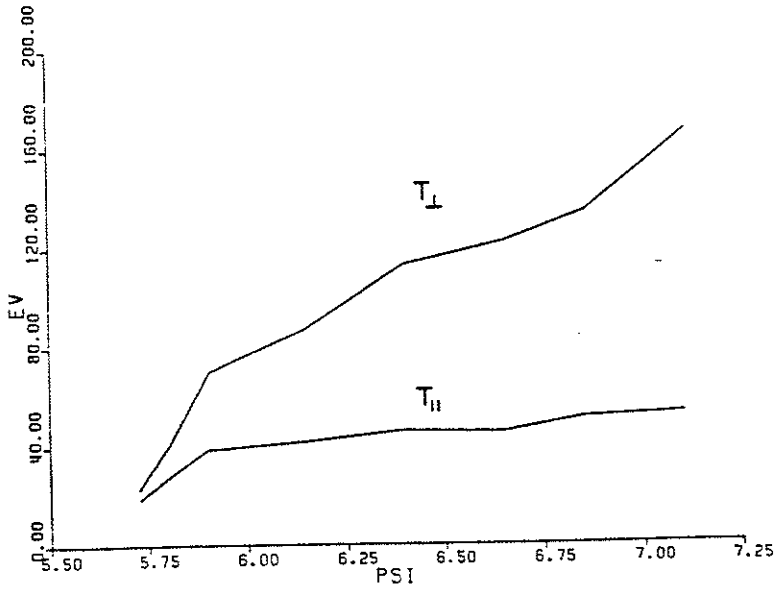

Figure 8: Comparison of Hydra (interference filtered PMT) and VUV monochromator for OIII.

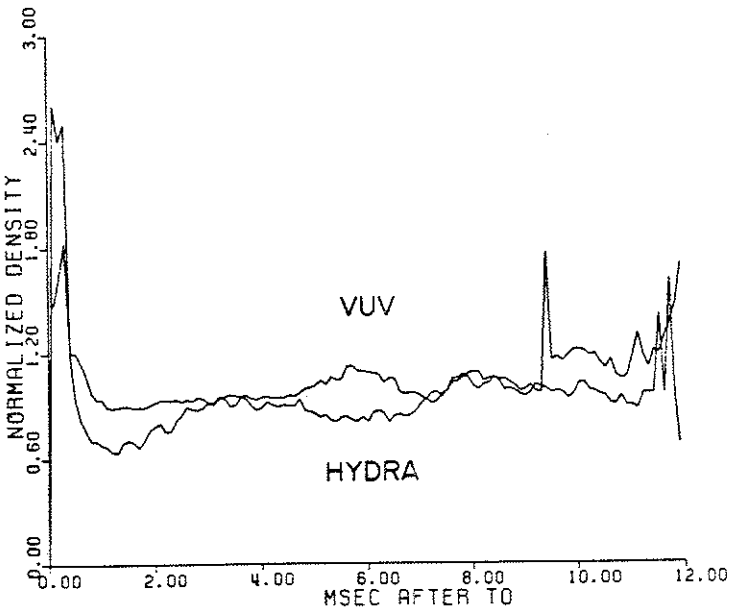

Figure 9: Comparison of Hydra H_β with VUV Lyman α lines.

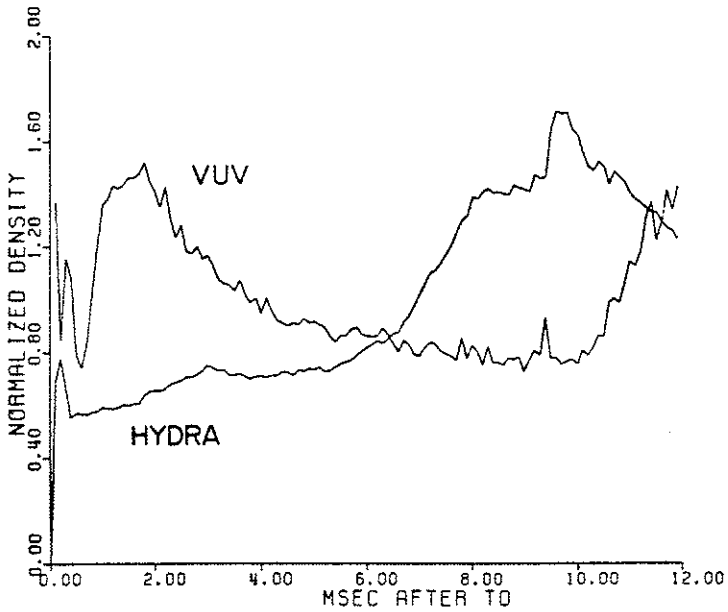

Figure 10: This plot shows the Thinistor bolometer data for a series of shots, and the tin-germanium (SnGe) filtered channeltron. Data are normalized to one for the gun-only shot. Recall the Thinistor responds to neutrals as well as photons.

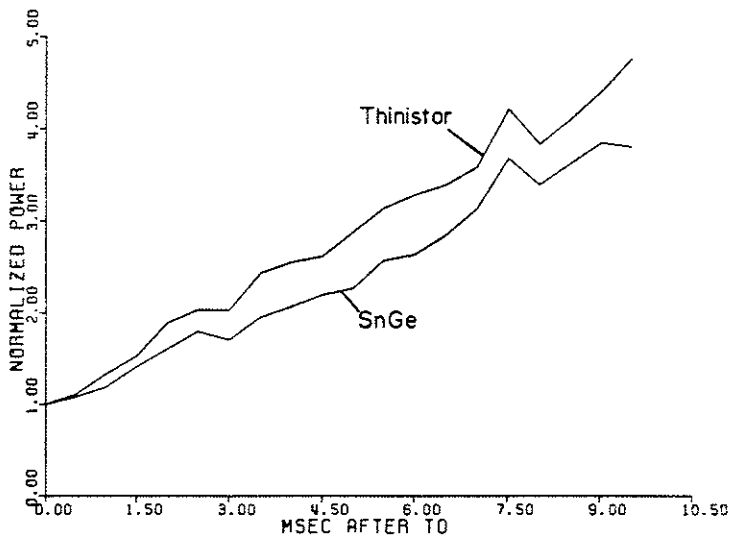

Figure 11: Electron temperature for a standard shot averaged over 33 shots, and the calculated standard deviation (added to, and subtracted from the average in the upper and lower curves).

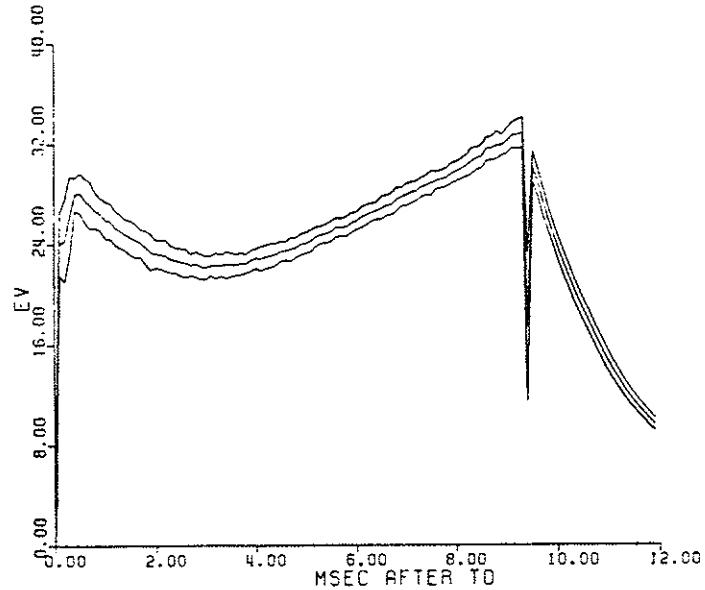

Figure 12: Average electron density and the standard deviation.

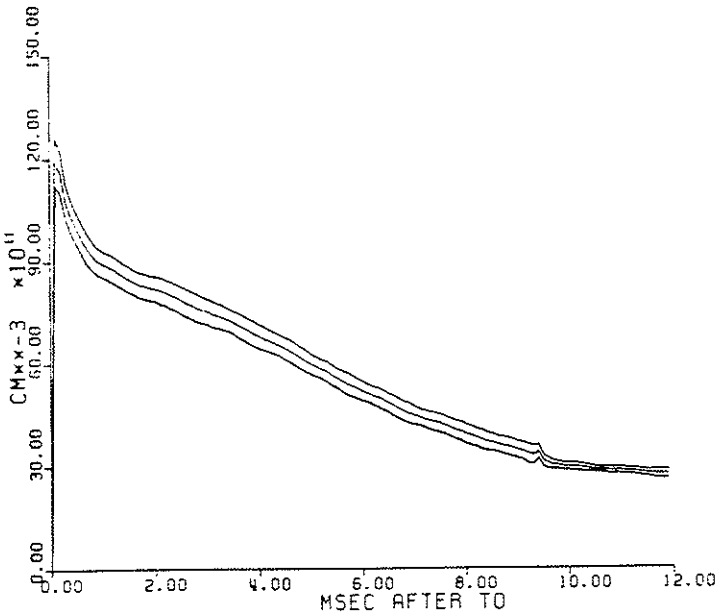

Figure 13: Average Hydra H_β intensity and standard deviation.

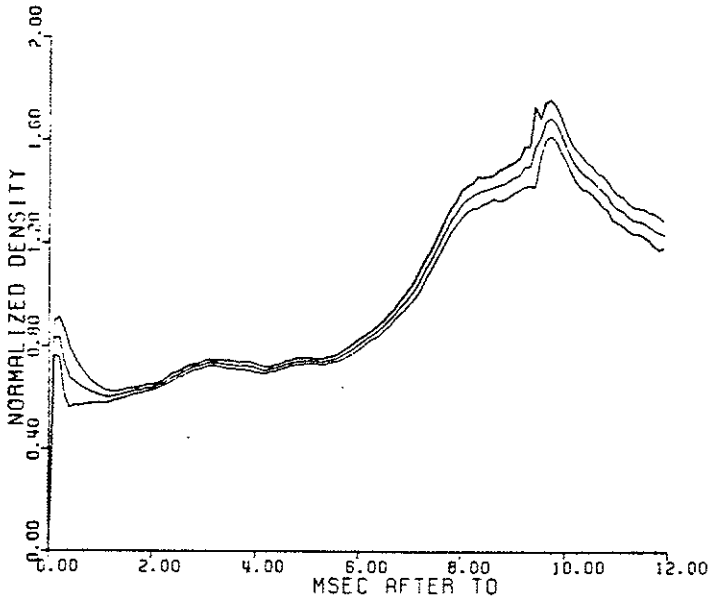

Figure 14: Average SnGe filtered channeltron and standard deviation.

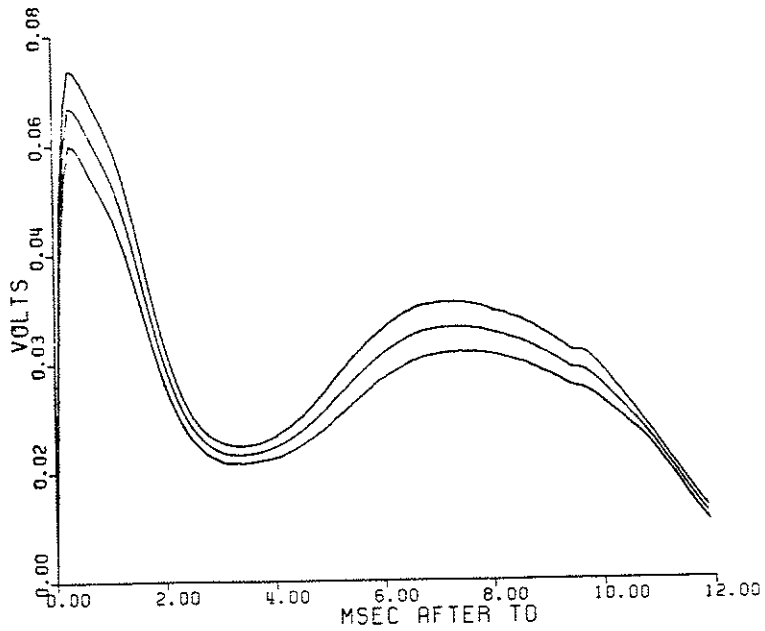

Table 1

Standard Shot Machine and Plasma Parameters

Major radius	140 cm	Minor radius (central)	$\sim$ 45 cm
Vacuum volume	8.6×10^6 cm^3	MHD stable volume	7.7×10^6 cm^3
Half sine field period	43 msec	RF pulse time	9.5 msec

Poloidal field (at 3.5 kV on capacitor bank) maximum B at:

Inner ring surface	8.1 kG
Outer ring surface	3.9 kG
Wall (at nose)	5.9 kG

	Initial	Final (9.5 msec)
Electron temperature	28 eV	36 eV
Electron density	1.0×10^{13} cm^{-3}	3.5×10^{12} cm^{-3}
Ion temperature at center	28 eV	50 eV
Ion temperature at edge	28 eV	270 eV

RF power coupled to the plasma	500 kW
Total plasma kinetic energy (typical)	570 Joules
Energy confinement time (typical)	1.1 msec

CHAPTER 4

MODELS

Coronal Equlibrium Codes

Models, and particularly ZD, play a prominent role in this study. This chapter covers the physics used in the model, the assumptions implicit in the code, and limits in its use and validity. Chapter 2 gave a number of constraints codes must comply with, and discussed the zero-D limitation and basic evolver technique. ZD grew from small coronal equilibrium codes used to study impurity radiation. A review of these codes and their application is instructive.

In late 1980, the ICRH oscillator and antenna were installed on the Octupole. Preliminary results were disappointing. A 10^{13} cm^{-3} target plasma typically achieved only 20 eV T_e with 2 Mw oscillator input power. This represented about 1/2 MW coupled to the plasma. A calculation of input power/cm^3 provided the first indication that the 'impurity barrier' had been reached. With a plasma volume of 5×10^6 cm^3, input power is 0.1 W/cm^3. Tokomaks typically require about 1 W/cm^3 to burn out (completely strip) low Z impurities.[1]

A non-time dependent coronal equilibrium code demonstrates that a 0.3% carbon plus 1% oxygen impurity level would account for the observed behavior of T_e *vs* input power (Figures 1 and 2). To confirm the dominance of impurity radiation, the total radiated power was measured as nitrogen was added to the plasma. No increase in total radiation was observed (Figure 3) as nitrogen line intensity increased an order of magnitude (Figure 4) and the electron temperature dropped to 8 eV. Numeric agreement between the measured radiated power (all the input power) and the coronal equilibrium code was within experimental error of doping level and input power. While this test established impurity line radiation as the dominant loss mechanism, it raised a number of questions.

Why did the modeling work so well? The experiment is in gross violation of the time scales for coronal equilibrium (by a factor of 100). Where did the impurities come from?

The source of impurities could be the wall, or they could be injected from the Marshall gun. Russel Hulse (PPPL) made the observation that the gun plasma is appropriately modeled by Local Thermodynamic Equilibrium (LTE), not coronal equilibrium. The plasma density within the gun is about 10^{18} cm^{-3}, well above the coronal limit for OVIII.[3]

In LTE an excited state does not have time to decay to the ground state before being excited again. This has two consequences: The time scales are fast enough that the 10 μsec lifetime of the gun plasma permits LTE to be established and multiple collisions can transfer energy to the impurity, dramatically reducing the electron tempera-

ture required for ionization. Thus the gun plasma completely strips low Z impurities of electrons. The gun plasma then enters the Octupole, where its density drops by five orders of magnitude. Recombination times for highly stripped ions are now fractions of a second. No single electron has sufficient energy to excite the ion. In effect, the impurity charge state distribution is frozen and line radiation from these impurities impossible. Thus gun injected impurities are not directly observable, although they do increase (Z) and will interact with the wall. The impurity source is thus inferred to be the wall.

It was, however, the violation of the time scales for coronal equilibrium which motivated the writing of time dependent coronal codes. The equilibrium time scale is established by the slowest ionization time (equal to the recombination time in equilibrium). This yields the simple time scale[3] for approach to coronal equilibrium of $\tau = \frac{10^{12}}{n_e}$. For a 10^{13} cm^{-3} density, $\tau = 0.1$ sec, or about 100 times the observed radiated power time scale.

Early versions of ZD resolved this issue a year later. This time-dependent coronal code produced the total radiated power as one of its outputs. When T_e and all densities were forced to remain constant, the evolution of an initially neutral impurity could be followed as it approached equilibrium. The 0.1 sec equilibrium time scale is seen in the density of the highly stripped ions (Figure 5). The total radiated power, however, has a much shorter time scale (Figure 6).

It became obvious (in retrospect) where the difficulty lay. The equilibrium time scale is for the slowest process, using an ionization energy about six times the electron temperature. Radiated power, however, should use an excitation rate for a state energy two to three times T_e since, beyond this, power is reduced by lower excitation rates and ionization rates are close to excitation rates.

Terms in ZD

As mentioned in Chapter 3, ZD keeps track of particle and energy density (n and E) for each specie. Thirty sets of processes generate rates of change for n and E (dn/dt and dE/dt). A wide range of time scales exist as the plasma evolves. Standard predictor-corrector techniques are used to adjust the integration time step while retaining accuracy. Several of the equations being integrated are extremely stiff. Consider the temperature of fully stripped oxygen ions. The dominant term is coupling to the bulk ions:

$$\frac{dT_0}{dt} = \nu_\epsilon (T_i - T_0)$$

where

T_0 = O^{+8} ion temperature

T_i = H^+ ion temperature

ν_ϵ = energy transfer collision frequency

For $T_e = T_i = 10$ eV, at $n_e = 5 \times 10^{12}$ cm^{-3}, $\nu_\epsilon \sim 10^6$ sec^{-1}. So,

while T_i changes slowly, T_0 will follow T_i closely. But note that a tiny error in T_0 will yield a huge dT_0/dt. In fact, the numeric precision (1 part in 10^7) of the computer limits the step size to microseconds for reasonable accuracies.

Innovative approaches to integrating such equations are necessary. The method used is an averaging third order predictor and an averaging second order corrector with step size control dependent on stiffness as well as predictor-corrector difference. Extensive testing shows the technique outperforms the standard fourth order Adams-Moulton-Bashforth fourth order predictor-corrector[4] in both accuracy and efficiency.

The processes considered by ZD are given in Table 1. The calculation of each of these terms is covered below. It is essential to note that all species are assumed to have a Maxwellian velocity distribution. The various approximations and limitations noted in the following sections are collected in a later section.

Elastic Electron Scattering on Ions

This term gives the energy transfer between electrons and the i^{th} ionic species. Maxwellian distributions and zero relative average velocity are assumed. Unless otherwise noted, units are CGS with temperatures in eV, magnetic field in gauss, and $\mu_i = m_i/m_p$ is the dimensionless mass normalized to a proton mass.

A form giving the rate of change of the energy density (rather than the usual[5] (dT_i/dt) is used:

$$n_i \frac{dT_i}{dt} = n_i \overline{\nu}_e (T_e - T_i) \times 1.602 \times 10^{-19} \frac{\text{watts}}{\text{cm}^3}$$

where n_i is the ion density, $T_{i,e}$ are temperatures in eV and $\overline{\nu}_e$ is the energy equipartition collision frequency given by[5]

$$\overline{\nu}_e = 8.8 \times 10^{-20} \frac{(m_e m_i)^{\frac{1}{2}} Z_i^2 n_e \lambda_{ei}}{(m_e T_i + m_i T_e)^{\frac{3}{2}}} \sec^{-1}.$$

The coulomb logarithm for $T_e < 10$ eV is

$$\lambda_{ei} = 23 - \ln \{ n_e^{\frac{1}{2}} Z_i T_e^{-\frac{3}{2}} \}$$

and for $T_e > 10$ eV

$$\lambda_{ei} = 24 - \ln \{ n_e^{\frac{1}{2}} T_e^{-1} \}$$

where $T_e > T_i$ m_e/m_i has been assumed. By conservation of energy the change in electron energy density is

$$n_e \frac{dT_e}{dt} = -\sum_i n_i \frac{dT_i}{dt}.$$

The accuracy of this term is of order λ^{-1}, typically 10%. For ICRF plasmas, this term is the dominant electron energy source. Note that while ion-ion coupling is 1/43 as strong as ion-electron coupling, highly stripped impurity ions can couple more strongly (as Z_i^2) to both

H^+ and e^-. Thus the path $H^+ \rightarrow$Impurity$\rightarrow e^-$ can contribute a non-negligible fraction of the total electron input power. The electron ion term just described covers the latter half of this path. Ion-ion coupling is next.

Elastic Ion-Ion Scattering

This term covers the energy transferred from the i^{th} to the j^{th} charged ionic species. This form is quite similar to the electron-ion coupling term. The rate of change of energy density of the i^{th} specie is

$$n_i \frac{dT_i}{dt} = n_i \overline{\nu}_\epsilon (T_j - T_i) \times 1.602 \times 10^{-19} \frac{\text{watts}}{\text{cm}^3}$$

with $\overline{\nu}_\epsilon$ cast in a more convenient form:[5]

$$\overline{\nu}_\epsilon = 6.804 \times 10^{-8} \frac{(\mu_i \mu_j) Z_i^2 Z_j^2 \lambda_{ij}}{(\mu_i T_j + \mu_j T_i)^{\frac{3}{2}}} \text{ sec}^{-1}$$

$$\lambda_{ij} = 23 - \ln\left\{ \frac{Z_i Z_j (\mu_i + \mu_j)}{\mu_i T_j + \mu_j T_i} \left[\frac{n_i Z_i^2}{T_i} + \frac{n_j Z_j^2}{T_j} \right] \right\}.$$

Again, conservation of energy is used to determine the power density lost from the j^{th} specie (thus halving the computation time). Accuracy for this term is also of order λ^{-1}. Maxwellian distributions are assumed.

Elastic Ion-Neutral Scattering

Isotropic scattering and a constant cross section are assumed.

Explicitly, $\sigma = 5 \times 10^{-15}$ cm^2 is assumed independent of interaction velocity, incident and target particle mass, ionic charge, and nuclear charge.[5] A collision is modeled kinetically as follows. The scattering collision frequency is $\nu_s = n\sigma V$. The interaction velocity $V = \sqrt{\frac{T_a}{m_a} + \frac{T_b}{m_b}}$ is assumed to be the vector sum of the thermal velocities. This gives the collision frequency for scattering. Isotropic scattering will evenly distribute the probability of energy transferred between zero and a maximum of $E_0 (\frac{m_a - m_b}{m_a + m_b})^2$. Thus to calculate the power density transferred, 1/2 the maximum energy transfer is assumed and

$$P_{a \rightarrow b} = n_a \nu_s (T_a - T_b) 1.602 \times 10^{-19} \left(\frac{1}{2} - \frac{1}{2} (\frac{m_a - m_b}{m_a + m_b})^2 \right) \frac{\text{watts}}{\text{cm}^3}.$$

Numerically,

$$P_{a \rightarrow b} = 7.84 \times 10^{-28} n_a n_b \sqrt{\frac{T_a}{\mu_a} + \frac{T_b}{\mu_b}} (T_a - T_b) \left(\frac{1}{2} - \frac{1}{2} (\frac{\mu_a - \mu_b}{\mu_a + \mu_b})^2 \right) \frac{\text{watts}}{\text{cm}^3}.$$

Note that the power transferred to neutral hydrogen species is substantial. This process can raise the temperature of H_2 in the bridge region from 0.02 eV to about 1/2 the ion temperature during the short (10^{-5} sec) H_2 lifetime. The energy thus coupled to H_2 determines the H_2 velocity, hence the time it takes H_2 to transit the plasma. Since the transit time is comparable to the dissociation and ionization times, neutral ion scattering plays a primary role in determining the plasma fueling rate.

There are a number of weaknesses in the treatment of neutral elastic scattering. Forward scattering is much more probable for electrons. The constant cross section is based on atomic size, hence ignores all quantum effects. The scaling with velocity and mass is reasonable, however. Thus the fault to be found in this treatment is that the estimate of the cross section is in error. Since electrons couple weakly to the neutrals compared to the ions, we are primarily interested in the ion-neutral cross section. Here, because of the low velocity and large mass, scattering will indeed be isotropic.

Inelastic Electron-impurity Interactions

This section covers inelastic electron events: Bremßtrahlung ionization, recombination, and excitation. All these processes except bremßtrahlung require extensive quantum treatment. Before covering the details of the rate calculations, the use of the rates in ZD will be discussed.

Processes Which Change Ion Density

For the i^{th} species, all ionization and recombination processes remove particles. Rates for the various processes are calculated per electron per ion. So

$$\frac{dn_i}{dt} = -n_e n_i \{R_{ionizi} + R_{radreci} + R_{diereci} + R_{3breci}\} \text{ cm}^{-3}\text{sec}^{-1}$$

where (rate coefficients having dimensions of $\text{cm}^3\text{sec}^{-1}$)

R_{ioniz} = ionization rate

R_{radrec} = radiative recombination rate

R_{dierec} = dielectronic recombination rate

R_{3brec} = 3-body recombination rate

n_e = electron density

n_i = i^{th} specie density

Changing the particle density also changes the energy density as particles carried to other species carry their thermal energy. Thus

$$\frac{dE_i}{dt} = -\frac{dn_i}{dt} T_i \times 1.602 \times 10^{-19} \frac{\text{watts}}{\text{cm}^3}.$$

Having removed particles from the i^{th} specie, they must now be put somewhere. Ionization of the i^{th} specie sources particles (and energy density) to the $(i+1)^{th}$ specie. (Species are ordered by ionization state. Fully stripped ions don't ionize and neutral particles don't recombine.) Recombination of the i^{th} specie transfers particles (and energy) to the $(i-1)^{th}$ specie:

$$\frac{dn_{i+1}}{dt} = n_e n_i R_{ionizi} \text{ cm}^{-3}\text{sec}^{-1}$$

$$\frac{dE_{i+1}}{dt} = n_e n_i R_{ionizi} T_I \times 1.602 \times 10^{-19} \frac{\text{watts}}{\text{cm}^3}$$

$$\frac{dn_{i-1}}{dt} = n_e n_i \{R_{radreci} + R_{diereci} + R_{3breci}\} \text{ cm}^{-3}\text{sec}^{-1}$$

$$\frac{dE_{i-1}}{dt} = n_e n_i \{R_{radreci} + R_{diereci} + R_{3breci}\} T_i \times 1.602 \times 10^{-19} \frac{\text{watts}}{\text{cm}^3}$$

Effects on Electrons due to Impurity Interactions

Changes in the electron particle density due to ionization and recombination are not explicitly calculated. Rather, overall charge neutrality at each time step is forced by setting $n_e = \sum_i n_i q_i$. The electron energy lost in recombination is all radiated away. These radiation rates are calculated (in watts/cm^3/electron/ion). Collisional excitation rates for impurities and neutrals are also calculated. This term is the critical line radiation term. Ionization simply removes the ionization energy from the electrons. For each specie i, then

$$\frac{dE_e}{dt} = -n_e n_i \{P_{radreci} + P_{diereci} + P_{bremi} + P_{execi} + R_{ionizi} E_{ionizi} \times 1.602 \times 10^{-19}\,\mathrm{J/eV}\} \frac{\mathrm{watts}}{\mathrm{cm}^3}$$

where

P_{radrec} = radiated power due to radiative recombination

P_{dierec} = radiated power due to dielectronic recombination

P_{brem} = radiated power due to bremßtrahlung

P_{exec} = radiated power due to collisional excitation

E_{ioniz} = ionization energy (eV)

The various radiated powers are summed to generate a total radiated power for output.

Throughout, a Maxwellian electron distribution is assumed. The ion and neutrals are assumed at rest relative to the electrons.

Both assumptions follow from the small mass of the electron. Also note that momentum exchange between electrons and impurities is ignored for these processes. This leads to an error in the thermalization of impurities. This error is small as electrons are much less effective than ions in coupling thermal energy to the impurities. Also note that elastic scattering (electron-ion and electron-neutral) is about the same size as inelastic scattering momentum coupling. Thus the elastic scattering process hides our sins by being close to correct for a process we ignored (inelastic momentum transfer), with both processes being small compared to ion coupling.

The calculation of the various rates for impurity processes is non-trivial. This section of ZD is a modified version of a code written by D.E. Post and R. Hulse at PPPL.[6] Most of the rates needed are not available from either experimental data or detailed quantum codes. Since the primary concern of this study is the average behavior of a specie rather than the detailed behavior of particular states, a 'simple' calculation can be done. This approach imposes several restrictions.

First, the assumption of coronal equilibrium that all electron interactions occur with the impurity in the ground state is strictly enforced. Thus the metastable states with long lifetimes are ignored. Metastable states typically have nearby states which are energetically easily accessible. Thus they are likely to be collisionally de-excited at our electron densities.[7]

Second, such an approach will not produce accurate excitation rates for particular spectroscopic lines. The sum of many lines yields the radiated power for the specie. Other rates are also calculated as sums over many states. The accuracy of the sums is far better than the accuracy for a single state in the approximations used.

Generally, the calculations for atomic quantum phenomena can be reduced to sums over accessible states of terms involving the oscillator strengths and energies of the states. In ZD atomic states are calculated considering only the principal quantum number (n). Angular momentum (ℓ) is ignored. (This approximation is not optional. Inclusion of ℓ terms would square the computing involved taking a 10 second Cray run to 10^{10} seconds.) $\Delta n = 0$ transitions are handled as a special case.

Only the first ten shells are considered. About half of the transitions contributing to line emission are $\Delta n = 0$, with decreasing contributions as Δn increases. The shells are filled in order with $2n^2$ electrons per shell. The energies for electrons in each shell, for transitions between all possible pairs of shells, and the ionization energy are calculated using the Pauli approximation to the Dirac energy equation based on the shielded nuclear charge at that shell. Shielding coefficients are tabulated for each shell and configuration. Critical elements (all impurities studied) use tabulated ionization energies.

Absorption oscillator strengths are calculated as corrections to

hydrogenic values for each possible transition. $\Delta n = 0$ transitions are treated as a single effective transition. Because of the importance of small n, small Δn transitions (they are the most probable) tabulated values are used. Corrections include (for $n \rightarrow m$ transitions) the population of the n^{th} shell, the vacancies in the m^{th} shell, as well as energy and shell dependent corrections.

All the energies and oscillator strengths are calculated only once for each charge state of each atomic species. These values are dependent only on atomic properties, not plasma parameters.

First, collisional ionization of an electron in the n^{th} shell occurs at a rate of:

$$R_{ioniz} = 5.88 \times 10^{-7} n_z n_e T^{\frac{1}{2}} \exp\left(-\frac{I_{q,n}}{T}\right) \times \left(1 - \exp\left(-\frac{I_{q,n}}{T}\right)\right)\left(\frac{13.6}{I_{q,n}}\right)^2 \Gamma_{q,n} \mathrm{cm}^3 \mathrm{sec}^{-1}$$

$I_{q,n}$ = ionization energy for ionization state q, shell n in eV

T = electron energy in eV

n_e = electron density

n_z = impurity ion density

$\Gamma_{q,n}$ = Gaunt factor

The Gaunt factor is the quantum mechanical correction to the otherwise classical calculation of the cross section. Bekefi[8] and Allen[9] cover the calculation of Gaunt factors in general and the reader is referred to these texts as well as the references in Post[7] for details. Typically,

when averaged over a Maxwellian electron distribution, Gaunt factors are between 1 and 2. The rates for each shell are summed after being multiplied by the number of electrons in the shell. Radiation from inner shell ionization is ignored.

Radiative recombination is the simple process of electron capture, with radiation removing the excess electron energy and ionization energy. The rate is calculated for capture to each unfilled shell. A factor of 5 correction is applied to the highest ($n = 10$) shell to account for the rest of the higher lying shells. Unity Gaunt factors are used in light of uncertainties in the rest of the calculation. The recombination rate to shell n is

$$R_{radrec_n} = 5.2 \times 10^{-14} q(\frac{I_{q,n}}{T})^{\frac{3}{2}} \exp(\frac{I_{q,n}}{T}) E_1(\frac{I_{q,n}}{T}) \mathrm{cm}^3 \mathrm{sec}^{-1},$$

where

E_1 = the first exponential integral

q = the shielded nuclear charge for the shell.

Radiated power from radiative recombination has two sources: the continuum radiation as the electron is captured in the n^{th} shell, and line radiation as the excited ion makes transitions to the ground state. Note that it is irrelevant how these transitions occur. Multi-photon decay will radiate the same power as a single transition. Thus the power due to line radiation is just the sum over unfilled shells of the recombination rate to state n times the energy above the ground state

of that shell. The continuum power factor is

$$P_{contin_n} = 8.32 \times 10^{-30} q(\frac{I_{q,n}}{T})^{\frac{1}{2}} I_{q,n} \frac{\mathrm{watts}}{\mathrm{cm}^3}.$$

Dielectronic recombination involves the free electron interacting with a bound electron, leaving both electrons in bound, excited states. Further, this excited state must have a low probability of ejecting an electron. The technique used is that of Burgess,[10] modified by Merts *et al.*[11] Essentially this approximation rests on an empirical (i.e., not theoretically justified) fit to an extremely involved quantum calculation. A 20% error is claimed for $Z < 20$ in the range of electron energy where dielectronic recombination is important. $\Delta n = 0$ transitions are treated in a similar manner, with a modified set of fits.

The dielectronic recombination rate for an electron in shell n interacting with the free electron is:

$$R_{dielec_n} = 7.59 \times 10^{-14} \frac{B(q)D(q,T)}{T^{\frac{3}{2}}} \sum_i f_{i,n} A(Y) \exp(-\frac{\overline{E}}{T}) \mathrm{cm}^3 \mathrm{sec}^{-1}$$

where

n = the initial state

q = ionic charge

$f_{i,n}$ = the oscillator strength for the $n \rightarrow i$ transition

$Y = (q+1)E_{in}$

$E_{i,n} = \dfrac{\mathcal{E}_i - \mathcal{E}_n}{13.6(q+1)^2}$ $\mathcal{E}_i$ - electron energy in i^{th} shell

$B(q) = q^{\frac{1}{2}}(q+1)^{\frac{3}{2}}(q^2+13.4)^{-\frac{1}{2}}$

$$\overline{E}/T = (q+1)^2 E_{i,n}/(73.5aT)$$

$$a = 1 + 0.015q^3/(q+1)^2$$

for $\Delta n = 0$ transitions (Merts *et al.*)[11]

$$A(Y) = Y^{\frac{1}{2}}/(1 + 0.105Y + 0.015Y^2)$$

$$D(q,T) = \frac{n_t/200}{1 + n_t/200}$$

$$n_t = (4.77 \times 10^{18} q^8 T^{\frac{1}{2}}/n_e)^{\frac{1}{2}}$$

for $\Delta n \neq 0$ transitions

$$A(Y) = \frac{Y^{\frac{1}{2}}/2}{1 + 0.210Y + 0.030Y^2}$$

$$D(q,T) = \frac{0.0015[(q+1)n_T]^2}{1 + 0.0015[(q+1)n_T]^2}$$

The power radiated has components from both the captured and the excited electron. The captured electron always radiates the ionization energy (in at least two photons).

Three body recombination is a process in which two free electrons interact near an ion leaving one electron captured by the ion. At low densities (such as the Octupole's) this is a very infrequent occurrence and thus may be treated simply. The rate[11] is

$$R_{3brec} = 8.75 \times 10^{-27} \frac{q^3 n_e}{T_e^{9/2}} \mathrm{cm}^2 \mathrm{sec}^{-1}$$

where

q = ionic charge

n_e = electron density

T_e = electron temperature in eV

Note that the overall dependence of the rate is n_e^2. Radiation from this process is ignored.

Bremßtrahlung is an even weaker process in the Octupole's cold plasmas. It is included only because it is trivial to calculate, and for completeness. The Gaunt factor for this process is taken as 1.2.

$$R_{brems} = 1.53 \times 10^{-32} q^2 T_e^{\frac{1}{2}} \times g_{ff}$$

T_e = electron temperature in eV

q = ion charge

g_{ff} = free-free Gaunt factor = 1.2.

Finally, collisional excitation is the dominant electron energy loss mechanism. The electron excites the ion (or neutral) which then decays to the ground state, emitting a photon. Note that the decay path (single photon or multiple) is irrelevant since only the radiated power is of interest. The rate for excitation from the n^{th} shell to the j^{th} shell can be written in the form

$$P_{exec}^{n,j} = 1.58 \times 10^{-8} \frac{f_{n,j}}{T^{\frac{1}{2}}} \exp(-\frac{E_{n,j}}{T}) g_{n,j} \mathrm{cm}^3 \mathrm{sec}^{-1}$$

where

$f_{n,j}$ = oscillator strength for $j \rightarrow n$ transition

T = electron temperature in eV

$E_{n,j}$ = excitation energy in eV

$g_{n,j}$ = Gaunt factor for the transition

The total radiated power is the sum over all electrons and all possible final states. Due to the importance of this term, care is taken to insure the best possible accuracy. Most of this effort occurs in calculating oscillator strengths. The oscillator strengths are calculated for a shell and have the fractional occupancy of the shell included. Thus the excitation rate need only be summed over initial shell, not all electrons. Again $\Delta n = 0$ transitions are handled as a single effective transition.

The Gaunt factor for $\Delta n \neq 0$ is taken as

$$g_{i,j} = 0.19\Big(1 + 0.9\Big\{1 + \frac{j(j-i)}{20}[1 + (1 - \frac{2}{z})\frac{E_{i,j}}{T}]\Big\} \times \exp(\frac{E_{i,j}}{T})E_1(\frac{E_{i,j}}{T})\Big)$$

where

$E_{i,j}$ = energy difference between shells i and j

E_1 = first exponential integral

T = electron temperature

z = nuclear charge

For $\Delta n = 0$, the Gaunt factor has different forms for neutral and charged impurities.

$$g_{nn} = C_{nn} + 0.276\exp(\frac{E_{nn}}{T})E_1(\frac{E_{nn}}{T})$$

where

$$C_{nn} = \begin{cases} d_{nn}\big(1 - \dfrac{\gamma_{nn}}{(q-1)}\big) & \text{charged} \\ \dfrac{0.06}{1 + E_{nn}/T}\Big((\dfrac{E_{nn}}{T})^{\frac{1}{2}} - 2\Big) & \text{neutral} \end{cases}$$

The overall accuracy of the impurity rate coefficients is claimed to be a factor of 2.[2,7] Accuracy degrades for Z > 20 (dielectronic recombination) and for low T_e. The T_e limit is $\sim$ 3 eV for low Z impurities and 10-20 eV for high Z impurities. This is due to the increased likelihood of $\Delta n = 0$ transitions at low energies. This in turn violates the single effective transition treatment of this class of transitions.

There are a few cases where the hydrogenic ion approximation used generates substantial errors. A case in point is TiIII autoionization. There exists a state just above the ionization energy for ionization from an inner electron. This enhances the ionization rate by an order of magnitude.[2]

In retrospect it is easy to see why the code is useless for detailed spectroscopic work. The hydrogenic model, lack of angular momentum, and the cavalier treatment of decay of excited states (ignoring decay path) all make explicit line radiation intensities unavailable. Even the calculation of the electron temperature dependence of $\Delta n \neq 0$ intensities would be close to useless. This has all been sacrificed to make the rate calculations computationally reasonable. Remember that for the broad range of ionization states and impurities under study this code is the best currently available.

In the interests of computational efficiency, ZD obtains these rates by interpolation into precalculated tables. Values of rate coef-

ficients are stored for 5% increments of electron temperture. Accuracy of the interpolated values was tested and found to be 1% of the directly calculated values except at low energies. When the electron temperature is well below the threshold for a process, the rate coefficient is roughly exponential (due to the Maxwellian averaging). This increases the curvature of the rate coefficient versus energy function. Accuracy degrades to a factor of 2 in extreme cases. All such cases, however, have ignorably small ($< 10^{-25}$ $cm^3 sec^{-1}$ per electron per ion) rate coefficients. The errors incurred by interpolating are thus irrelevant to the accuracy of the codes results.

Special Cases

Rate coefficients are not generated for charge exchange or molecular species as in the previous section. These processes are handled with published polynomial fits from tabular data.[12,13] Molecular densities are quite small at the electron temperatures under study. Since line radiation dominates the electron energy loss rate the simple estimates for energy transfers in some of the processes are acceptable.

$$H^0 + H^+ \rightarrow H^+ + H^0$$

The rate for atomic hydrogen charge exchange is known to $\pm 10\%$.[12,14] The 'interaction temperature' is taken as $T = (T_{H+}^2 +$

$T_{H^0}^2)^{\frac{1}{2}}$ to accomodate energetic neutrals. The change in specie due to charge exchange (charged to neutral and *vice versa*) modifies the energy density as the two species, in general, will be at different temperatures.

$$\frac{dE_n}{dt} = n_n n_i R_{CX}(T_i - T_n) 1.602 \times 10^{-19} \frac{\text{watts}}{\text{cm}^3}$$

E_n = neutral energy density

n_n = neutral density

T_n = neutral temperature (eV)

T_i = ion temperature (eV)

R_{CX} = charge exchange rate (ions to neutrals)

$$H^+ + H_2 \rightarrow H^0 + H_2^+$$

Charge exchange on molecular hydrogen is handled as in atomic hydrogen charge exchange. The particles exchange charge carrying their thermal energy to the new species.

$$H_2 + e \rightarrow 2H^0 + e$$

Neutrals generated by dissociation of molecular hydrogen pick up the binding energy (4.7 eV) plus some of the electrons' energy. These Franck-Condon neutrals have an energy of about 3.5 eV each. Thus two hydrogen neutrals and 7 eV plus the thermal H_2 energy are added to the atomic hydrogen neutral specie per event. The electron is assumed to lose 9 eV (the threshold energy for the reaction). Dissociation to two

neutrals is the dominant H_2-electron inelastic interaction, other than line radiation.

$$H_2 + e \rightarrow H_2^+ + 2e$$

Molecular ionization is assumed to leave the hydrogen molecule energy unchanged (transferring it to the H_2^+ species). The electron loses 18.3 eV (the H^0 ionization energy plus H_2 binding energy), with a cold ($T = 0$) electron being added to the electron density.

$$H_2 + e \rightarrow H^+ + H^0 + 2e$$

Ionizing dissociation is treated like a Franck-Condon process ($H_2 + e \rightarrow 2H^0 + 2e$) plus ionization. Thus the H^+ and the H^0 each carry away half the H_2 energy plus 3.5 eV, and the electron loses 18.3 eV (ionization plus binding energy). The new electron is assumed cold ($T = 0$).

$$H_2^+ + e \rightarrow 2H^0$$

Dissociative recombination uses the entire electron thermal energy. The hydrogen atoms carry the H_2^+ energy, but the dissociation energy and any radiation is ignored. Essentially, internal energy is ignored and only the thermal energy of the initial particles is transferred to the product.

$$H_2^+ + e \rightarrow H^0 + H^+ + e$$

Dissociation of ionized molecular hydrogen is treated like H_2^+ dissociative recombination. The thermal energy of the molecule is split between the resulting proton and hydrogen atom. Like all other molecular species rate coefficients, the molecule is assumed to be in the ground vibrational state.

$$H_2 + H_2^+ \rightarrow H_3^+ + H^0$$

This is the only source for H_3^+. As with all processes involving similar mass incident particles, an effective root-mean-square temperature is used to calculate the cross section. The energy of the incident particles is arbitrarily split by mass among the products. Internal energy is, again, ignored.

$$H_3^+ + e \rightarrow 3H^0$$

This is the only process removing H_3^+. It is about two orders of magnitude stronger than the source term for H_3^+. The difference in rates is further enhanced by the fact that the destruction of H_3^+ occurs via electrons whereas creation requires H_2 or H_2^+. Appreciable amounts (1%) of H_3^+ would only be found in partially ionized (50%) molecular hydrogen.

It was found that H_3^+ densities were so low that removal of

those terms had no effect on the code results. The code cannot permit a density to fall to zero as this causes overflow problems, so densities are clamped at 1 cm^{-3}. For H_3^+ the equilibrium density is far below this, resulting in large rate coefficients for H_3^+ dissociation. This often limited the integration step size, thus motivating the removal of H_3^+ creation and dissociation processes from the code.

$$H_2 + H_2^+ \rightarrow H_2^+ + H_2$$

Molecular hydrogen charge exchange is treated like atomic charge exchange. The particles exchange energy.

Neutral Transport

The extreme spatial asymmetries in the neutral density require a variety of concessions be made to the geometry of the experiment. The large rate coefficient for atomic hydrogen charge exchange also modifies the treatment of the transport for this species. The treatment of spatial dependencies in hydrogenic species was an addition to the original 'pure' zero-D code, and greatly improved the code's results.

Three classes of neutrals are considered by the code. Atomic Hydrogen, molecular Hydrogen and impurities. The machine is divided into four regions: The central and bridge plasma regions, and central and bridge edge regions. Table 2 summarizes the geometric factors used to describe the regions and Figure 7 shows the location of the regions

in the machine. Note that only the hydrogenic neutral species are split into regions. Particle transport along field lines insures that charged specie behave uniformly across the neutral regions. (See the section on ICRF heating for a discussion of ion temperature anisotropies and their treatment.)

Impurity neutrals are left totally zero-D. Transport of these particles is handled with a simple kinematic model

$$\frac{dn_n}{dt} = -n_n \frac{d}{v}$$

where:

n_n = impurity neutral density

d = scale length (see Table 2)

v = $\sqrt{\frac{2T}{M}}$, thermal velocity

The scale length is the volume weighted average of the central and bridge region lengths.

The edge regions are the regions that desorbed (not reflected) hydrogenic species drift through to get from the wall to the plasma (but not *vice versa*). Addition of these regions to the code affected only the first 10 microseconds of the neutral hydrogenic densities. The edge regions were left in the code because the several microsecond averaging of desorbed neutral H_2 flux into the plasma helps stabilize the integration of a very stiff term. The addition of this otherwise irrelevant but physically reasonable process halves the computer time

required.

All the desorbed hydrogenic neutrals are put into their corresponding edge region (four additional 'species'). Particles are moved to the plasma regions at the rate

$$\frac{dn_p}{dt} = n_e \frac{d}{v}$$

where:

n_p = Plasma region neutral density

n_e = Edge region neutral density

d = width of the edge region (see Table 2)

v = thermal velocity of desorbed particles at 0.025 eV.

Molecular hydrogen in the plasma is treated in a manner similar to impurity neutrals but in two regions. All interactions between H_2 and other species are treated for each region separately. Thus the two regions require completely separate treatment as two separate species. Interactions between a regional species and a global (a true zero-D) species are calculated for each region and summed, weighted by the volumes of the regions.

The rate H_2 leaves a region is

$$\frac{dn_{H_2}}{dt} = -n_{H_2} \frac{d}{v}$$

where:

n_{H_2} = H_2 neutral density for the region

d = neutral scale length for the region

v = $\sqrt{\frac{2T_{H_2}}{m}}$ = thermal velocity.

A fraction of the particles leaving one plasma region is transferred to the other region. This fraction is calculated from the geometry of the regions. The rest of the particles are sent to the wall. (The edge regions are not used for particles leaving plasma regions as their velocities are much greater than desorbed neutral velocities.)

Atomic hydrogen is treated identically to molecular hydrogen except that particle transport in the central transport region is modified to account for charge exchange. The charge exchange mean free path is typically 30 cm. The atomic hydrogen transport in the bridge region, which has a scale length of 7 cm, is not substantially modified by charge exchange.

The multiple charge exchange neutral transport problem can be quite challenging. Several approximations reduce the problem to computationally tractable levels. First, neutrals entering the region rapidly approach the ion temperature by elastic neutron-ion collisions and charge exchange. Spatially uniform ion temperatures (implicit in a zero-D treatment) are also assumed. Thus treatment of atomic hydrogen neutral transport may be treated assuming spatially constant velocities. In such a case, where the plasma dimensions are much larger than the charge exchange mean free path, we may treat the problem in fluid terms and assume Ficks law diffusion.

$$\frac{\partial n_n}{\partial t} - D\nabla^2 n_n = \text{source}$$

where n_n is the neutral density, and D is taken as

$$D = \frac{(\Delta X)^2}{\tau}$$

where ΔX = step size and τ = time per step.

In effect a charge exchange event is considered a collision which simply alters the direction of the neutral. Thus the identity of the neutral is tied to the electron. (Remember the neutral and ion temperatures are typically within 10% of each other.) With this view, transport reduces to a simple random walk with a step size of the charge exchange mean free path.

Given the factor of 2 accuracy of many of the rate coefficients, it would be pointless to attempt a detailed solution to atomic hydrogen transport. All that is desired is reasonable scaling with ion density and rough quantitative accuracy. These goals can be met with a solution to the fluid transport equation in one dimension and simple estimates of D.

Wall Desorption

McCracken and Stott[15] published an outstanding review of plasma-surface interactions. Data for desorption is taken from this article. The hydrogenic flux to the wall is summed for neutral and charged particle transport. The desorption yield is dependent on the

energy of the flux to the wall, the cross section for desorption and the fraction of the surface covered by a particular impurity.

The energy dependence of the ion induced wall desorption has a low energy threshold dependent on the surface binding energy. For ungettered machines, with little surface conditioning, this energy is small, a few eV.[16] Clean surfaces have thresholds of a few tens of eV. The yield rises with energy until the burial of particles starts competing with desorption. The yield levels off at this energy (typically 1 to 50 KeV).

Typical yields are 1-10 particles/particle for dirty surfaces and 0.1 particles/particle for tightly bound 'clean' surface layers. A yield linear in energy normalized to 1 at 500 eV and averaged over a Maxwellian is used.

The parameter η_0, the normalized (to T_i = 333 eV) yield, is a free parameter for each neutral specie. Included in η_0 are the cross section and coverage. This may be thought of as the fraction of the machine surface area covered by a particular specie times the yield at 500 eV (monoenergetic).

The energy dependence of desorption yield is calculated by a separate program. ZD interpolates into the table produced to get the normalized yield for the temperature of the incident particles. The calculation of yield performs the averaging over a Maxwellian velocity distribution by brute force numeric integration. Figure 8 shows the H_2

normalized desorption yield energy dependence. A sheath potential of $3T_e$ is assumed to accelerate ions into the wall.

All desorbed particles are assumed neutral. The magnetic field will return charged particles to the wall. Only hydrogen (charged or neutral) is assumed to induce desorption. The energy of the desorbed particles is assumed to be the wall temperature, 0.025 eV. Only one parameter per desorbed specie is needed. This parameter specifies the yield at 500 eV. Note that we may also include in this parameter a factor describing the fraction of the surface covered by that species. One normally thinks of the coverage on atomic scales as the fraction of a monolayer the species occupies. This factor can, in fact, be used to specify a macroscopic coverage as well (e.g., the fraction of non-gettered wall surface area).

In fact, the entire average character of the surface is described via a single energy dependence and a coverage factor of the desorption yield. The details of spatial dependence of wall gas load, particle flux, titanium gettering, as well as the impurity induced desorption, impact angle, electron and photon induced desorption are ignored. The data to describe these effects are not available and the precision of the rest of the code is insufficient to make use of such data.

With the addition of multiple regions for neutral hydrogen species, the problem of spatially dependent wall condition may be addressed. The octupole was run with 6 titanium sublimators in opera-

tion. The central region is almost completely covered by titanium. For this reason, desorption is assumed to occur only in the bridge region. Less than 50% of the wall area in the bridge region is gettered.[17]

Multiple regions also give one the choice of where to put ion induced desorption neutrals, (*i.e.*, to specify the region the limiters are in). ZD uses central region ion induced desorption. This was done to increase the fueling efficiency at low RF powers. The basic plasma parameters are quite insensitive to the region chosen for ion induced desorption except at low RF powers. Otherwise, slight changes in the coverage accomodate the resulting differences in fueling efficiency. The subject of limiter location will be more thoroughly addressed in Chapter 6.

Typical desorption yields are measured to be 4-10 at incident energies of 100 eV.[15] ZD results match the experimental results with an H_2 cover factor in the vicinity 2. Given a factor of 5 for the higher energy normalization and $\frac{1}{2}$ for the partially gettered wall, an equivalent yield at 100 eV used by the code is 5. The implications of this result will be discussed in later chapters. Of interest here is the fact that a simple physical model for desorption produces results consistent with detailed studies of particle induced desorption.

Wall Reflection

About half the particles incident on the wall are simply reflected.

The incident particle may not be backscattered until it gets fairly deep (many atom layers) into the wall material. The probability that a backscattered particle will reemerge from the wall is dependent on the depth that such scattering occurs. Thus there is a substantial energy dependence to the reflection coefficient.

As for desorption, ZD gets particle reflection coefficients by interpolating into a table produced by another program. This program uses a fit to data from Heiland[17] to calculate the reflection probability as a function of incident energy, mass, charge, and wall material. The reflection probability is then averaged over a Maxwellian energy distribution. The calculation is simplified by a few reasonable assumptions.

First, the reflection coefficient has a universal form if it is stated in terms of the reduced energy of the incident particle.[15] For titanium

$$\epsilon = \frac{70.76 E_i}{(47.9 + \mu_i) Z_i \sqrt{7.851 + Z_i^{\frac{2}{3}}}}$$

where

ϵ = reduced energy

E_i = incident energy

Z_i = incident nuclear charge

μ_i = incident mass in proton units.

The wall material is assumed to be titanium as about 90% of the wall surface is gettered. Thus only a few constants are needed to

specify the different reflection probabilities of the incident species. The reflection coefficient varies slowly with energy and in past studies was taken as constant ($R_p = 0.5$). The only case where this is insufficient is for late times of gun only shots.

For these low temperature ($T_i < 5$ eV) non-heated plasmas reflection of diffusing plasma ions dominates the neutral source. ZD results are sensitive to several percent changes of the reflection coefficient in these cases. Unfortunately data at low energies is sparse, until one reaches room temperature. At 0.025 eV, sticking coefficients are published for most molecular gasses on titanium.[19] The simple expedient of limiting the reflection coefficient to a maximum of one minus the sticking coefficient at room temperature was taken.

A final note about low energy reflection coefficients is that they should not be taken too seriously. At first glance it would seem that this case makes an ideal measure of low energy reflection coefficients. (Low energy neutrals are extremely difficult to detect, but here a large number of reflected particles are returned to the plasma to radiate.) Unfortunately the approximations used to calculate excitation rate coefficients (and most other terms) reduce the accuracy of such a technique to about 10%. The atomic rate coefficients accuracies exceed a factor of 2 below 3 eV. The adjustments made to the particle reflection coefficients seem to be correcting for the errors in the hydrogen rate coefficients.

ICRH Input Power

ICRH is a valuable tool in the study of confinement in that it allows a broader range of plasma parameters to be studied. It introduces a number of problems as well. The local nature of the input power is the primary difficulty. Other disturbing characteristics of ICRH are: 1) a two component ion distribution function; 2) ion distribution function velocity anisotropies (3:1 $\perp$:$\parallel$ temperatures); 3) toroidal asymmetries; 4) finite Larmor radius effects; and 5) complex coupling mechanism.

The utility of ICRH, and in particular the ability to independently control power input and to promptly terminate heating, motivate its inclusion in this study. A compromise is taken. An empirical treatment of the ICRH input power is included in ZD with the obvious *caveat* that the code's accuracy, particularly for ions, is degraded.

The simplest approach to ICRH input power is to add the power to a single hydrogen ion species. Coulomb collisions then couple the energy to the other species. The ion-electron coupling and charge exchange are the dominant hot ion loss mechanisms. The hot ion temperature is remarkably insensitive to plasma parameters experimentally. The hot ion temperature is 250-300 eV over factors of 2 change in poloidal field, factors of 4 in ICRH power, factors of 10 in electron density and factors of 5 in T_e.[20]

The power coupled to the plasma as a function of density is taken from Fortgang's thesis.[21] No ion temperature or spatial dependencies are included. A linear fit to the data yields the form

$$\frac{dE}{dt} = P_{in}(5.26 \times 10^{-15} n_i + 9.46 \times 10^{-2}) \frac{\text{watts}}{\text{cm}^3}$$

where:

E = energy density

n_i = ion density

P_{in} = power input (see discussion below)

The input power, P_{in}, specifies the power level of the ICRH oscillator for the shot to be simulated. This parameter is dimensionless, being normalized to 1 megawatt total (volume integrated) at an ion density of 2×10^{13} cm^{-3}. Note that this is the power coupled to the plasma, not the oscillator input power.

Chapter 3 covered the measured ion temperature anisotropies. On the basis of that data, the hot ion component is seen to be localized to the plasmas edge. Several features were added to ZD to account for this anisotropy. An edge temperature is defined as a perpendicular component of the hot ion temperature measured by the charge exchange analyzer and a parallel component of the bulk ions. The charge exchange hot ion temperature is calculated from a fit to experimental data while the bulk ion temperature is calculated normally. Thus

$$T_{edge}eV = \frac{2}{3}170(1 - e^{-P_{in}/.05435}) + \frac{1}{3}T_i.$$

The perpendicular component of T_{edge} and the charge exchange data are shown in Figure 9.

Note that the edge ions are not treated as a separate species. The edge temperature is used only to set two wall desorption values. First, T_{edge} is taken as the energy of ions impacting the limiter. Second, a small fraction of charge exchange events are assumed to occur in the edge which increases the temperature of neutral atomic hydrogen impacting the wall.

Limitations

In this section the assumptions, limitations, and accuracies of the model are brought together in one place. The objective is to ascertain the overall accuracy expected of the code and to examine some of the experimental problems which bear on the accuracy of the conclusions drawn from the model. Table 3 lists assumptions for which there are reasonably obvious smallness parameters. Table 4 has a longer list of problems, many of which are less easily quantifiable.

Reviewing Table 3, the only substantial errors are seen to relate directly to ICRH plasmas. In particular, the non-Maxwellian ion distribution function grossly violates the assumption of Maxwellian distributions.

As mentioned previously, some empirical 'fixes' are used to alleviate this problem. Errors in the ion distribution function have

little effect on charge exchange rates as the rate coefficient is roughly independent of energy to about 10 KeV. The ion temperature the code uses will adjust to couple the appropriate power to the various species. Electron-ion collision frequency is only weakly dependent on T_i ($\sim 1\%$ variation for $0 < T_i < 300$ eV for $T_e = 30$ eV).

Ion-ion coupling will be strongly affected. The impurity temperatures will be high by about a factor of 2 during ICRH (assuming $T_\perp = 250$ eV, $T_\parallel = 70$e V). This is of little consequence however as the impurity ion temperature does not enter into the wall reflux, or impurity radiation terms. It only weakly affects the coupling to the electrons (via the ion $\rightarrow$ impurity $\rightarrow$ electron path).

Finally, the ion anisotropies are empirically included in calculating desorption. It should be reiterated that the hot edge is assumed to be part of the average ion temperature calculated by the code. Thus the hot ion component is not treated as a separate species.

Most of the items in Table 4 have been discussed in the sections describing terms in the code. Charge exchange on impurities was not mentioned as it is totally ignored by ZD. Data for charge exchange cross sections are largely unavailable. Recently the importance of this topic has been recognized.[22,23] Charge exchange is an alternative recombination path which lowers the charge state of impurities. This can substantially increase radiated power. An estimate of the neutral density required to effect a significant change in this charge state distribution is

easily derived. Assume for this purpose that dielectronic recombination proceeds at a rate equal to that of radiative recombination. Then

$$\mathcal{R}_{recomb} = n_e n_z \, 2 \times \{5.2 \times 10^{-14} Z \sqrt{\tilde{E}} [0.43 + \frac{1}{2} \ln \tilde{E} + 0.48 \tilde{E}^{-\frac{1}{3}}]\} \mathrm{cm}^{-3} \mathrm{sec}^{-1}$$

$$\tilde{E} = \frac{E_{ioniz}}{T_e}$$

Z = ion charge (not nuclear charge!)

n_e = electron density,

n_z = impurity charge state z density

The primary concern is that charge exchange will increase the radiated power by increasing the density of easily excited ions. This dictates the choice of $\tilde{E} \sim$ 3 and $z \sim$ 5. (For example, O^{+5} at $T_e \sim$ 10 eV has $E_{ioniz} \sim$ 114. eV. This is an ion which will have a substantial function of the total oxygen population). Then

$$\mathcal{R}_{rec} = n_e n_z \times 1.17 \times 10^{-12}.$$

This is compared to the charge exchange rate. Using data from Olson and Salop,[23] and Hulse *et al.*,[22] the charge exchange cross section is estimated as 5×10^{-15} cm^2 and roughly independent of energy. Taking the neutral thermal velocity to estimate $\langle \sigma v \rangle$ yields

$$\mathcal{R}_{cx} = n_n n_z 5 \times 10^{-15} \{9.79 \times 10^5 \sqrt{T_n}\} \mathrm{cm}^{-3} \mathrm{sec}^{-1}$$

where:

n_n = neutral density

T_n = neutral temperature eV

Taking $T_n = 30$ eV

$$\mathcal{R}_{cx} = n_n n_z \times 2.68 \times 10^{-8} \mathrm{cm}^{-3} \mathrm{sec}^{-1}$$

Equating these rates gives the n_n/n_e ratio for charge exchange to be as fast as recombination

$$\frac{n_n}{n_e} = 4.38 \times 10^{-5}$$

The effects of this level of charge exchange depend on $d\langle z \rangle / dT_e$. ($\langle z \rangle$ = average charge state of ions for a nuclear species.) See Post *et al.*[22] for a qualitative review of the effects of doubling the recombination rates. The radiated power can easily double for a fixed T_e. This implies such charge exchange will lower T_e. This in turn reduces $\langle z \rangle$ hence reduces the charge exchange rate (a strong function of z at low z) and increases ion-electron coupling.

Charge exchange cross sections for low z ions are uncertain by orders of magnitude. Few measurements have been made. ZD ignores this process. Given such uncertainty in the cross sections the only statement of error which can be made is that for $z \geq$ 5 and $n_n/n_e \geq 10^{-4}$ substantial (factor of two) errors can be incurred for ranges of T_e where $d\langle z \rangle / dT_e$ is large.

The zero-D nature of the code and some of the implications of this have been previously discussed. Experimental measurements are

local, however. T_e is measured at a point. Spectral lines and n_e are line integrated measurements. The various diagnostics are scattered around the experiment. Toroidal asymmetry of T_e by 10% could induce factor of two errors in impurity line intensity. Ion temperature asymmetries are far less important for impurity diagnostics but linearly affect reflux and charge exchange. By using multiply ionized impurity lines, the spatial distributions of impurities are given time to smooth out.

Experimentally, multiply ionized species are not seriously asymmetric. Reasonable electron temperatures are obtained with CIII light by the line ratio technique. This method is very sensitive to the line ratio (exponentially). The two lines were measured toroidally separated by 120°. While this only indicates that any asymmetry is time invariant, it is a strong argument for a symmetrical distribution. The method correlates within 20% of probe electron temperatures throughout the ICRF pulse and well after heating ends.

Finally, it should be noted again that ZD gives impurity densities, not line intensities. The excitation functions used are a standard form whose relative accuracy is less than other uncertainties. All intensity measurements are relative.

To summarize, the accuracy of conclusions based on ZD are primarily limited by a few inherent restrictions on the code. First is the zero D nature of the model. Second the accuracy of the rate coefficients is a factor of two overall. The rate coefficients are most

accurate in the regime being studied; moderate T_e and low z. Charge exchange on impurities may become the factor limiting accuracy when $\langle z \rangle$ for an impurity exceeds 5 (about 100 eV for carbon, 30 eV for oxygen, aluminum and titanium). A few independent tests of the code are lost by the use of uncalibrated line intensities. ICRH induced ion velocity space anisotropies cause substantial errors in impurity ion temperatures but otherwise are benign. Spatial anisotropies are potentially more serious but evidence indicates that multiply charged impurities are homogeneous. Overall, ZD is expected to be accurate to within a factor of 2 for non-ICRH plasmas. With caveats regarding spatial inhomogeneity and impurity ion temperatures ICRH plasmas will suffer only slight degradation in accuracy (to perhaps a factor of 3). Corrections will have to be applied to T_i to account for spatial and velocity anisotropies.

References for Chapter 4

[1]R.J. Hawryluk and J.A. Schmidt, *Nucl. Fusion* 16, 775(1976).

[2]R. Hulse, private communication.

[3]R.W.P. McWhirter in Plasma Diagnostic Techniques, R.H. Huddlestone and S.L. Leonard (eds.) (Academic Press, New York, 1965).

[4]F.S. Acton, Numeric Methods That Work (Harper & Row, New York) 1970).

[5]D.L. Brook, NRL Plasma Formulary (Naval Research Laboratory, 1980).

[6]D.E. Post and R. Hulse, EQLCDC code, private communication.

[7]D.E. Post, R.V. Jensen, C.B. Tarter, W.H. Grasberger and W.A. Lokke, *Atom Data and Nucl. Data Tables* **20**, 397(1977).

[8]G. Bekefi, Radiation Processes in Plasmas, (John Wiley and Sons, New York, 1966).

[9]C.W. Allen, Astrophysical Quantities (Oxford University Press, New York) 1955.

[10]A. Burgess, *Astrophys. J.* 141, 1588 (1965).

[11]A.L. Merts, R.D. Cowan, and N.H. Magee, Jr., LASL Report LA-6220-MS, Los Alamos, NM (1976).

[12]E.L. Freeman and E.M. Jones, Culham Laboratory Report CLM-R137 (1974).

[13]E.M. Jones, Culham Laboratory Report CLM-R175 (1977).

[14]C.F. Barnett *et al.*, Atomic Data for Controlled Fusion Research, ORNL-5206 and ORNL-5207 (1977).

[15]G.M. McCracken, and P.E. Stott, *Nucl. Fusion* **19**, 889(1979).

[16]D.J. Rose and M. Clark, Plasmas and Controlled Fusion (MIT Press, Cambridge, MA) (1961).

[17]H.R. Garner, University of Wisconsin PLP-834 (1980).

[18]W. Heiland, *J. Vac. Sci. Technol.* **14**, 576(1977).

[19]D.J. Harra, *J. Vac. Sci. Technol.* **13**, 471(1976).

[20]E.J. Strait, private communication.

[21]C.M. Fortgang, Ph.D. Thesis, University of Wisconsin (1983).

[22]D.E. Post, Princeton Plasma Physics Laboratory PPPL-1877

(1982).

[23]R.A. Hulse, D.E. Post, and D.R. Mikkelsen, *J. PHys. B* **13**, 3895(1980).

[24]R.E. Olson and A. Salop, *Phys. Rev. A* **14**, 579(1976).

Figure 1: Early measurement of separatrix electron temperature versus ICRH input power.

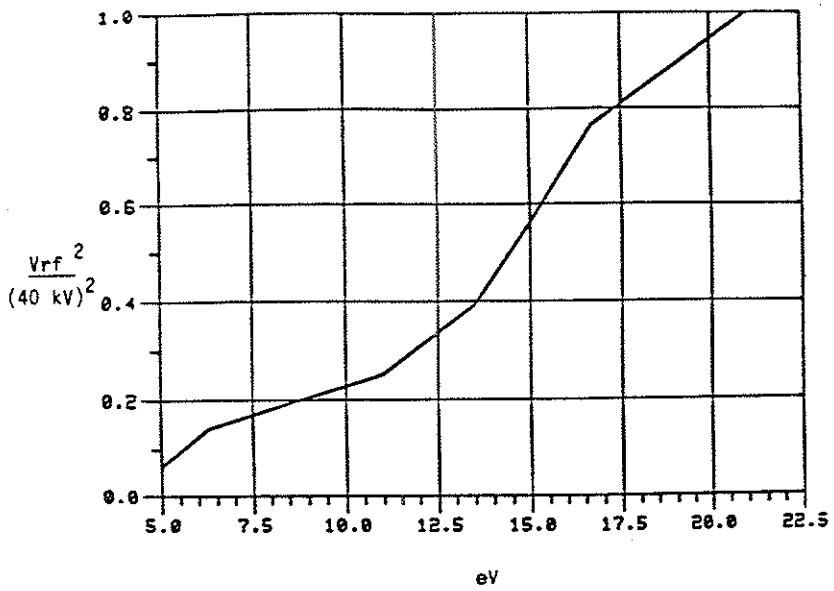

Figure 2: Coronal equilibrium zero-D calculation of electron temperature versus input power.

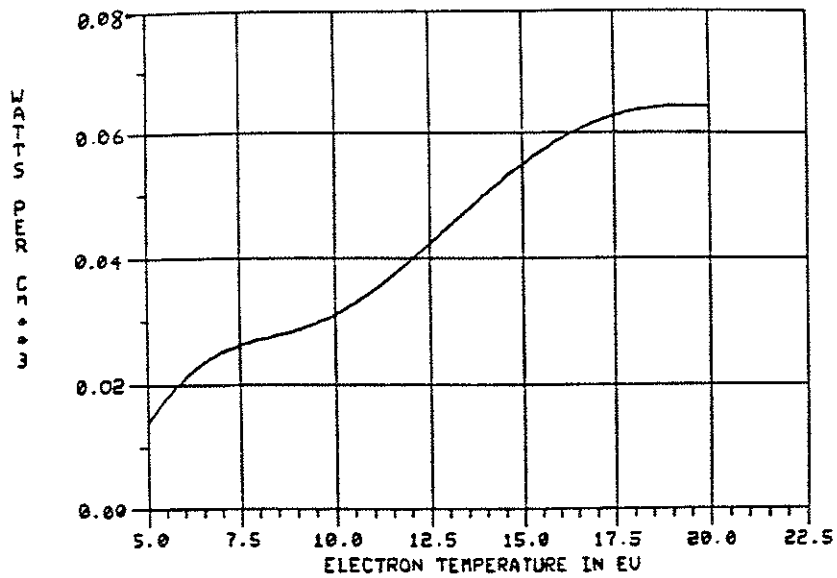

Figure 3: Measured total radiated power versus N_2 doping level.

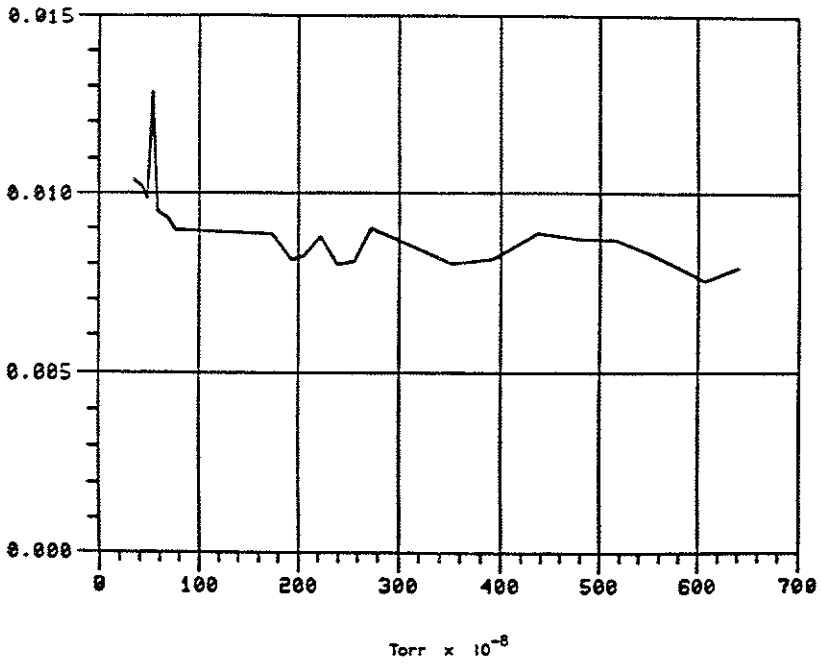

Figure 4: NIII line radiation measured with an interference filtered PMT versus N_2 doping level.

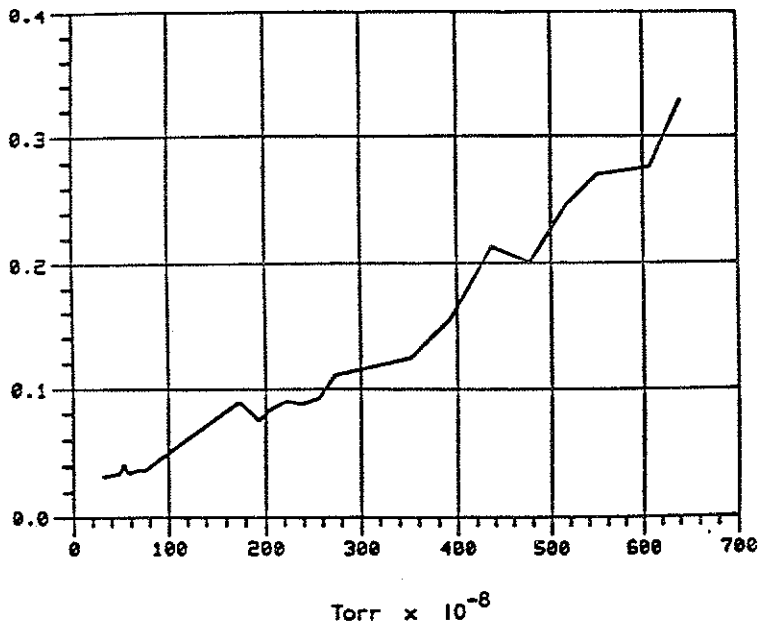

Figure 5: The power radiated from a 30 eV plasma with an initially neutral carbon impurity. The electron temperature and density are held constant and all other radiative and transport processes were removed from the code.

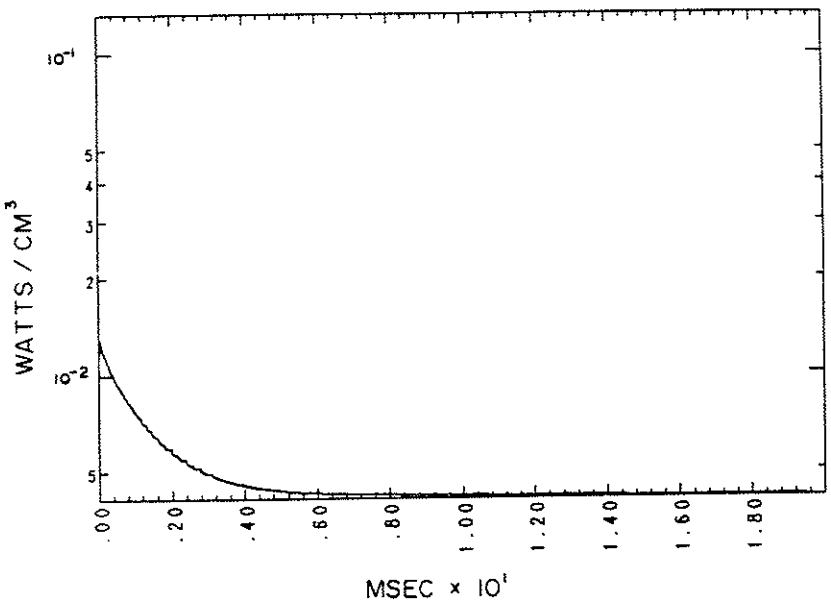

Figure 6: The density evolution of C^{+5} for a 30 eV plasma with an initially neutral carbon impurity. The electron temperature and density are held constant and all transport processes were removed from the code.

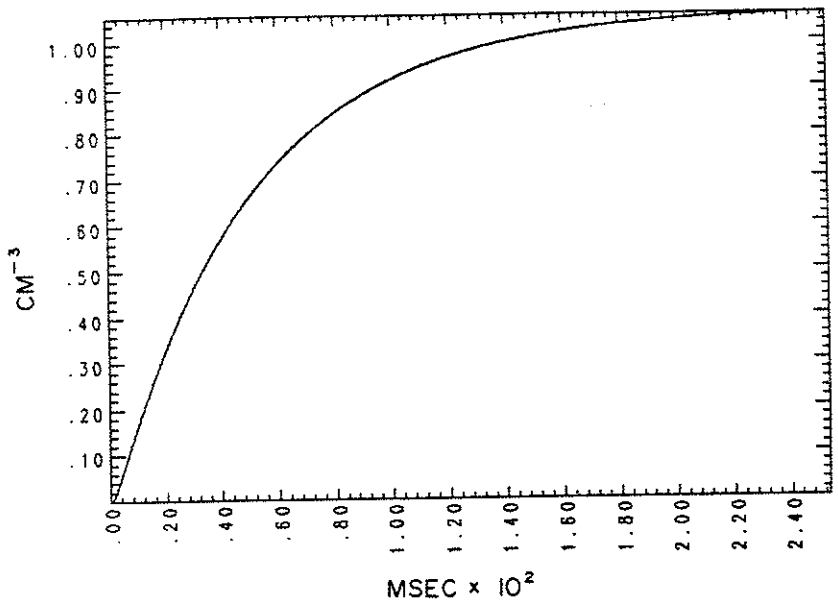

Figure 7: Geometry of the regions used by ZD for hydrogenic neutrals. The poloidal cross section is vertically and horizontally symmetric.

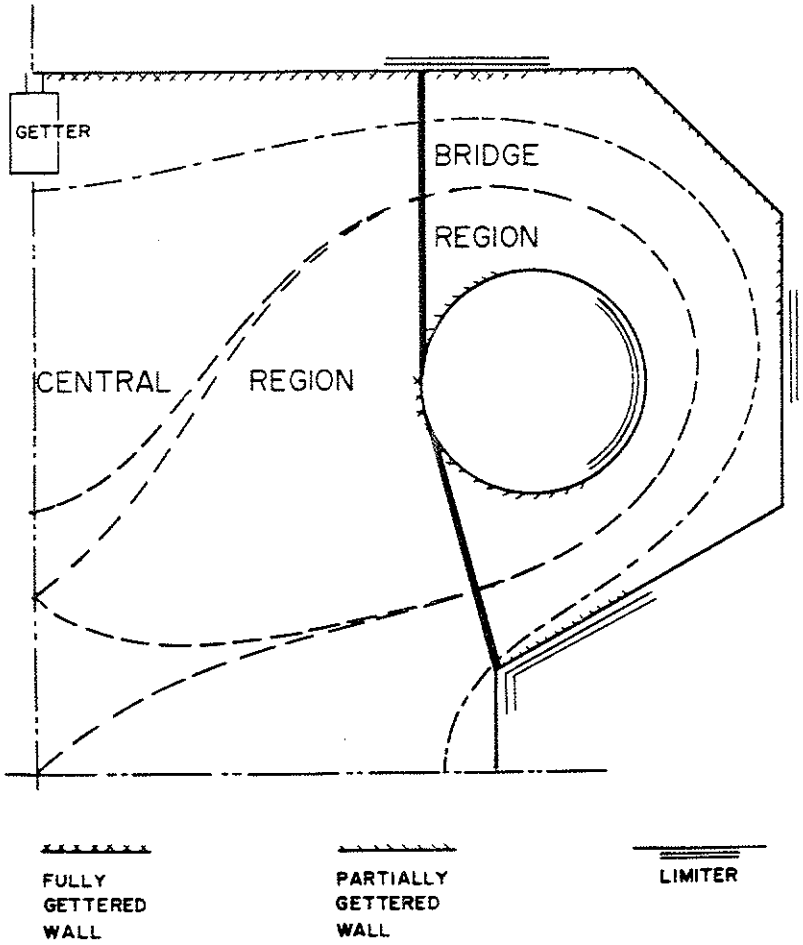

Figure 8: Molecular hydrogen desorption yield versus temperature of incident particles. This plot shows the yield for protons or neutral atomic hydrogen atoms. A Maxwellian velocity incident distribution is assumed.

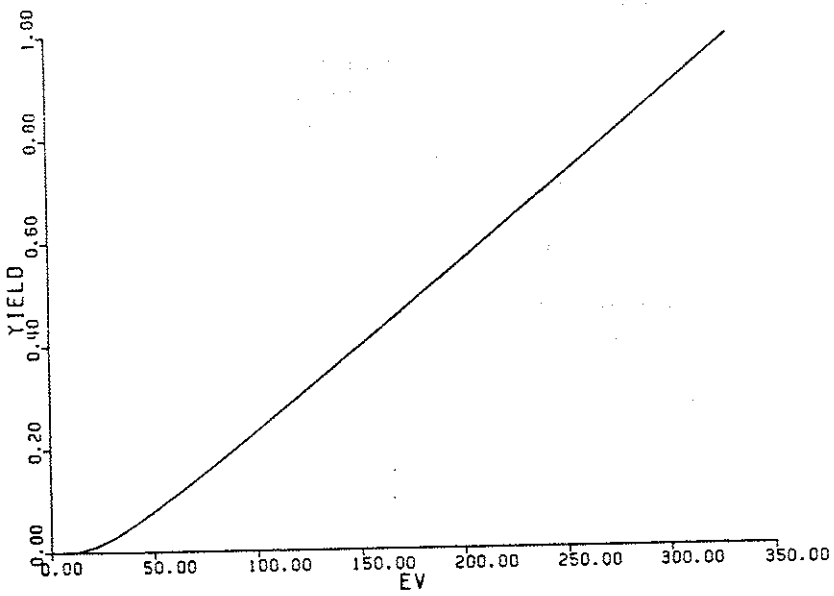

Figure 9: The hot ion temperature measured by the charge exchange analyzer and the fit used by ZD.

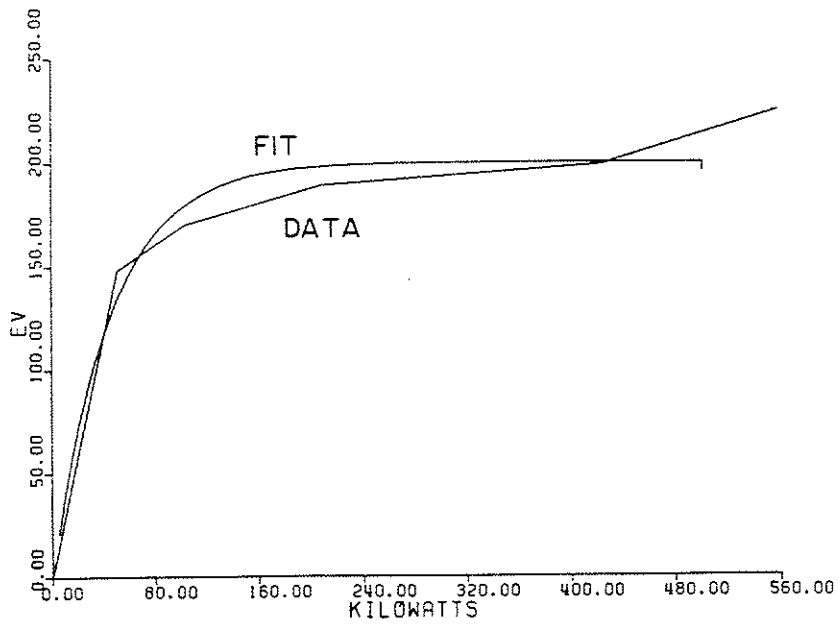

Table 1

ZD processes

1) elastic $e^- \Rightarrow x_i$ electron-ion
2) elastic $x_i \Rightarrow x_j$ ion-ion
3) elastic e^-, $X_i \Rightarrow N_j$ electron ion-neutral
4) inelastic electron-impurity interactions
   a) bremßtrahlung
   b) recombination $e^- + X_i^n \Rightarrow X_i^{n-1}$
      1) radiative
      2) dielectronic $e^- + X_i^n \Rightarrow X_i^{n-1}$ +photon(s)
      3) 3 body $2e^- + X_i^n \Rightarrow X_i^{n-1} + e^-$
   c) ionization $e^- + X_i^n \Rightarrow 2e^- + X_i^{n+1}$
   d) collisional excitation $e^- + X_i^n \Rightarrow e^- + X_i^{n*} \Rightarrow e^- + X_i^n$ +photon(s)
5) Special cases

a)	$H^+ + H \Rightarrow H + H^+$	charge exchange
b)	$H^+ + H_2 \Rightarrow H + H_2^+$	charge exchange on H_2
c)	$H_2 + e \Rightarrow 2H + e$	dissociative excitation
d)	$H_2 + e \Rightarrow H_2^+ + 2e$	electron ionization of H_2
e)	$H_2 + e \Rightarrow H^+ + H + 2e$	dissociative ionization
f)	$H_2^+ + e \Rightarrow 2H$	dissociative recombination
g)	$H_2^+ + e \Rightarrow 2H^+ + 2e$	dissociative ionization
j)	$H_2^+ + e \rightarrow H^+ + H + e$	dissociative excitation
k)	$H_2 + H_2^+ \Rightarrow H_2^+ + H_2$	molecular charge exchange

6) neutral transport
7) ion transport
8) wall desorption
9) wall reflection
10) ICRH input power

Table 2
Geometric Factors used in ZD

	Bridge region	Central region
Neutral scale length (cm)	8.0	60.0
Area to volume ratio (cm^{-1})	0.54	0.057
Fraction of surface area facing opposite region	0.14	0.22
Desorbed neutral drift distance (cm)	3	10
Fraction of total volume	0.1	0.9
Total wall area	4.0×10^5 cm^2	
Limiter area	2.0×10^4 cm^2	
Total MHD stable volume	7.6×10^6 cm^3	
Equivalent-volume at separatrix density	5.0×10^6 cm^3	

Table 3
Basic Plasma Conditions

	Assumption	Condition	How well met
1)	Collisionality	$\omega_{ci}/\nu_i >> 1$	$\omega_{ci}/\nu_i > 100$
2)	Finite gyro radius	$\rho_i < (1/n\, dn/dr)^{-1} = L$	Bulk ions $\rho_i \sim .1L$ ICRH tail $\rho_i \gtrsim .3L$ (at 1 keV)
3)	Stability	Avg Min B stability within ψ_{crit}	Absolutely
4)	β	$\beta = (B^2)/(\sum_i n_i k T_i) << 1$	$\beta \sim 10^{-5}$
5)	Maxwellian distributions	$M = P_{NC}/\frac{nkT}{\tau} << 1$ P_{NC}=non-collisional power τ=equilibration time	ICRH ions $M \sim 1$ electrons $M \sim 0$ Neutrals $M \sim 0.25$
6)	Optically thin plasma	$\tau = 5.4 \times 10^{-9} \lambda (\mu/T)^{\frac{1}{2}} n_i l << 1$	$\tau \sim 10^{-3}$
7)	Coulomb logarithm for collisionality	$1/\Lambda << 1$	$1/\Lambda \sim 0.08$

Table 4
Other Limitations

1) Zero-D Bulk of plasma is homogeneous experimentally except for neutrals.

2) Code gives only impurity density, not line intensity.

3) Empirical treatment of ICRF input power.

4) Impurity rate coefficient accuracy is factor of 2.

5) Diffusion of particles is calculated for zero-D with constant scale length ignoring modifications to the density profile.

6) Particle reflection from walls is treated simply.

7) Impurity induced reflux is ignored.

8) Radiation from minor sources (ionization to excited state, 3 body recombination, etc.) is ignored.

9) Impurity rate coefficient accuracy degrades at low T_e.

10) Dielectronic recombination model is accurate to within a factor of 2 only for Z $<$ 20.

11) Initial impurities are neutral (gun injected impurities are 'frozen').

12) Only neutrals are emitted from the wall.

13) Coronal model is assumed (metastable states are collisionally de-excited).

14) Charge exchange on impurities is ignorable.

$$(n_{neutral}/n_e < 10^{-4})$$

15) Turbulent injection phase of a shot (the first few hundred microseconds) is ignored.

CHAPTER 5

GUN AFTERGLOW PLASMAS

Overview

Gun afterglow plasmas (i.e., no ICRH power) are the simplest to model. With T_e above 3 eV the modeling is quite successful, and provides a wealth of information about the plasma-wall interaction. Below 3 eV, the hydrogen rate coefficient's accuracy degrades, causing increased differences between experimental data and code results.

The gun plasmas initially have electron temperatures of 30 eV decaying to 2 eV by 12 milliseconds (Figure 1). The density starts at 1×10^{13} cm^3 and decays to 2×10^{12} (Figure 2). This range of plasma parameters spans several important energy thresholds for the plasma-wall interaction, forcing the choice of desorption threshold and the form of the particle reflection coefficient energy dependence in ZD. Once these parameters are set, the desorption yields used are constrained by the electron temperature decay. With the temperature correct, the rest of the data produced by ZD closely matches the experimental data.

The ability to unambiguously set single parameters is due to the wide range of T_e spanned by the plasma. This feature is lost when RF is applied. The initial character of the surface is presumed independent of RF however, so the energy thresholds are not modified

by RF heating.

The data show four distinct intervals of unique behavior. The first half millisecond shows a rapid drop in density, and large variations in H^0 density. This interval is presumed to be dominated by the relaxation of injection turbulence. No attempt is made to treat this interval.

From 1/2 to 2 milliseconds, the plasma temperature drops rapidly from 30 eV. Particle induced desorption produces H_2 and impurities. Line radiation and charge exchange are the dominant energy loss mechanisms. At the end of this interval temperatures have cooled so that the desorption rate is rapidly dropping. The H_2 density begins to drop as losses exceed the source rate.

From 2 to 6 milliseconds the electron temperature slowly drops by a few eV. T_e is well below most line radiation excitation energies. The ion temperature is slightly higher than T_e which transfers energy to the electrons to compensate for the small losses. As the plasma cools, the particle reflection coefficient rises. At the end of this interval, elastic ion neutral collisions (neutrals being produced by reflection of ions from the limiter) are causing a larger ion cooling rate than coulomb collisions with electrons.

After 6 milliseconds particle reflection continues to increase. This generates a larger source of H^0, and increases the number of 'bounces' from walls a neutral survives through. Thus, the lifetime

of H^0 increases as well. The increasing H^0 density cools the ions (via elastic scattering) faster than coulomb collisions, and at 10 msec, the ion temperature falls below the electron temperature.

While the accuracy of the code degrades at low temperatures the successive, isolated dominance of the different processes permits unambiguous assignments of the processes responsible for the plasma's behavior. By returning to the experimental data with this understanding, the thresholds may be accurately determined. Also, indications of the nature of corrections which would be required in the simulation to provide a better match with the experimental data help in interpreting the far more complex RF cases.

Hydrogen

Significant sources of atomic hydrogen are H_2 dissociation, reflection of ions from the wall as neutrals, and recombination. The primary losses are ionization and neutral transport. The first half of the shot clearly shows H_2 desorption producing molecular hydrogen which dissociates making H^0. This H^0 is then ionized fueling the plasma.

Figure 3 shows a plot of experimental data overlaying H_2 and H^0 densities. Figure 4 shows the code results. The code shows a faster rise of H_2 density and a prompt fueling rate (seen as a reduced dn/dt early in time). Data clearly indicate the initial H_2 density, H^0 density, and fueling rate are lower than the simulation.

This implies the particle flux to areas of the wall which have significant adsorbed gas loads is small as the injection turbulence dies down. One can postulate several mechanisms; the density profile is strongly peaked on the separatrix initially. As it assumes a normal mode, the measured density will drop due to the heavy weighting of the separatrix density in the line averaged microwave interferometer. Thus the early reduction in density may not imply a large flux of particles to the wall.

A second possibility is that a well gettered limiter becomes saturated with gas. Only when saturated would desorption be likely. A monolayer of titanium over 10% of the surface area of the wall is sufficient to adsorb the density initially lost. As this is a reasonable figure for the plasma limiter area, ZD was modified to test this possibility. As expected, the lack of fueling generated an initial fast drop in density, but the corresponding reduction in ion induced desorption so reduced the impurity influx that the electron temperature decay could no longer be maintained.

The initially fast density decay is most likely due to a combination of saturation of poorly gettered wall and the evolution of the density profile as injection turbulence dies down.

The primary problem the code has is in modeling the evolution of atomic hydrogen density. This specie is extremely sensitive to wall and neutral transport parameters. A factor of two decrease in the

recombination rate at 3 eV brings the code results in line with the data. The simple treatment of neutral transport and limited treatment of spatial anisotropies can also easily account for the disparity. Finally, no account of the field line movement has been included. A far more detailed treatment of both rate coefficients and spatially dependent effects is required to accurately model atomic hydrogen.

Impurities

Neutral impurities are desorbed from the walls just as molecular hydrogen is, with similar energy thresholds. Unlike hydrogen, impurities continue to radiate after being ionized. As discussed in Chapter 4, one must perform the time dependent coronal equilibrium calculation to follow the densities of all possible charge states of the impurity. Only then can the radiated power be calculated as this is a strong function of energy which is unique to each charge state.

Recall that a neutral entering a hot plasma radiates ferociously until it approaches the coronal equilibrium average ionization state. This process accounts for the rapid cooling of the gun plasmas early in time. Figure 5 shows the calculated evolution of the first 6 ionization states of oxygen, and Figure 6 compares calculated and measured radiated power.

Note that the dominance of radiation from species far from the coronal equilibrium average state implies a significant lack of sen-

sitivity to the specific impurity. As absolutely calibrated spectral line intensities are unavailable, only the relative intensity of a single line versus time is known. Thus the experimental data yield only the energy dependence (via changing T_e) of line emission, general indications of total impurity content (via ZD's calculated electron energy confinement) and a qualitative description of the relative ionization state densities. Since desorption rates are similar for all impurities, and the calculation of state densities is solely dependent on n_e and T_e, the only possible information available to discriminate between impurities is the energy dependence of total radiated power. This energy dependence is quite independent of species (i.e., specific transition energies) because the electron temperature is well above threshold for the states being excited early in the particle's lifetime (i.e., at low ionization states).

The consequence is that virtually identical results can be obtained with any mix of low Z impurities by adjusting the desorption yields. The energy dependence of radiated power in a plasma far from coronal equilibrium is quite insensitive to the quantum mechanical details of the impurities.

The relative ionization state densities and time behavior yield an enormous amount of information, however. Precisely because the plasmas are so far from equilibrium, one has a millisecond time scale, sensitive indicator of the plasma surface interaction. The strong desorption pushes the ionization state density more neutral than coronal equi-

librium yielding a direct measure of the desorption rate. Further, the time scale is sufficiently long that the history of the desorption rate must be accounted for. This yields data on abrupt plasma-wall interactions (e.g., injection transients) otherwise difficult to measure or simulate.

All these features can be seen in evaluating the data and simulations for the gun plasmas. Figure 7 shows the coronal equilibrium charge state density functions for the experimental T_e evolution. Comparison with ZD's state density functions in Figure 8 shows the perturbation from coronal equilibrium.

Derived Parameters

As seen in the previous sections, ZD models the gun plasmas with reasonable precision. To achieve this the code has to calculate a variety of parameters not experimentally accessible. Three 'diagnostics' outputted from the code warrant further discussion. First, particle transport independent of other sources and sinks is essential to the understanding of the plasma. Next, ZD had to account for higher neutral densities in the bridge region. Finally, ZD calculates the total radiated power by adding values calculated for each specie (and, for hydrogenic species, each region).

It is clear that hot ($T_e \geq 10$ eV) plasmas can ionize substantial amounts of hydrogen, and this source term must be taken into

account when studying particle transport. In preparation for the far more dramatic RF shots, a comparison of the density decay time with the particle confinement time (both from ZD) is shown in Figure 10. Neutral ionization dominates the density decay rate when $T_e > 10$ eV. While moderate electron temperatures are required for significant ionization, there must also be a source of gas. Particle induced desorption of H_2 is strongly temperature dependent and produces large quantities of gas only when the plasma is capable of ionization. The combination of thresholds in ionization (and radiation) and desorption rate abruptly terminates fueling after about 2 milliseconds.

The sharp reduction in the temperature decay at 2 milliseconds is due to two effects. First, the termination of desorption removes the source of H_2 and neutral impurities. Second, the reduction in electron temperature causes the average charge state of the impurities to exceed that of coronal equilibrium. Impurity radiation falls dramatically as the electrons are unable to excite the impurity ions.

The desorption rate is critically dependent on the wall surface condition. This fact is included in ZD by allowing desorption only in non-gettered regions (the bridge). As expected, the density of desorbed neutrals is much higher in the bridge region. Figures 10 and 11 show the H^0 and H_2 densities for the bridge and central regions. The factor of 3 increased density in the bridge has a number of consequences. Virtually all spectroscopic, charge exchange and bolometric diagnostics

view the central region of the experiment. Thus if such a diagnostic is sensitive to a neutral specie density it will underestimate that density by a volume weighted factor of 2. The charge exchange analyzer is routinely used to estimate the power loss due to charge exchange. At least a power equal to the central region losses occur in the bridge regions, unseen by the analyzer.

Similarly, the 'Thinistor' bolometer was absolutely calibrated but indicated a factor of 2 lower power than expected. This is now understood in light of the enhanced losses in the bridge region.

Discussion

The gun-only shots are seen to have plasma parameters determined largely by initial conditions. The rapid drop in T_e quickly turns off desorption and at 2 msec, most radiation. The code has problems tracking the initial, turbulent evolution of the plasma. This phase is treated by modifying the initial conditions. Correct electron temperatures are obtained but the density decay and wall flux are in error.

The H_2 density is a direct indicator of wall flux, and while T_e is above 10 eV, the density decay rate should indicate fueling efficacy. Note that ZD shows significant fueling and H_2 densities during the first millisecond, in contrast to the experimentally rapid density decay and low H_2 density.

Yet the data indicate, and the code correctly simulates, the

temperature decay. This behavior confirms that the initial impurity load is responsible for the initial cooling of the electrons. The preceding discussion illustrates the use of ZD to gain understanding of experimental data. Another use of the code is to ascertain what parameters are unimportant to the plasma evolution. The first observation is that the ion flux to the limiter is not energetic enough to significantly deplete the limiter gas load. (This in marked contrast to RF shots.) Second, tests indicate the code results are insensitive to the region the limiter is located in.

Finally, the sensitivity of the code results to neutral hydrogenic species densities should caution us to consider the effect of rate coefficient inaccuracies. At low electron temperatures typical of the last half of the shot, the threshold energy for atomic processes is several times the electron temperature. Thus only the energetic tail of the electron distribution participates, and the rate coefficients are extremely sensitive to the threshold behavior of the cross section. Even simple systems (H^0 and H_2) have large uncertainties in cross section near threshold. Clearly better rate coefficients are required for improvements in low T_e behavior of plasma simulation codes.

Within the range of validity of the approximations used ZD produces a very reasonable simulation of the plasma. The insight gained from the detailed and physically realistic code permits an accurate interpretation of experimental data.

Figure 1: The electron temperature decay is plotted as measured (data) and calcualted by ZD (code).

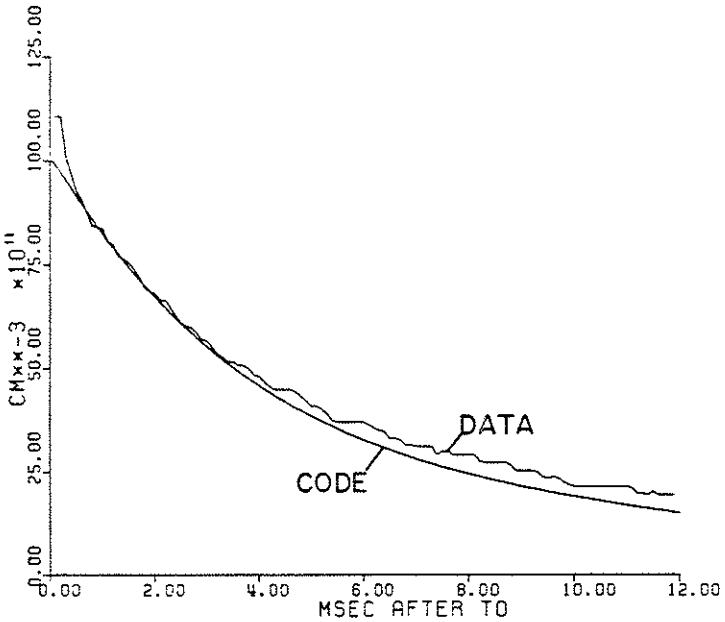

Figure 2: The electron density decay is plotted as measured and calculated.

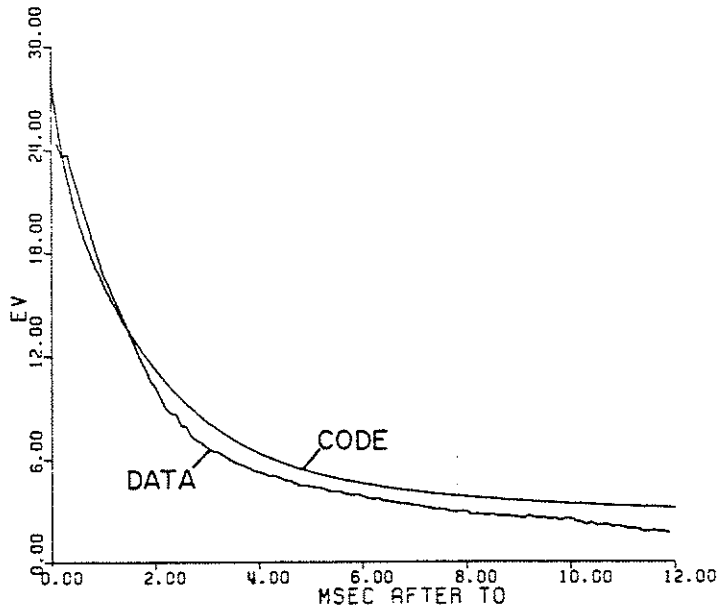

Figure 3: H^0 and H_2 relative densities as a function of time inferred from VUV lines at 1215 Å and 1613 Å (respectively). Each curve is separately normalized to an average value of 1.

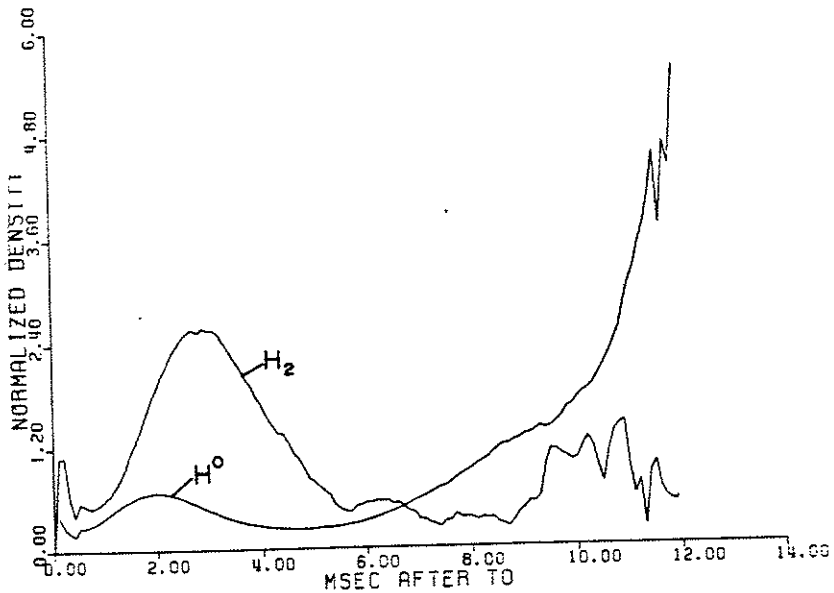

Figure 4: H^0 and H_2 densities calculated by ZD.

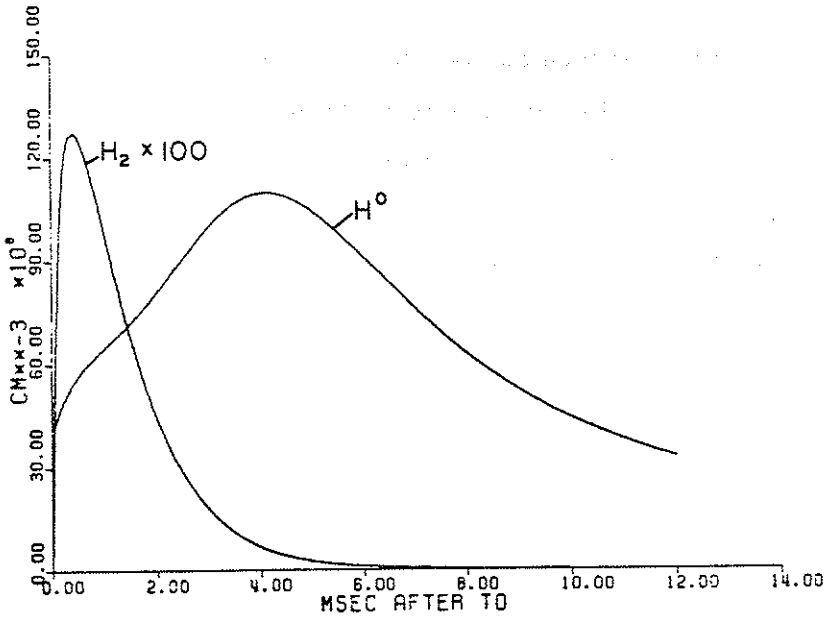

Figure 5: The calculated evolution of the first six ionization states (neutral through O^{+5}). Densities are absolute.

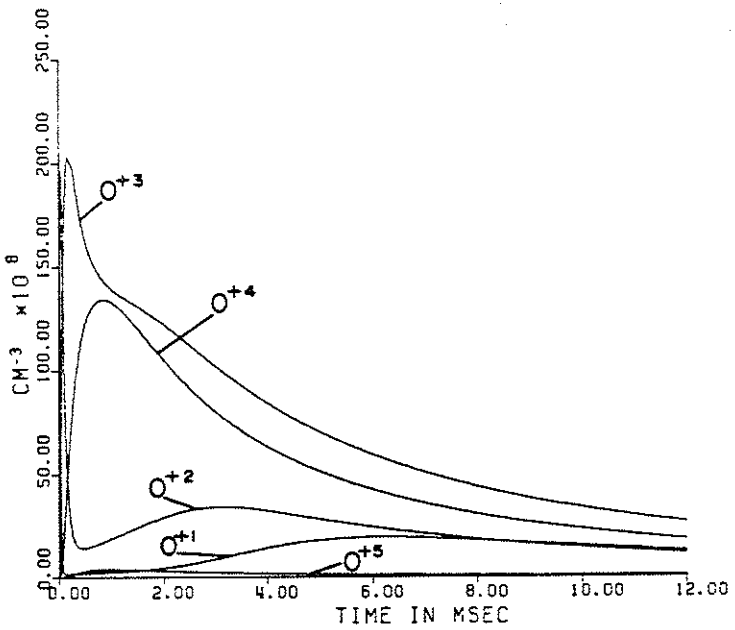

Figure 6: A comparison of the calculated total radiated power and the relative radiated power measured by the SnGe filtered channeltron. The code results are presented in two forms. First is the results from the code. The second form has been numerically filtered to match the characteristics of the channeltron amplifier

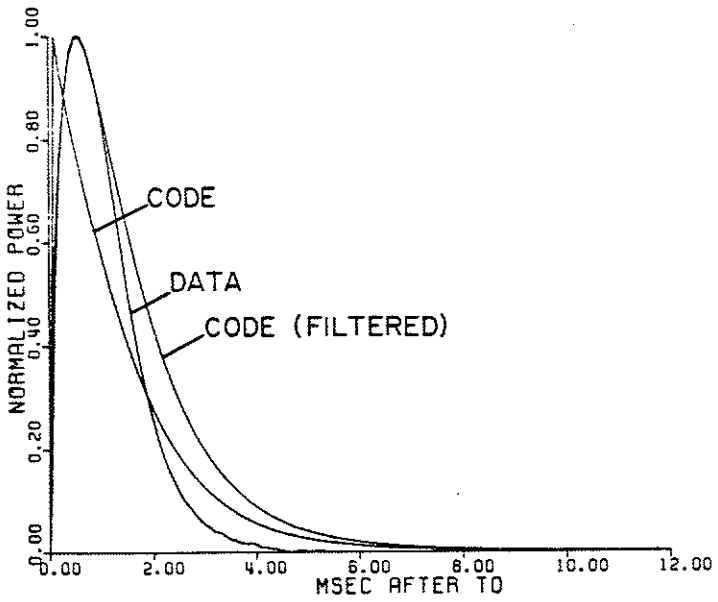

Figure 7: The fractional population of charge states of oxygen assuming coronal equilibrium at the experimentally measured electron density and temperature.

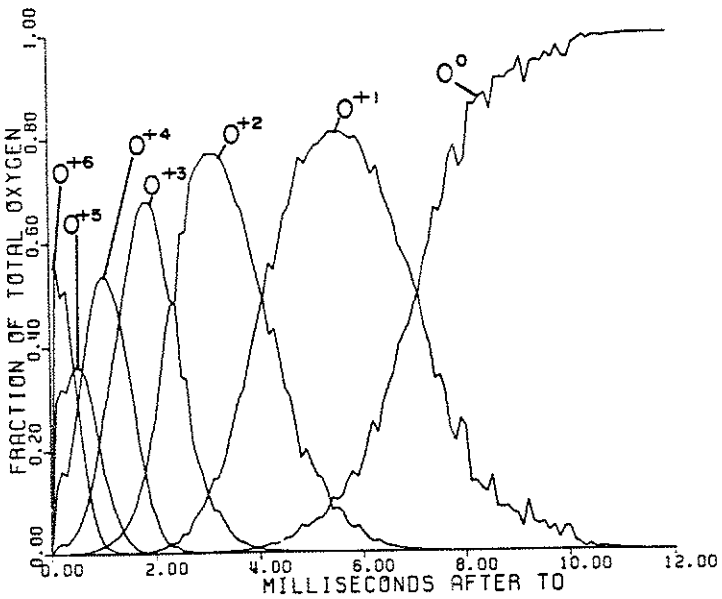

Figure 8: The fractional population of charge states of oxygen as calculated by ZD.

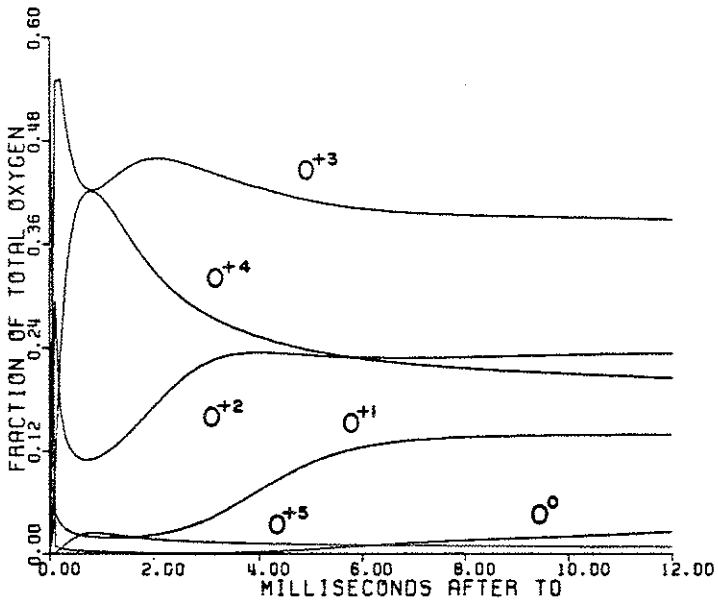

Figure 9: The measured density decay time scale $(\frac{1}{n}\frac{dn}{ct})^{-1}$ is compared to the confinement time derived from the particle transport used in ZD.

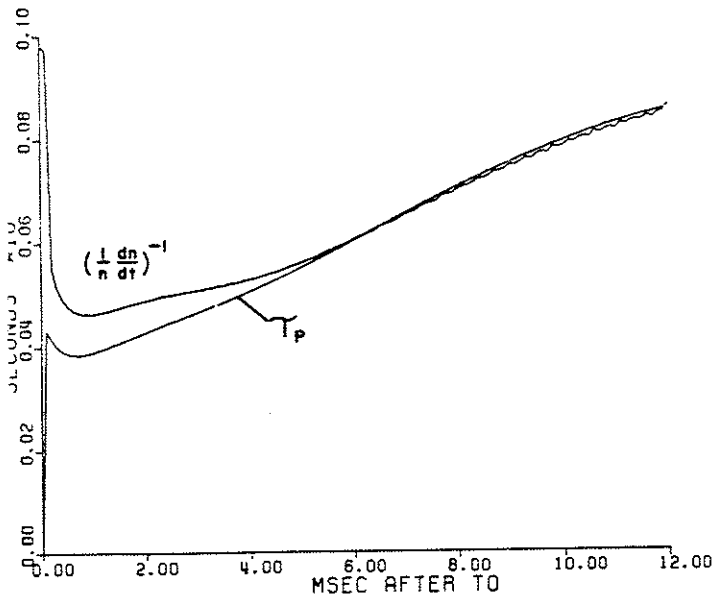

Figure 10: Calculated atomic hydrogen densities for the bridge and central regions.

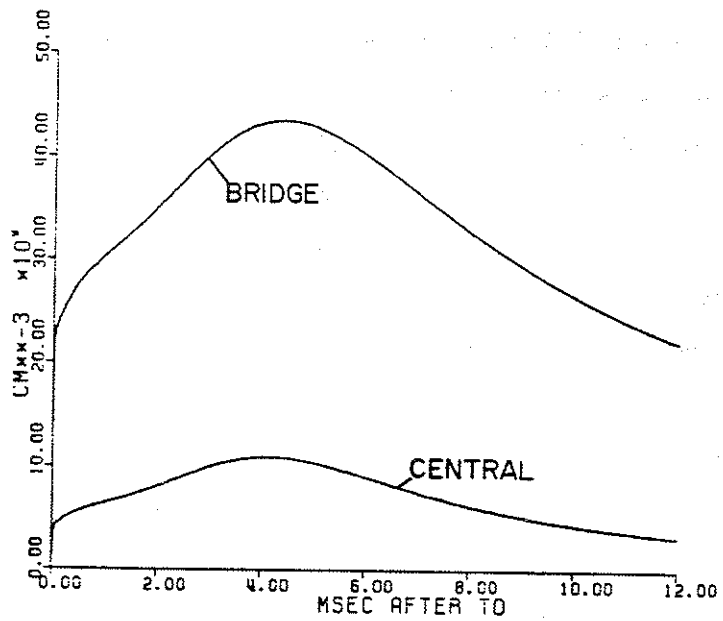

Figure 11: Calculated molecular hydrogen densities for the bridge and central regions.

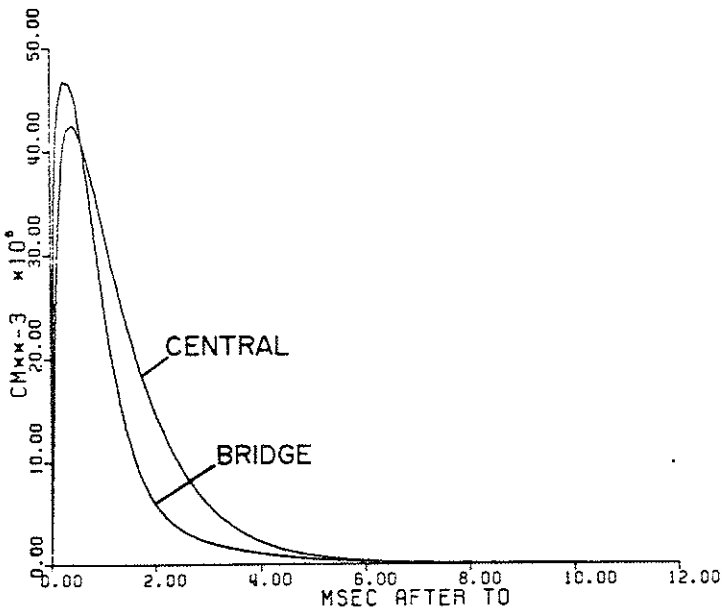

CHAPTER 6

ICRF HEATED PLASMAS

Overview

The addition of ICRF power remarkably alters the behavior of the plasma. Many of these changes are due to the simple fact of higher, sustained ion temperatures. Desorption continues as a strong process throughout the shot. Basic plasma parameters are, then, determined by the equilibrium between strong, competing processes: charge exchange and line radiation (due to the large influx of neutrals from the wall) balance the ICRH power, and ionization of desorbed and reflected particles fuel the plasma against transport losses. In addition to these expected processes, ICRH seems to modify the particle transport scaling. Spatial and velocity ion anisotropies dramatically increase wall gas desorption. At low powers these effects combine to actually increase the plasma density.

As the RF power is raised, the evolution of the plasma shifts. Figures 1 through 4 show the electron temperature and density and H_2 and H^0 relative density evolution for a range of RF heating powers. In gun-only shots desorption is important only at early times. Adding ten kilowatts increases T_i and T_e, but their values remain below the desorption threshold. Thus at very low powers one sees T_e remaining

constant, a fraction of an eV above the gun only case. At about 30 kW, the edge ion temperature exceeds the desorption threshold. (This is a soft threshold so there is a gradual change in behavior as power is increased.) Ion induced desorption now produces significant amounts of H_2, and dissociation and ionization fuel the plasma.

The edge ion temperature is quite sensitive to charge exchange and elastic collision energy losses. This provides a strong feedback mechanism to set the electron temperature at a constant value. If T_e rises T_i increases (due to the ion-electron collisional coupling) which increases desorption. Increased desorption increases energy losses, reducing T_e and T_i. The 50 kW case illustrates the remarkable stability of this mechanism.

The density is also seen to remain constant after falling to an equilibrium value. Like T_e, the equilibrium density rises linearly with power at low powers. The mechanism maintaining the equilibrium is implicit in the electron temperature feedback. As T_e rises, the ionization rate rises. The increased ionization increases the density, which in turn increases the desorption rate due to the increased flux of ions to the wall. The larger flux of desorbed neutrals reduces T_e, and the ionization rate.

Above 100 kW, the edge ion temperature becomes gyroradius limited. The desorption rate now decouples from T_e and the feedback mechanisms are lost. As power is increased T_i increases which heats the

electrons. The electron and ion temperatures become less coupled as T_e rises due to the $T_e^{-\frac{3}{2}}$ scaling of the ion-electron collision frequency. This permits ion temperatures in excess of 100 eV. Hot ions having larger gyroradii diffuse faster, increasing the particle loss rate while the desorption yield remains constant due to the gyroradius limit of ion energy. Since the effective ion fueling fraction is less than 1 (particles added to plasma per ion hitting the wall), the density now decreases as power increases.

The 200 kW case shows the transition through the various regimes. On injection, the electron temperature drops rapidly as desorbed neutrals and impurities radiate. The ion temperature rises, eventually supporting T_e at 15 eV (at 4 milliseconds). The hot ions are lost faster than fueling can replenish them but the density decay is seen to be substantially reduced. As the density drops the desorption rate drops (seen by a steadily decreasing H_2 density) and T_e rises. T_i decouples from T_e (due to the density dependence of the ion-electron collision frequency) and rises dramatically, and the density now drops rapidly. Note however that while $(\frac{1}{n}\frac{dn}{dt})^{-1}$ is about that of the gun-only shots, there remains substantial fueling. Particle confinement is far shorter than the density decay would indicate.

At high power ($\gtrsim$ 500 kW) ion heating is strong enough that the electrons are never strongly coupled to the ions. The high ion temperature causes plasma transport that fueling cannot compensate

for and the density uniformly drops.

The preceding description leaves a variety of important processes unmentioned. RF power coupled to the ions is not linear in ion density; thus ion heating per ion is stronger at lower densities (down to $2 \times 10^{12}\text{cm}^{-3}$). Charge exchange plays a vital role as energetic neutrals can impact non-gettered walls inaccessible to the ions. Once again, the regional behavior of neutral densities is critical. The hot edge ions and their extreme velocity anisotropy play a central role in setting the desorption yield. Charge exchange in the edge region, while contributing a small fraction of the total neutral flux to the wall dominates the total neutral induced desorption reflux.

Clearly, spatial and velocity anisotropies play a major role in establishing the plasma behavior. ZD is moderately successful simulating RF heated plasmas, but this has been the case only since a variety of spatially dependent features were added. These include two regions for hydrogen neutrals, the hot edge ions, position dependent limiters, hot edge ion charge exchange of neutrals impacting the wall, treatment of the velocity anisotropy of the edge ions and modeling of the central neutral transport which accounts for spatial variation of the neutral density profile. A number of spatial phenomena have been included implicitly as well. The hot edge ion temperature is determined by a fit to experimental data, not by detailed modeling. Likewise the RF power deposited in the plasma is established by a fit to measured density and

applied voltage dependencies.

It is not surprising, then, that the accuracy of the simulation results degrades for RF heated plasmas. The free parameters require some adjustment for different RF powers to compensate for the simple approximations used to account for grotesquely spatially dependent behavior. Once again, however, the code is used primarily to assist in the interpretation of experimental data. In this light the parameter variations as a function of RF power become useful tools to indicate how the code fails (or succeeds) in accounting for the experimental data.

The variations in parameters, and some crucial data points are reviewed in Table 1 for the three critical cases: gun-only, 100 kW, and 500 kW ICRF power. A review shows the largest variations in parameters are those affecting hydrogen recycling. The factor of 10 difference in H_2 desorption yield and factor of 3 difference in wall gas load indicate ZD still has problems modeling reflux. Before delving into the processes affecting reflux and fueling, a review of the variation in measured plasma parameters *versus* RF power is in order.

Fueling

The data in figures 1 through 4 reflect various stages in the refueling process. Particle transport causes ion induced desorption of H_2. About 50% of the ions hitting the wall reflect as neutrals. Various dissociation processes are possible but the dominant one is

$H_2+e \Rightarrow 2H+e$. The hydrogen is then ionized, fueling the plasma. At each stage there are losses which reduce the fueling efficiency. Ions may hit clean, gettered surfaces. H_2 may traverse the thin bridge region without dissociating. H^0 charge exchanges easily on protons and is quickly lost, but this incurs additional neutral induced desorption and reflection. All these processes have strong temperature dependencies.

A useful analogy to employ for describing the interplay between these processes is classical control theory.

One major process, neutral induced desorption, can be conceptually isolated by treating it as an isolated loop which multiplies neutrals. Some fraction of neutrals in the plasma will impact the wall, creating H^0 by partial reflection and H_2 by desorption. The H_2 dissociates producing additional neutrals. Particle losses in this loop include neutrals hitting gettered walls (not inducing desorption), H_2 leaving the plasma before dissociating, and various ionization processes. There are energy costs in this loop as well.

Desorbed H_2 leaves the wall at thermal velocities. Elastic collisions with ions do substantial heating. Figure 5 shows the evolution of the H_2 and ion temperature for the 100 kW case. This heating of H_2 dramatically reduces the time an H_2 molecule spends in the plasma (its residence time). Charge exchange of H^0 cools the ions. More significantly it increases the desorption yield. The hot edge plasma is responsible for charge exchange of 10-30% of the neutrals leaving

the plasma. These energetic neutrals account for most of the neutral induced desorption.

The neutral recycling is strongest in the bridge. If all ion induced desorption is located in the central region, neutral densities in the bridge are still a factor of 2-5 greater than in the center. This is due to the simple fact that only areas behind the rings are ungettered. Freshly gettered surfaces cannot desorb gas (except thermally).

The central region is, however, most efficient in fueling the plasma for a given gas load. The large size of the region, and multiple charge exchange insure virtually all H_2 is dissociated, and most neutrals ionized. Note that ZD treats atomic hydrogen transport differently for the two regions to account in some measure for these spatially dependent features.

Overall, the 'gain' for the neutral induced reflux cycle is less than one. A gain greater than one would yield exponentially increasing neutral densities. The increasing neutral density would produce a larger electron cooling rate and lower T_e. This in turn would reduce the gain as the ionization cross section drops. Two points should be made: First, this 'gain control' is a very strong mechanism (in control theory it is second order feedback with attendant fast response to first order quantities). Second, the inverse process occurs for gains less than one. Temperatures rise, desorption yields increase and gain increases.

Because the system is driven (much like a thermally stable

subcritical fission assembly with a neutron source) gains will remain somewhat less than one. This however greatly increases the neutral density by roughly 1/(1-gain). Alternatively, the neutral recycle loop is responsible for a fraction of the neutral density equal to the (less than 1) gain. Finally, note that if T_e rises enough to burn out neutrals, or the gas source depletes, the gain will drop.

Ion induced desorption can now be conceptually isolated from the neutral reflux cycle. Ions hitting the wall also reflect as neutrals. About half the incident ion flux sticks to the wall, the remainder re-entering the plasma at somewhat reduced energy. The hot edge plasma is the component which interacts with the wall. The elevated ion temperature tremendously enhances desorption yields.

Only a fraction of the total wall surface acts as a limiter. One of the free parameters for ZD is the limiter area. About 10^{20} particles impact the limiter during the shot. A monolayer of gas has about 4×10^{14} particles/cm^2. A 16 cm wide toroidal strip of limiter has an area of 2×10^4 cm^2. (This is the value used by ZD, corresponding to 5% of the total wall area.) Thus there are 8×10^{18} particles per monolayer on the limiter. Typical desorption yields of 0.1 to 1 can remove 1 to 10 monolayers of gas from the limiter during a shot. Note that smaller limiter areas imply more monolayers are removed for a given gas influx.

At typical base pressures of 10^{-7} Torr, it takes about 10

seconds to adsorb a monolayer of gas on a clean surface. Sticking coefficients drop by about a factor of 10 for each monolayer, so the second layer takes about 100 seconds. Thus two to three monolayers adsorb onto a clean surface during the 150 second interval between shots. There is very complex surface chemistry involved in establishing the depth and composition of adsorbed gas on the limiter surface. While this topic is beyond the scope of this thesis, it is encouraging to note that ZD's results are in accord with the basic characteristics of surface chemistry.

ZD requires a depleting limiter gas load of one to three monolayers to match experimental data. The characteristics of the plasma-limiter interaction dominate the behavior of the plasma as a whole. The neutral recycling process multiplies the effect of desorbing gas from the limiter. The hot edge plasma ensures substantial desorption yields for ions, and increases the neutral recycling gain via increased neutral desorption yields due to charge exchange in the hot edge.

Clearly, the behavior of those processes demands spatial dependencies. ZD has some of the spatial effects explicitly treated by approximation. These take the form of fits to experimental data for the edge ion temperature and velocity anisotropy. Estimates are made for edge neutral charge exchange and neutral transport. The feedback mechanisms responsible for determining the edge ion temperature are lacking. ZD will thus yield accurate simulations only if the assumptions

used would be the consequence of the detailed feedback mechanisms. Thus ZD's physics is correct only if the results match the data, and only to the accuracy that the simple treatment of the hot edge permits. ZD's primary utility lies in interpreting data, not exactly matching experimental data.

Low Power RF

At low RF powers, the plasma parameters scale quite linearly with RF power. Figure 6 shows the density and electron temperature as a function of RF power. Figure 7 shows the late time (equilibrium) hydrogenic species density. The increasing H_2 density shows the increasing gas load as the edge ion temperature increases. Note that the H_2 density increases despite increasing electron density and temperature and reduced residence time. At 100 kW, fueling exceeds plasma transport.

ZD matches the 100 kW case best with a limiter gas load of 5 monolayers and a desorption cover of 3. In this case, the large cover is indicating that desorption yields exceed those of a single monolayer (as expected). Desorption yields 10 times the single monolayer value for multiple layers is not unreasonable, as the upper layers are very loosely bound to the surface.

Above 100 kW the hot ions in the edge plasma become gyroradius limited, hitting a different limiter. There is a great deal of evidence for

this. The hot component of the charge exchange neutral distribution has a sharp transition at 100 kW and 170 eV. Figure 7 in chapter 4 shows this. At high powers, the floating potential in the edge plasma goes negative. Figure 8 shows a profile of V_f before and just after RF shuts off. Negative floating potentials indicate enhanced ion losses. Normal ambipolar transport yields positive floating potentials which electrostatically confine the more collisional electrons.

At high powers, ZD requires very different limiter parameters to match the plasma behavior. The changing limiter characteristics for gyrolimited ions implies multiple limiters. The primary limiter in the Octupole is usually considered the walls out to the nose. The RF antenna has additional limiters slightly below the flux surface intersecting the nose wall. Ion heating is strongest right above the antenna. All this is quite suggestive that the limiter for high power RF shots is the antenna limiter, while at low power, the nose wall is the limiter. It is also observed that much of the nose wall is ungettered, hence heavily gas loaded while the antenna limiters are about 50% gettered. Further, the nose wall limiter is parallel to the field lines meaning a much greater area is available for desorption. The antenna limiters are perpendicular to the field lines, limiting the areas which desorb gas to a gyroradius times the limiter length.

Analysis of plasma transport to limiters is far more complex than the above would indicate. The transport along field lines to a wall

is a two-dimensional problem. Ions diffuse across fieldlines, and travel at about the sound speed (C_s) to the limiter. C_s is independent of ion temperature and density, having a value of about 10^7 cm/sec in RF heated plasmas. The path length along a field line from the antenna to the nose limiter is 100 cm. Clearly a more detailed study is required to determine the plasma transport to the multiple limiters. There is however compelling evidence to support a hot gyroradius limited plasma local to the RF antenna.

When a toroidal field is added to the experiment, the basic plasma parameters are not greatly affected. The hot ion component measured by the charge exchange analyzer indicates a dramatic increase when the field line from the end of the antenna is skewed to the entrance of the analyzer shown in Figure 9. At this toroidal field, the analyzer views a flux tube connected to the ICRF resonance just above the antenna.

In review, to match ZD results to data requires large reflux rates from limiters at low RF powers, and small, depleting limiter gas loads at high power. ZD has trouble accurately matching these fundamentally multidimensional processes, but the factor of 10 changes required far exceed code errors. This behavior implies multiple limiters. Referring back to the data indicates the second limiter becomes important as the hot ion edge plasma becomes gyroradius limited. Toroidal field slewing of field lines to the charge exchange analyzer indicate the

ions just above the antenna have a higher density of energetic ions. The antenna limiters are thus implicated as the gyroradius limiting surface.

The 100 kilowatt case is quite sensitive to parameters affecting fueling. Consequently, a detailed examination of this case is in order. This 100 kW RF heated plasma has the edge ion temperature just below the gyroradius limit. The limiter is then the large area, gas loaded nose wall. The ions hitting this wall have the maximum energy possible. More energetic ions hit the antenna limiter with much less gas adsorbed on its surface. Thus, this case represents the maximum possible neutral gas flux into the plasma.

The measured density and electron temperature for this case are shown in Figure 10 The enormous reflux is sufficient to increase the density at 6 milliseconds. It is instructive to consider a simple analysis of the energy budget for this case. The density remains approximately constant for the majority of the RF heating interval. Approximating the density behavior as $dn/dt = 0$, the ionization rate is easily calculated. If the particle transport dependencies are the same as the gun only case, the particle confinement time is about 4 milliseconds. Since the density remains about constant, each particle lost must be replaced. This implies a fueling rate for the entire plasma of 6.3×10^{21} particles/second.

Fueling is quite inefficient at these low electron temperatures. The total power required for fueling is estimated by following the

processes involved in making an ion from wall desorbed H_2. The H_2 molecules leave the wall at the wall's thermal energy. As they transit the plasma, they thermalize, acquiring about 5 eV. The mean free path for dissociation in this case is 18 cm, or about twice the bridge scale length. When averaged over regions, half the desorbed H_2 transits the entire plasma, and hits a wall. About half of those reflect back into the plasma at reduced energy. Overall, about 8 eV is used thermalizing H_2. H_2 radiates before dissociating, removing 10 eV from the plasma. After dissociating, the two H^0 atoms radiate as well. This uses an additional 30 eV. On average one of the two H^0 atoms is lost to the wall. 85% of these carry their 10 eV thermal energy, and 15% charge exchange in the hot edge plasma removing 170 eV. Thus the lost H^0 atoms carry 33 eV to the walls. Finally, an ionization occurs using 13.6 eV. Thus the total energy required per ion added to the plasma is 94 eV. The observed fueling thus requires 95 kilowatts. Note that T_e and T_i are roughly constant so the stored energy of the plasma is not used to supply this energy. Further, the total stored energy is initially only 240 joules, one fifth of the energy required. The estimates above show fueling requires almost all the power that is input to the plasma. These estimates assumed no other losses. Charge exchange and impurity line radiation reduce the power available for fueling. The low temperatures keep these incidental losses at a minimum, but also increase the energy per ionization for fueling (radiation requires excitation by lower energy

electrons than ionization).

ZD cannot even approach holding the density constant with transport parameters set to the gun-only cases, as expected. Several possibilities for resolving the dilemma are: a) the plasma transport is reduced due to RF, b) rate coefficients are in error, or, c) processes not yet considered enhance the fueling efficiency.

ZD uses an extensively studied two-component transport dependence.[3] The diffusion coefficient is the sum of classical scaling and vortex scaling terms. The vortex diffusion term uses an effective turbulence temperature of 2.5×10^4 eV. The value of the classical scaling component of the diffusion coefficient is taken as 15 times the classical value. The factor of 15 corresponds to the usual factor of 10 for gun-injected plasmas[3] when actual density scale lengths are taken into account. It was found that reducing the classical anomaly factor to 2 to 5 produces the best match between ZD and the data.

The mechanism responsible for anomalous classical scaling particle transport is not understood. One can speculate that RF destroys the coherence of collective effects enhancing transport. Large ion gyroradii, and a sheared toroidal plasma flow due to both spatial variation of T_i and radial electric fields caused by gyrolimited ions would be effective at shorting out potentials supporting drift waves. Such considerations are well beyond the scope of this study. Further, the confidence in the conclusion that reduced transport is responsible for enhanced fueling is

subject to question.

The second possibility for increased fueling was error in rate coefficients. The strong fueling makes ZD quite sensitive to the hydrogen rate coefficients. With T_e near 10 eV the Maxwellian averages heavily weight the threshold region of the cross sections. Recent studies indicate a possible 60% error in accepted cross sections for atomic hydrogen near threshold, and factor of 2 errors for H_2.[4] While existing data and theory match reasonably well for these rate coefficients,[5] such measurements are difficult and hotly debated.[6] Since the issue cannot be resolved without more accurate rate coefficients, the question will be left hanging with the often repeated lament that plasma modeling demands better atomic data.

Finally, could enhanced fueling be due to processes not yet considered? One such possibility is ion induced or enhanced H_2 dissociation. A cursory search of the literature and inquiries to several physicists studying molecular hydrogen yielded no references. Classically, ions would be expected to be quite effective at inducing vibrational excitation and dissociation in molecular H_2. The heavy ion should be quite effective in coupling momentum to the nuclei of the molecule. Vibrational states of homonuclear molecules have long lifetimes (10^7 sec). Electron induced dissociation of vibrationally excited molecules can be a factor of 2 larger than for the ground state.[8] Ion induced dissociation is both energetically possible, and classically has a larger

cross section than for electrons due to the close match of momentum.

At 10 eV electron induced vibrational excitation of H_2 has a rate coefficient[7] of about 1×10^{-9} cm^3sec^{-1}. The hot ions have velocities of 4 eV electrons, which will contribute an additional 2×10^{-9} cm^3sec^{-1}. (This ignores possible enhancements to vibrational excitation by ions due to small impact parameter collisions.) The total vibrational excitation rate of 3×10^{-9} cm^3sec^{-1} is one third of the dissociation rate.[5] Clearly a more complete study is called for as the above only considers one initial rotor state, and a single final vibrational state.

H_2^+ dissociation at energies below 15 eV is known to be strongly dependent on vibrational state.[8] Data used in ZD assumed $\nu = 0$ whereas Franck-Condon factors make $\nu = 3$ the most probable final state for molecular ionization.[9] Below 10 eV this can increase the rate coefficient by three orders of magnitude.[5] It is observed that since H_2^+ is magnetically confined, its lifetime in the plasma is a particle confinement time. Hence the error in fueling rate will depend on other rates for destruction of H_2^+. For the 100 kW case, dissociative recombination will dominate. Thus the errors in vibrational state of H_2^+ shift the $H_2 \rightarrow H_2^+ \rightarrow H^+ + H^0$ path to $H_2 \rightarrow H_2^+ \rightarrow 2H^0$. This may halve the fueling efficiency, but only below about 15 eV.

The author's experience running thousands of simulation cases indicates ZD underestimates H_2 dissociation rates. Also, the rapid

drop in T_e and increase in H^0 density after RF shutoff imply reduced plasma transport which returns to non-RF values when the RF is removed. The complex initial behavior of the density correlates with both T_e approaching cross section threshold energies and hot edge ion temperature increases. Further study of fueling at low temperatures and particularly vibrational excitation effects on rate coefficients is clearly indicated.

High Power RF

At high powers (500 kW) the plasma behavior is no longer dominated by fueling. The intense recycling of the 100 kW case is eliminated because the antenna limiter quickly depletes its gas load. The 25 to 40 eV electron temperatures result in several major changes in the plasma behavior. The ion temperature decouples from the electrons. Hydrogenic ionization is more efficient. Finally, impurity line radiation becomes a substantial energy loss.

Figures 11 and 12 show the data and ZD's results for electron density and temperature. The initial drop in T_e is due to the influx of hydrogen and impurities by ion induced desorption. As the gas on the limiter depletes, the gas's influx is reduced lowering the power removed from the electrons by radiation and ionization. T_e then rises. The peak electron temperature is reached at the end of the RF pulse.

Late in the shot, the electron temperature is limited by impurity line radiation and reduced coupling to the ions due to reduced density and elevated temperatures. Charge exchange becomes more important as T_i rises, removing more energy per event.

The basic shape of T_e with its initial decline is due to a depleting limiter. Well over a year was spent exploring alternative processes. These included neutral gas flowing from the gun, successive refinements in neutral transport and desorption and direct ohmic heating of electrons by RF. The requirement for consistent behavior across RF powers and detailed comparison of the entire data sets demonstrated these alternatives to be unphysical.

The H_2 density is a good indicator of the accuracy of the reflux modeling. Figure 13 shows the relatively calibrated measured data and the code results. One would expect the atomic hydrogen density to show similar behavior. Figure 14 shows a comparison of code and data for central region H^0 density. The large difference in peak to 10 millisecond ratio between the two is due to several effects. First, the zero-dimensional nature of the code enforces a uniform density in the central region. The data are taken at a single toroidal location about a charge exchange mean free path toroidally away from the end of the antenna. Also, the neutrals are modeled in only two regions. While this appears adequate for modeling the major features affecting confinement, it is clearly inadequate for detailed spectroscopic work on H^0.

Transport of atomic hydrogen in the large central region is dominated by charge exchange. To adequately treat H^0 transport in the complex octupole geometry requires Monte Carlo techniques. The computer time required for such an analysis is prohibitive. Such detailed treatment is both unnecessary and in light of other accuracy limitations unwarranted.

After the RF shuts off, the code indicates a much slower electron cooling rate than is observed. This is easily understood in light of the lower hydrogen densities the code generates late in the RF pulse. Small increases in this density will dramatically increase the cooling rate as the electron temperature drops. Note however that the initial cooling rate on RF shut-off is too small. This directly implies the code has underestimated the electron cooling rate, or overestimated the power coupled to the electrons from the ions.

Late in time, as the density decays, the ion temperature rises dramatically (Figure 18), and cools slowly after RF heating ends. Experimental data do not show such effects. The measured, sustained H^0 densities and roughly constant ion temperatures indicate a strong feedback mechanism using charge exchange to limit ion temperatures. Recall desorption is a strong function of impact energy, and is very effective at producing gas at these energies.

Such a process is produced by the code when wall gas loads are large, but the simple modeling of neutral transport results in substantial

fueling. Once again, the limited treatment of spatial effects limits the code's accuracy. A very limited amount of spatially resolved data are available. They offer a final demonstration of the severity of spatial inhomogeneities for atomic hydrogen.

Figure 19 shows an angular scan of H_β intensity taken from a port directly above the antenna. The antenna and the bridge region are seen to have enhanced hydrogen densities (assuming uniform electron temperatures). Figure 20 shows the time evolution of H_β intensity at several angles, and the results when the probe is located on the outside wall viewing a ring through the bridge plasma. These data have been normalized to the total path length viewed.

These data add confidence to the multiple limiter hypothesis. As the ions heat early in time the H^0 density is seen to shift from the bridge to the central region. Dramatically enhanced bridge region neutral densities are also confirmed.

With the interpretation of basic processes provided by the code, the experimental data are easily understood. A comparison of impurity charge states shows (Figures 15 and 16) a reasonable match between code and data. The behavior of the bolometric data is shown in Figure 17. Recall that a component of the Thinistor signal is due to the incident neutral flux. This produces a larger signal for hotter, RF heated plasmas compared to the filtered channeltron. The code results show the total radiated power summed over all regions. As

the heating power is raised, desorption in the bridge region causes dramatically enhanced radiation in this volume. The Thinistor and channeltron do not view this region which accounts for about half the volume integrated radiated power. When these factors are taken into account the data presented in Figure 17 are seen to be remarkably consistant. The agreement between Thinistor, filtered channeltron, and code results gives a great deal of confidence in the understanding of impurity behavior.

Since the impurity lifetime is long compared to that of neutrals, spatial inhomogeneities have time to smooth out. Note that impurity ions are assumed to transport along with the entire plasma. This eliminates the possibility of wildly different impurity transport.

In summary the high power cases are easily understood in terms of an initial gas load due to depleting limiter gas loads. While detailed modeling of atomic hydrogen presents difficulties, ZD is quite successful in determining the basic mechanisms responsible for the plasma's behavior. Like the gun only case, interpretation is simplified by the existence of discrete regimes of reflux rates. For high power RF heated plasmas this characteristic gives independent parameter control of the code results. It is thus easy to match the code and data.

The confidence in the result of the code lie first in its limited use to help interpret experimental data and second in the reasonable consistency of the free parameters across an enormous range of heating

power.

References for Chapter 6

[1] J.R. Patau, University of Wisconsin PLP-558 (1974).

[2] E.J. Strait, University of Wisconsin PLP-881 (1972).

[3] H.R. Garner, Ph.D. thesis, University of Wisconsin (1982).

[4] J. Furst, private communication.

[5] E.M. Jones, Culham Laboratory Report CLM-R175 (1977).

[6] D.E. Golden, private communication.

[7] M.A. Morrison, A.N. Feldt, and B.C. Saha, private communication.

[8] J.M. Peek, *Phys. Rev.* **134**, 877(1964).

[9] G.H. Dunn and B. Van Zyl, *Phys. Rev.* **154**, 40(1967).

[10] E.J. Strait, University of Wisconsin PLP-903 (1983).

Figure 1: Measured electron temperature evolution for gun only, 14 kW, 50 kW, 100 kW, 200 kW and 500 kW ICRF heating powers.

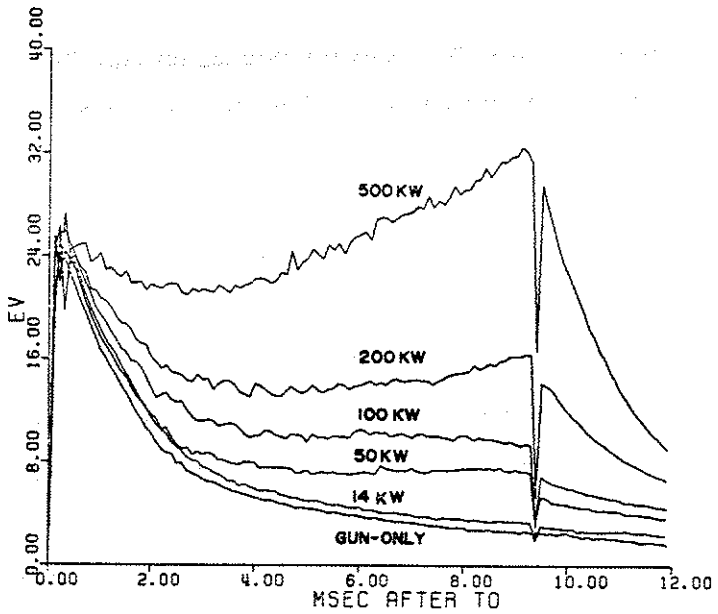

Figure 2: Measured electron density evolution for gun only, 14 kW, 50 kW, 100 kW, 200 kW and 500 kW ICRF heating powers.

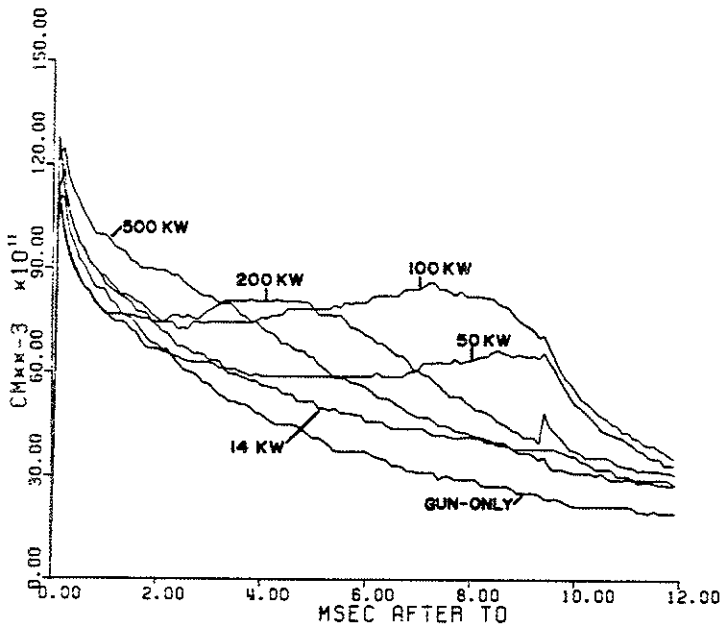

Figure 3: Measured relative H_2 density evolution for gun only, 14 kW, 50 kW, 100 kW, 200 kW and 500 kW ICRF heating powers.

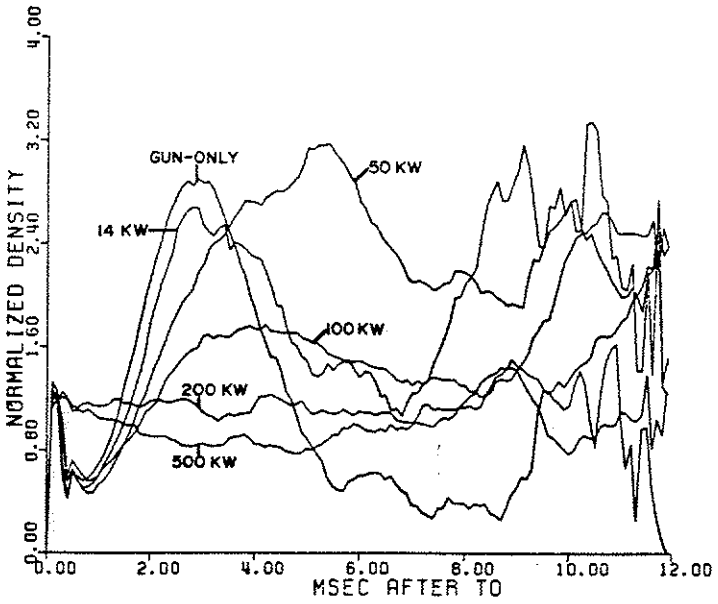

Figure 4: Measured relative H^0 density evolution for gun only, 14 kW, 50 kW, 100 kW, 200 kW and 500 kW ICRF heating powers.

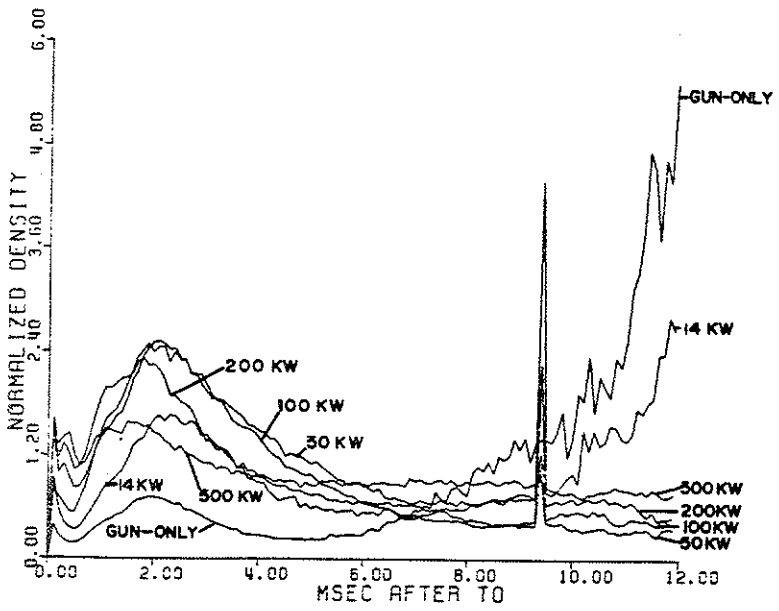

Figure 5: Calculated H_2 temperature evolution compared with ion temperature for 100 kW case.

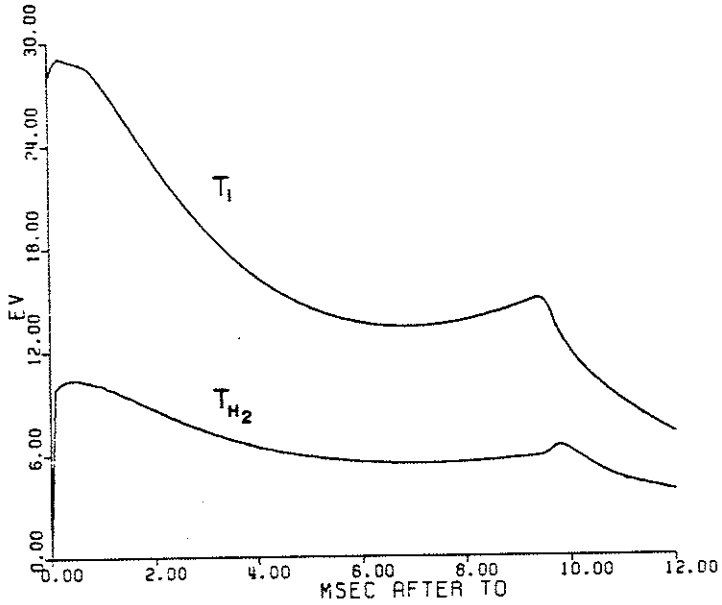

Figure 6: Equilibrium (8 msec) density and temperature versus RF power.

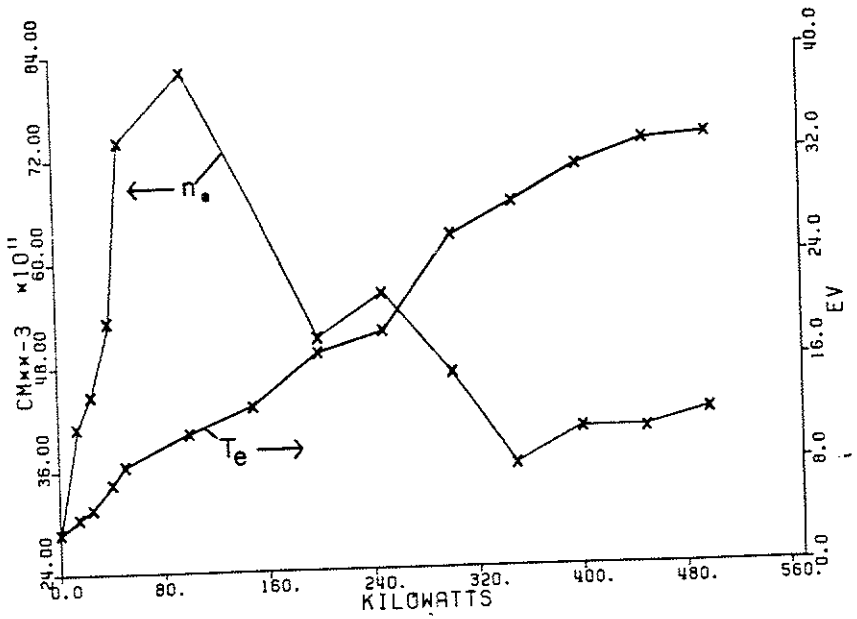

Figure 7: Equilibrium (8 msec) relative H^0 and H_2 density versus RF power.

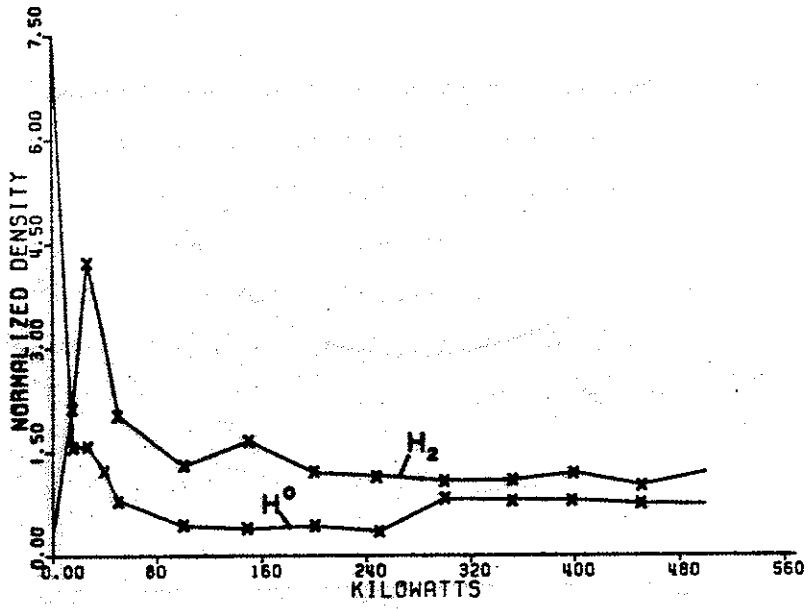

Figure 8: Floating potential versus ψ (flux coordinate) before and after RF shutoff. Data were taken by Dr. Strait.

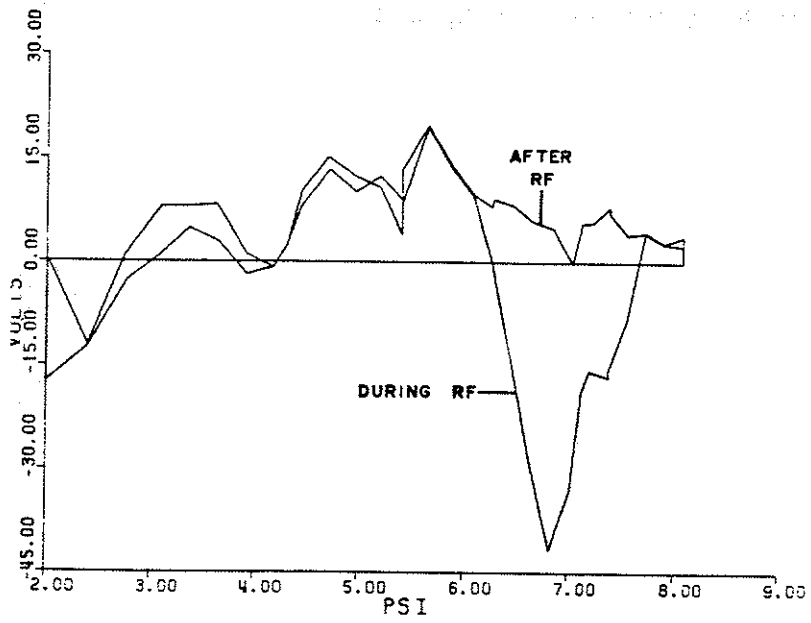

Figure 9: Charge exchange ion temperature and power versus toroidal field. The power calculated from charge exchange data assumes toroidal and poloidal uniformity of neutral flux. Data were taken at reduced poloidal field to permit slewing the flux tube from the end of the antenna past the analyzer. B_T bank voltage of 300 volts slews the flux tube to a location directly under the charge exchange analyzer. Data taken by Dr. Strait.[10]

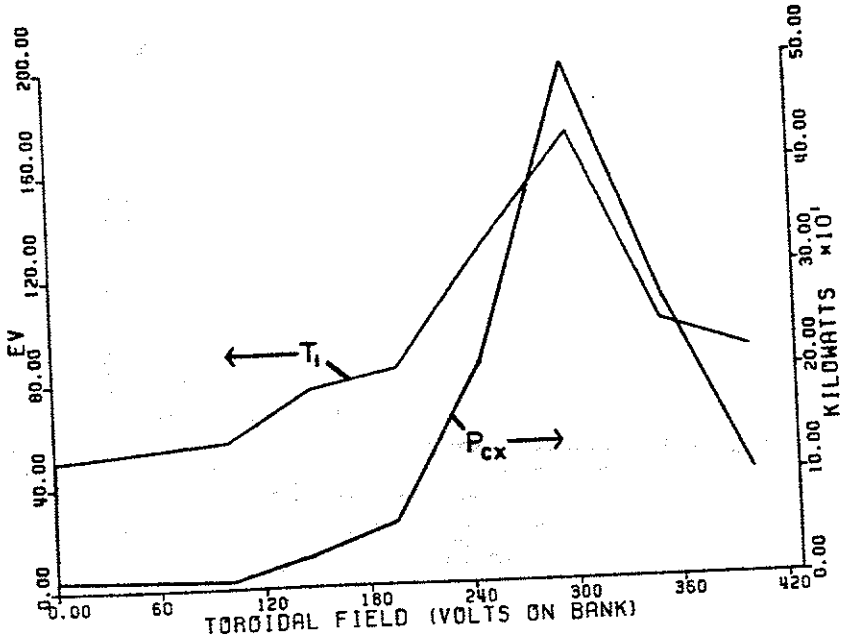

Figure 10: Measured electron density and temperature evolution for 100 kW ICRF heating.

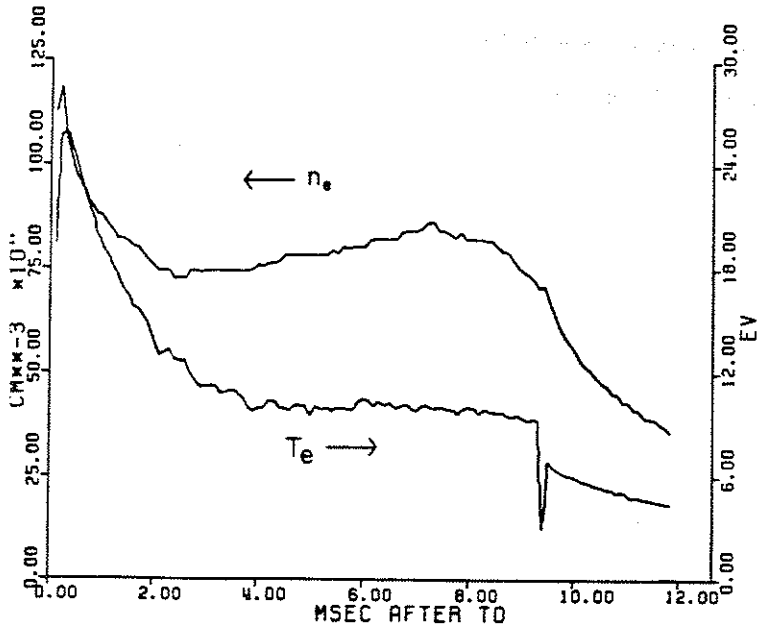

Figure 11: Comparison of code and measured data for electron density evolution at 500 kW ICRF heating power.

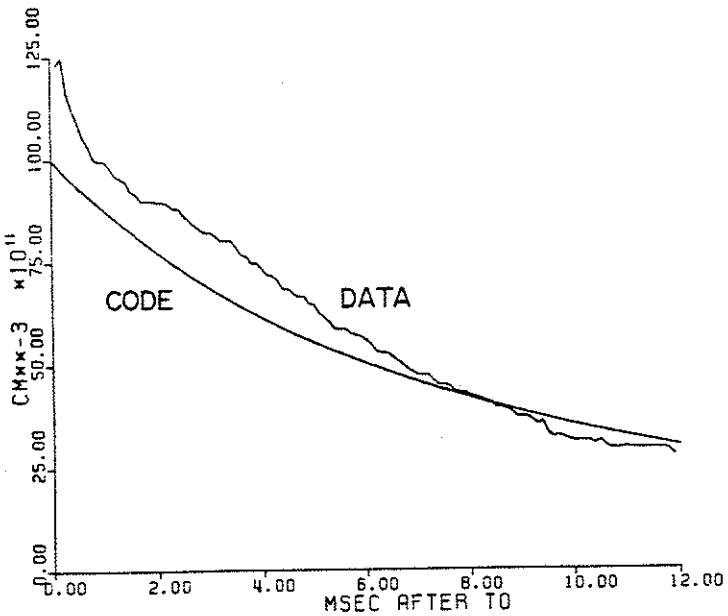

Figure 12: Comparison of code and measured data for electron temperature evolution at 500 kW ICRF heating power.

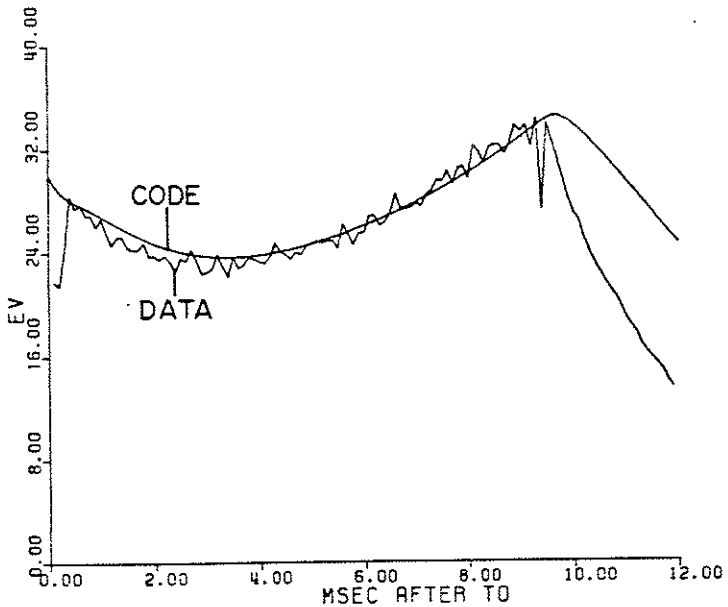

Figure 13: Comparison of code and measured data for relative H_2 density evolution at 500 kW ICRF heating power.

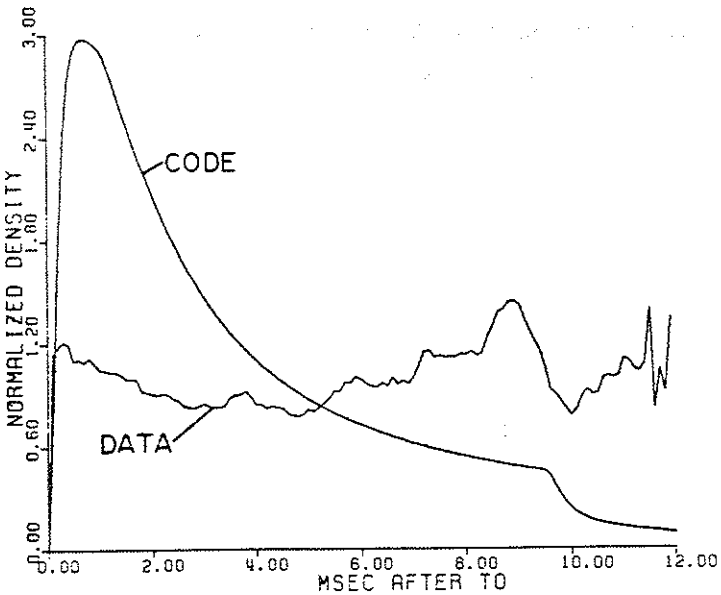

Figure 14: Comparison of code and measured data for relative H^0 density evolution at 500 kW ICRF heating power.

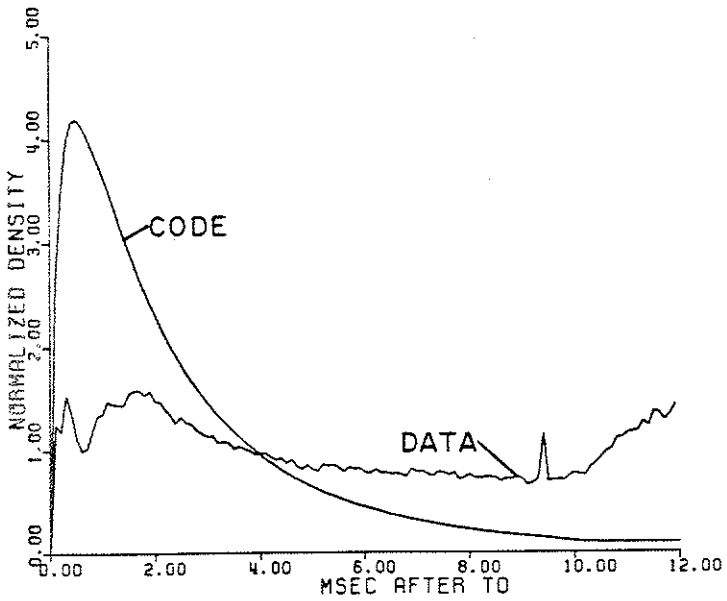

Figure 15: Normalized oxygen charge state distribution evolution measured for 500 kW case. Data for each charge state is individually normalized to a peak value of one.

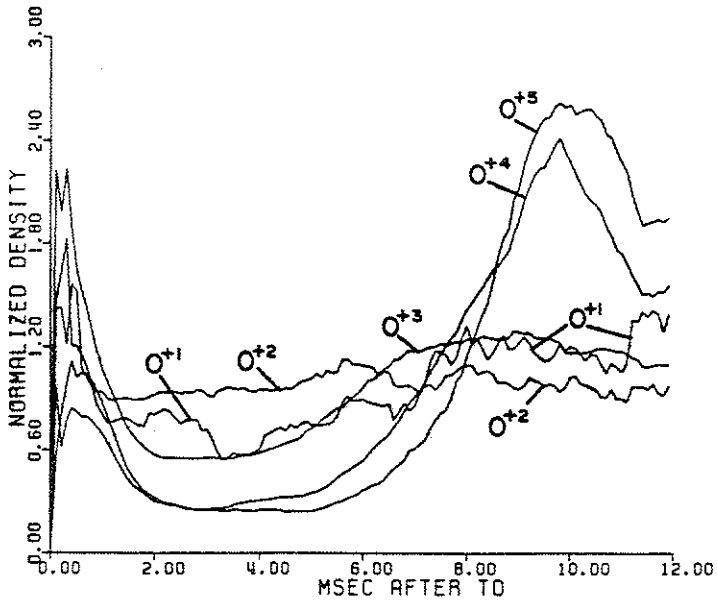

Figure 16: Code results for oxygen charge state distribution evolution for 500 kW case. As in Figure 15, data for each charge state are normalized.

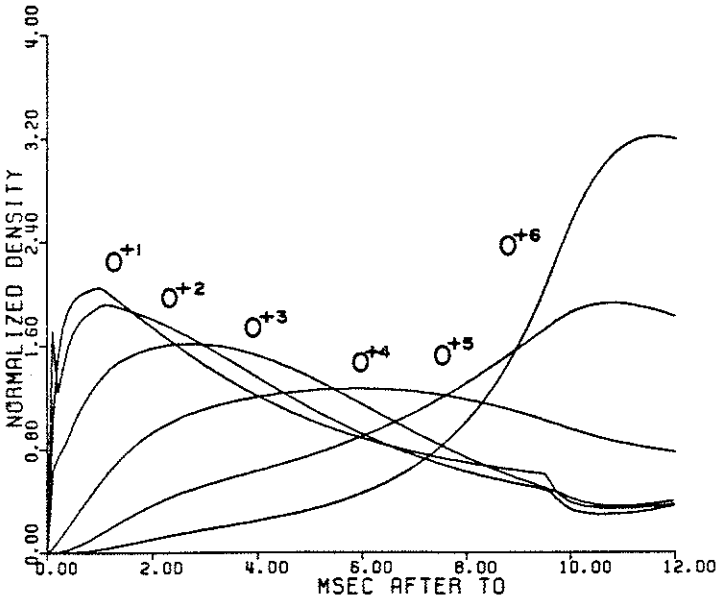

Figure 17: Time integrated total radiated power evolution. Data plotted are Thinistor, SnGe filtered channeltron and code results. Data are for 500 kW case. Data are normalized to one for gun-only case.

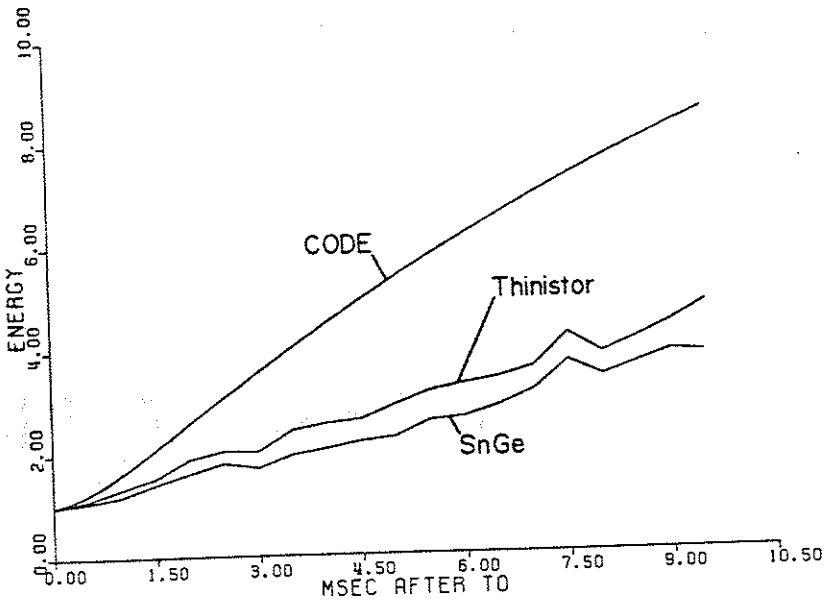

Figure 18: Calculated ion temperature for 500 kW ICRF heating case. Note that for zero-D modeling the ion temperature is considered an average over the velocity anisotropy and position.

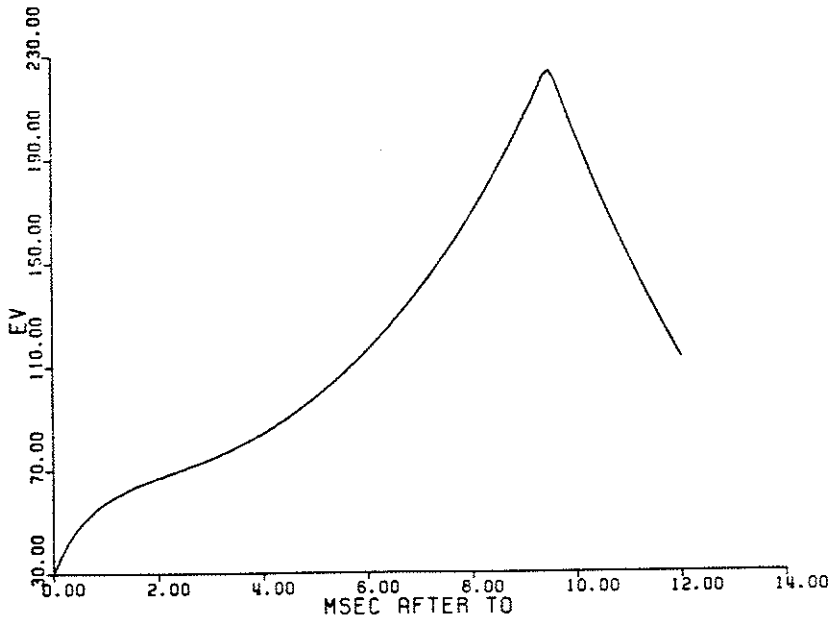

Figure 19: The measured H_β light at 1.5 milliseconds for a 500 kW case. The angle is referenced to a vertical chord in a poloidal plane. Data are normalized to path length. The ring location is noted.

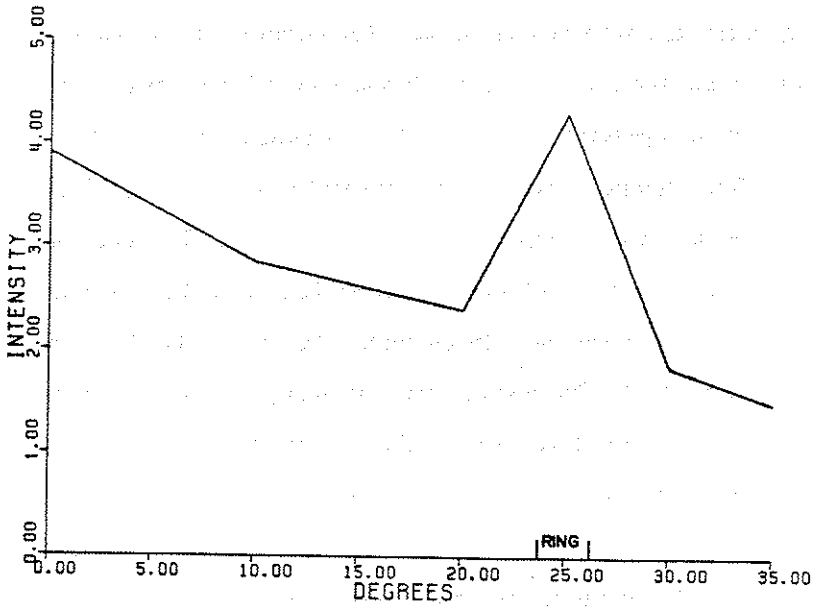

Figure 20: The time evolution of H_β light at several angles, and across the bridge region. The data are normalized to path legnth.

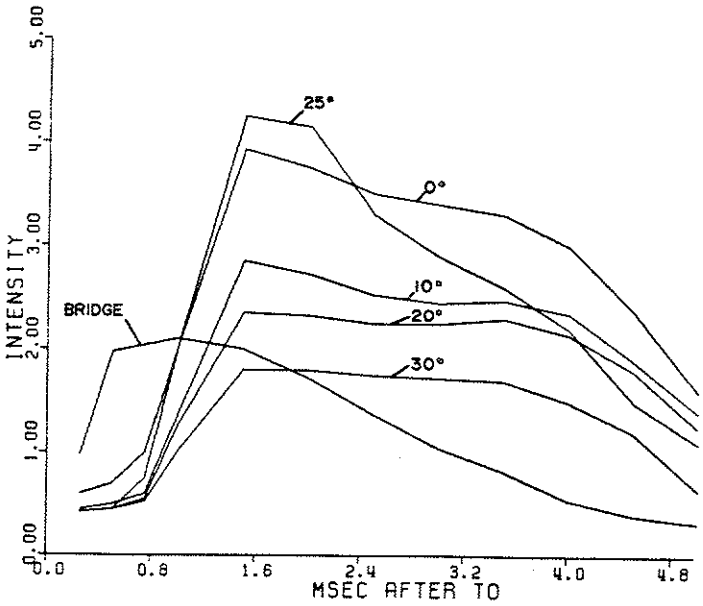

CHAPTER 7

CONCLUSIONS AND SUGGESTIONS FOR FUTURE WORK

The interpretation of experimental data with the aid of detailed global simulation codes yields a quantitative description of the processes affecting particle and energy confinement. Zero dimensional modeling with special treatment of severe inhomogeneities is adequate to reveal the basic mechanisms responsible for the plasma behavior. ICRF heating produces dramatic changes in the characteristics of the plasma. Analysis shows the puzzling behavior is due to an RF supported, anisotropic, hot ion edge plasma and its effect on the plasma-wall interaction.

Gun afterglow plasmas have straightforward behavior. The initially warm plasma briefly induces substantial reflux. The influx of neutral hydrogen and impurities rapidly cools the plasma. The behavior of the measured neutral densities determines the energy threshold for desorption as 50 eV. The plasma then very slowly continues cooling. The neutral atomic hydrogen density rises late in time. This is due to the increasing particle reflection probability and field line movement.

As RF power is added reflux fuels the plasma. Very stable equilibria are found due to the strong feedback the neutral influx has on the ion temperature and desorption yields. The RF drives a hot edge plasma tremendously enhancing reflux. At 100 kilowatts the huge fueling actually increases the density for part of the shot. Analysis of the

energy balance required of such fueling using the best available atomic rate coefficients leads one to conclude RF reduces the anomaly factor for the classical component of particle transport and that vibrational excitation of molecular species enhances fueling efficiency.

At higher RF powers the hot edge ions become gyroradius limited. The likely candidate for the limiter of these hot ions is the antenna limiter. This dramatically reduces the gas influx as the limiter area available for desorption is reduced by a factor of 5. The desorption of several monolayers of gas is sufficient to deplete the limiter gas load.

A prerequisite for determining such subtle plasma-wall interactions is a thorough understanding of a large number of processes affecting confinement. The recycling of hydrogen must be known to 10% accuracy to achieve factor of 2 accuracy in the basic plasma parameters. The evolution of impurity charge states is determined by the electron temperature history. The success ZD has in matching experimental data across a wide range of plasma parameters is strong evidence for the accuracy of the modeling of individual processes.

Such global modeling gives one powerful new diagnostics. A case in point is the use of the impurity charge state distribution as a measure of the reflux to particle transport rate ratio. Another use is to identify the characteristics affecting the interpretation of a diagnostic. Molecular hydrogen line radiation is seen to be a reasonable measure of the reflux rate.

A fringe benefit the use of modeling has is the ability to quickly test a proposed mechanism for reasonableness. The experience gained in extensive use of ZD has led to a detailed grasp of the subtle interactions between the plasma and surfaces. The author found the educational experience of using the code invaluable.

A substantial body of results has been left unmentioned to avoid obscuring complex discussions. The successful treatment of impurity-electron interactions indicates that the most complex sections of the code perform flawlessly. The assumption that gettered walls do not desorb particles is implicit in the treatment of desorption. Even slight errors here would have enormous impact on the plasma. The various coulomb collision processes as well as the ion-neutral scattering are also seen to work well. The Marshall gun does not contribute significantly to either the impurity or neutral content of the plasma. Finally, the various strategies for minimizing the computing time required reduced the calculation required by three orders of magnitude. A full one-dimensional simulation is computationally feasible.

One of the primary motivations of this study was to learn how to improve the plasma parameters. This study confirms the long recognized necessity for clean wall surfaces. A factor of two reduction in desorbed impurities permits the plasma to burn through the impurity barrier. This can be accomplished in the octupole by gettering the heavily bombarded walls in the bridge region. The limiters should be

totally gettered, perpendicular to field lines, and located in the center of the machine. This will reduce the ion induced desorption gas load and keep the neutrals away from the bridge region. Neutrals in the bridge are appallingly efficient in recycling due to the huge loosely bound gas reservoirs on the wall.

Several simple tests of the multiple limiter mechanism could be performed. The antenna limiters are thin stainless steel. Thermocouples near the upper edge would allow measurement of the heat deposited on the limiter. Since a fraction of a kilojoule is deposited on this limiter, the temperature rise would be substantial. (Perhaps this heating adds thermally induced desorbed neutrals as well.)

Simple spatial scans of Lyman α (H^0 line radiation) in the vicinity of the antenna would be very informative as well. Limiters (even gas depleted limiters) will be a large source of neutrals. It should be easy to verify the location of limiters with line integrated spectral intensities. In a similar vein, a relative measure of neutral density in the bridge compared to the central region is possible.

Several spectroscopic studies are clearly called for. First, some indication of titanium line radiation is clearly necessary. This requires extreme VUV instrumentation unavailable at the time of this study. The hot edge ions may be causing sputtering. Another essential study would be to get an indication of the H_2 vibrational spectra. This can be done by measuring the first electronic state band structure.

Comparison of the band structure from the plasma with that of a discharge tube would indicate any major shifts in vibrational level populations. A thorough study of vibrational state effects on H_2^+ rates is also needed.

Finally, it is observed that the hot edge plasma and severe velocity anisotropy are a major problem in terms of inducing reflux. The gyrolimited particles are probably a large energy loss as well. The ideal solution is to move the resonance to a more collisional location. One cannot, however, blindly reduce the oscillator frequency to place the resonance deeper in the plasma. The attenuation of the RF electric field and density profile must be considered to establish the optimum resonance location.